IMPLICATIONS OF THE ELECTRICAL RESISTIVITY STRUCTURE OF THE OLYMPIC MOUNTAINS AND PUGET LOWLAND

by

Claudia Maria Aprea

A dissertation submitted in partial fulfillment
of the requirements for the degree of

Doctor of Philosophy

University of Washington

1996

Approved by _____
(Chairperson of Supervisory Committee)

Program Authorized
to offer Degree_____

Date_____

Doctoral Dissertation

In presenting this dissertation in partial fulfillment of the requirements for the Doctoral degree at the University of Washington, I agree that the Library shall make its copies freely available for inspection. I further agree that extensive copying of this dissertation is allowable only for schorlarly purposes, consistent with "fair use" as prescribed in the U.S. Copyright Law. Requests for copying or reproduction of this dissertation may be referred to University Microfilms, 1490 Eisenhower Place P.O. Box 975, Ann Arbor, MI 48106, to whom the author has granted "the right to reproduce and sell (a) copies of the manuscript in microform and/or (b) printed copies of the manuscript made from microform.

Signature _____

Date _____

University of Washington

Abstract

Implications of the electrical resistivity structure

of the Olympic Mountains and

Puget lowland

by Claudia Maria Aprea

Graduate Program in Geophysics

The electrical structure of the Olympic Mountains and Puget lowland was surveyed by the use of an electromagnetic remote sensing technique known as Magneto-tellurics (MT). The goal was to retrieve a conductivity image of the area, and thus learn from it. For that purpose twenty MT stations were deployed in the surveyed area between 1992 and 1994.

The most important results from this study include the important role of fluid in the sedimentary Core rocks of the Olympic Peninsula; evidence that the sedimentary core is buttressed to the east and bellow the approximated position of the Peripheral rocks of the Olympic Peninsula; evidence of deep fault cutting close to the boundaries between the Peripheral rocks and the Seattle basin, and the Seattle basin and the pre-Tertiary basement; the strong correlation of both the crustal and Bennioff seismicity zone with contours of electrical structures suggesting for example, that the onset of deep earthquakes at the thrust zone depend on the material above the subducted slab in a way that the electrical condutivity of the rocks is affected.

Table of Contents

LIST OF FIGURES

ACKNOWLEDGMENTS

CHAPTER I

INTRODUCTION

Project POM (Puget lowland Olympic Mountains) is a study of the electrical structure of the area using the magnetotelluric (MT) method. Between the Fall of 1992 and the Summer of 1994 twenty MT stations were surveyed along a west-east line (see Figure I.1) $(47.62°, 47.82°)$ from approximately the Pacific coast at $124.377°$ to $121.7194°$.

The tectonic history of the Pacific Northwest margin has been shaped since the early Tertiary by plate convergence *(e.g: Riddihough, 1984; DeMets, et al., 1987)*. The Cascadia convergent margin flanks the west side of Oregon, Washington and Vancouver Island, and marks the boundary between the North America and Juan de Fuca plate (see Figure I.2). This is a zone of oblique convergence at a rate of about 4.2 cm/y in the direction N50°E *(Riddihough, 1976, 1984)*. Along much of this margin a forearc region has been subsequently has accumulated over a gently east-dipping sheet of lower Eocene basalt (see Figure I.3). These basalts erupted onto an oceanic crust close to the North American continent, and accreted during the late Eocene. These basalts are known as the Crescent formation in Washington, the Siletz River volcanics and Roseburg Basalt in Oregon, and the Metchosin volcanics in Vancouver Island. The forearc basin rocks and these Eocene basalts form the Coast Range and bedrock below the basins of the Puget lowland-Willamette trough. Further to the east, the western Cordillera is a collage of pre-Tertiary tectono-stratigraphic terranes.

The Olympic Peninsula represents an anomalous segment of the Cascadia margin: the subducting Juan de Fuca slab departs from its normally planar geometry forming an arch beneath the Olympic Peninsula, subducting at a dip of 10–12° at the top of the arch *(Crosson & Owens, 1987)* (see Figure I.4). As a result, the Tertiary accretionary prism accumulated onto the Crescent basalts, that underlies the continental slope and coastal areas of Vancouver Island and Oregon has been uplifted and exposed in Washington to form much of the Olympic Peninsula itself *(Brandon & Calderwood, 1990)*. The Olympic Peninsula is composed of two major terranes. The "Peripheral" and "Core" rocks *(Tabor, Snavely and Muller, 1983)*. I capitalize these names to avoid confusion in the text.

The "Core" rocks of the Olympic Peninsula (see Figure I.5) consist of the uplifted and eroded accretionary prism and form much of the Olympic Mountains. Basalts from the Crescent formation in Washington form the "Peripheral" rocks of the Olympic Peninsula, as they crop out in a crescent-shaped or horse-shoe shaped form. They dip down towards the east beneath the Puget lowland and towards the north beneath part of Vancouver Island. Core rocks are in fault contact, with the Peripheral rocks. Lying structurally beneath the major thrust fault in the zone, the Peripheral fault, the Core rocks dip beneath the Peripheral rocks.

The Puget lowland presumably lies over the contact between the Coast Range terrane and the older North America continental margin (pre-Tertiary). This area is characterized by the presence of several faults marking a complex tectonic history. The Seattle basin (see Figure I.6), lies within a large negative gravity anomaly *(Danes, et al., 1965; Finn et al., 1991)*, and is crossed by the north-south trending, apparently inactive Puget fault. East of the Puget fault a not yet fully understood fault zone

reflects the complexity of a region characterized by the assemblage, thrust imbrication and arrangement of different tectono-stratigraphic terranes; events that go from late Cretaceous to early Tertiary in time *(Johnson & Potter, 1994)*. The Seattle fault is a zone that consists of four east-west striking south dipping faults. This fault zone appears to be truncated by the Hood Canal fault to the west and not to continue through the Olympics.

Although there is a basic knowledge of the tectonic history of this area, a lot of things remain unknown or not fully understood. For example (see Figure I.7), the contact between the Coast Range terrane and the older crust to the east has been partially covered by mid-Tertiary and Quaternary volcanism in the Cascades along much of Oregon and Washington. Important features in the Puget lowland are covered by a thick mantle of Quaternary deposits and further obscured by Puget Sound. The deeper structure in the Peripheral rocks is obscure.

Geophysical remote sensing methods are thus crucial. Methods that remotely sense the electrical conductivity of the earth can be of use in answering some of the questions, because high contrasts in the electrical conductivity can be expected between the most important features in this area due to differences in lithology. For instance, contrasts of at least two orders of magnitude are expected between sediments (from both the forearc region and subduction complex) and basalts (from the Crescent Formation and subducting Juan de Fuca oceanic crust).

Extracting an electrical conductivity image of the area may illuminate some of the obscured features. For example, the mapping of abrupt changes in conductivity expected between the Core and Peripheral rocks may give information about the lower boundaries of the Peripheral rocks and about the deeper structure of the subduction

complex itself. Do the Core rocks continue beneath the Peripheral rocks, and if so, to what extent?.

The Magnetotelluric Method (MT) and the Magneto Variational Method (MV) consist of the measurement of naturally occurring electromagnetic fields at the earth's surface. Information about the sub-surface electrical structures can be inverted from the data (defined as certain functions of the electromagnetic fields in the frequency spectrum). The data cover a frequency range from $(9.09 \times 10^{-5} \; 5.00 \times 10^{-2})$ s^{-1} (i.e period: from 20 to 11000 s) and sample the crust and upper mantle.

This dissertation presents a detailed study of the POM MT data. A two-dimensional resistivity model with respect to an experimentally determined electric strike is presented and interpreted in the context of the regional geology.
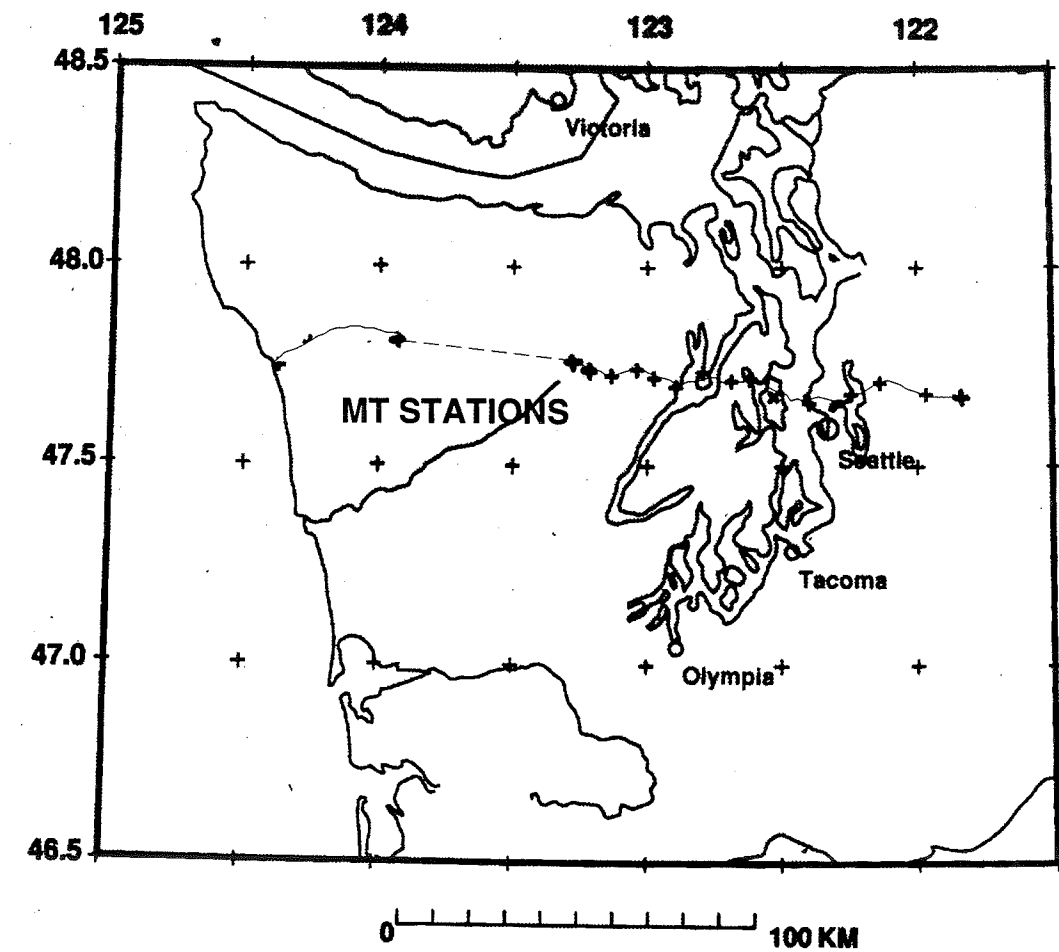
FIGURE I.1
Map of the Pacific Northwest showing the location of the twenty Magnetotelluric stations deployed between 1992 and 1994 for POM project (Puget lowland Olympic Peninsula).
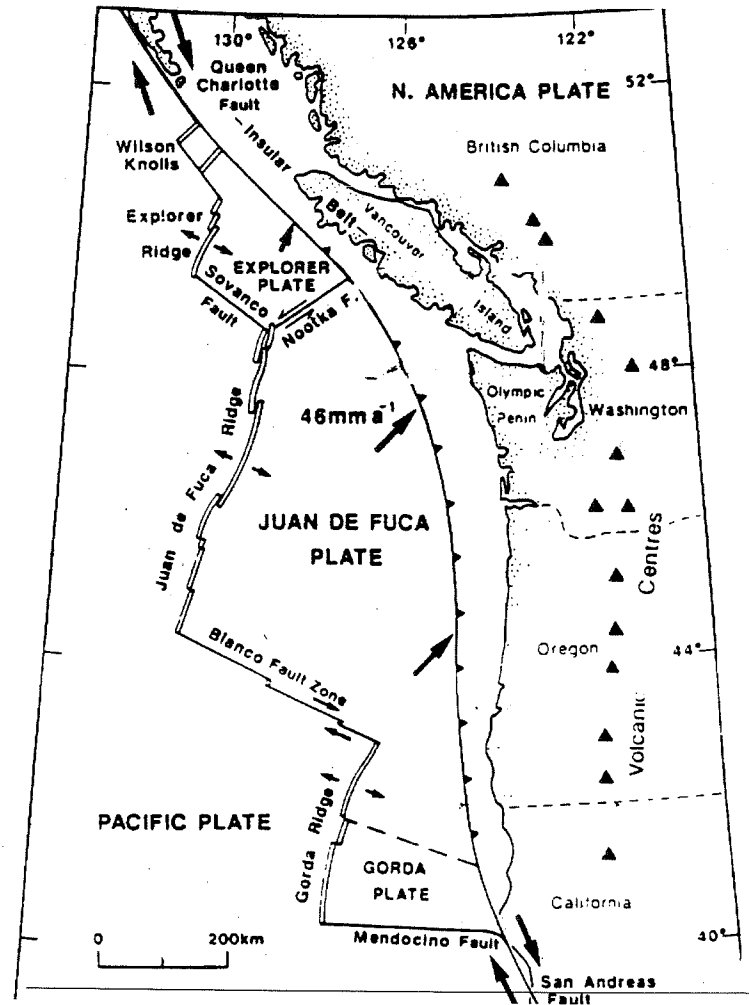
FIGURE I.2

The Cascadia convergent margin marks flanks the coast of
Vancouver Island, Washington and Oregon. Since the Tertiary
the Juan de Fuca Plate is being subducted beneath the North
American plate (from Wannamaker, et al. 1989).
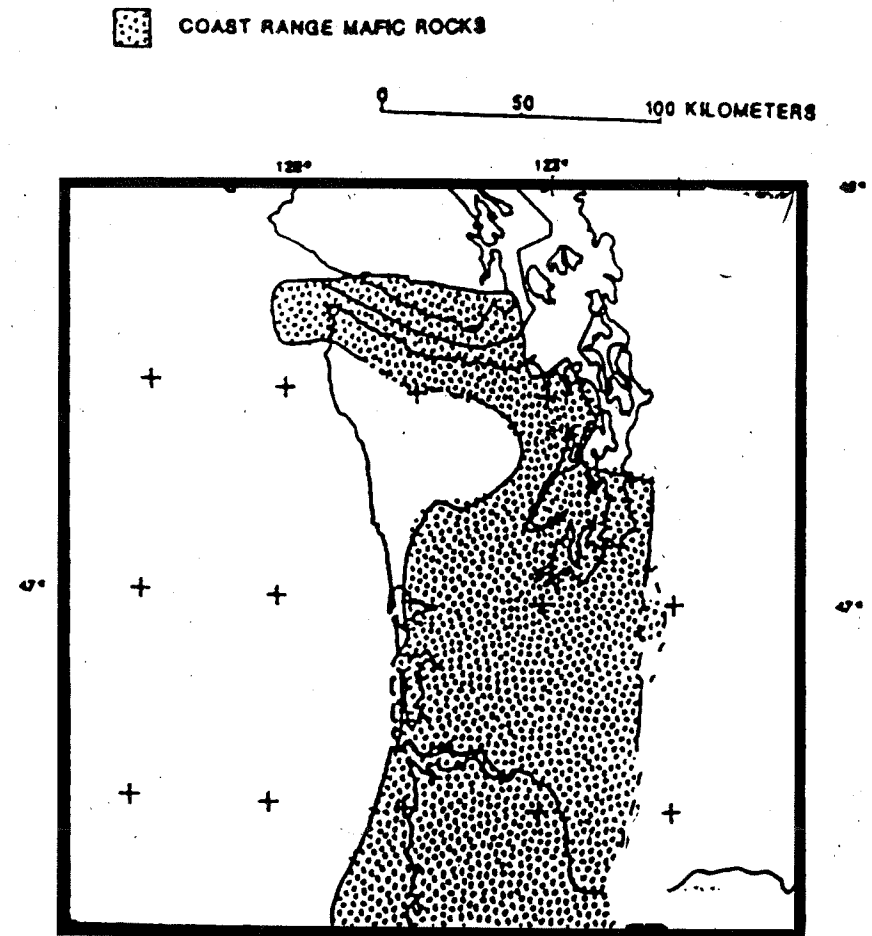
FIGURE I.3

Map showing the minimum extent of the Coast Range mafic rocks
as interpreted from gravity and magnetic data (Finn,1990).
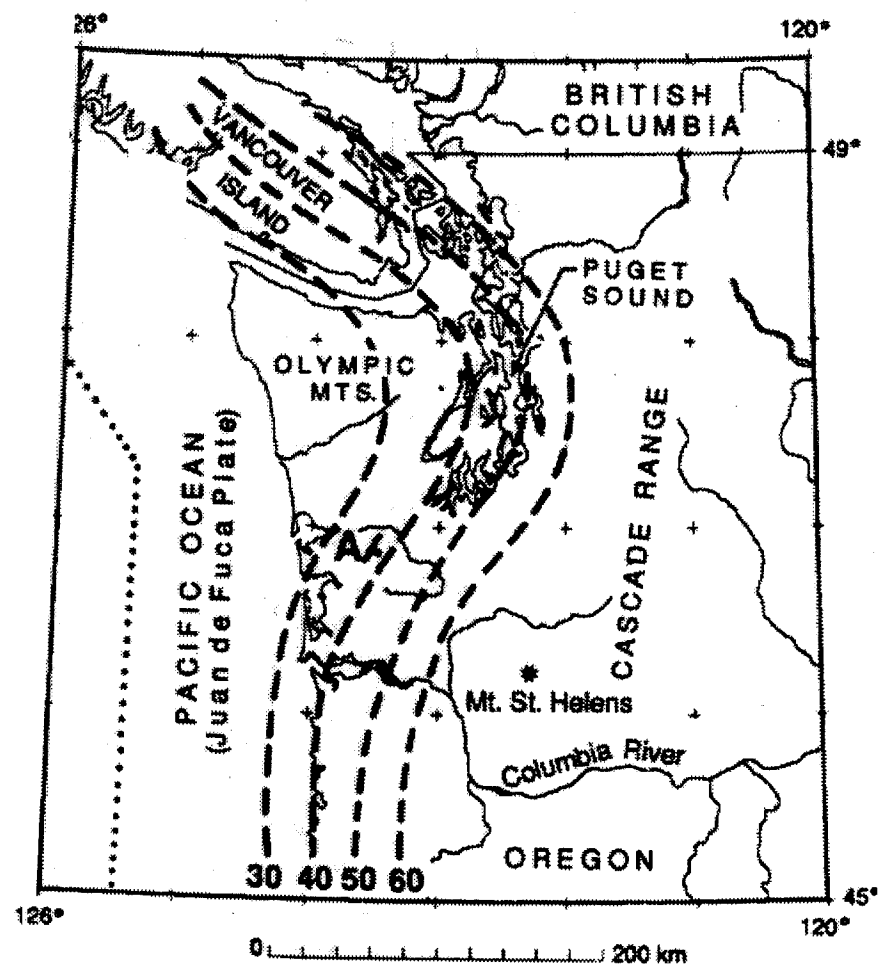
FIGURE I.4

Contour map of the subductied oceanic Moho, from sesmicity and teleseismic waveform analysis (contours in km) (from Crosson and Owens, 1987)
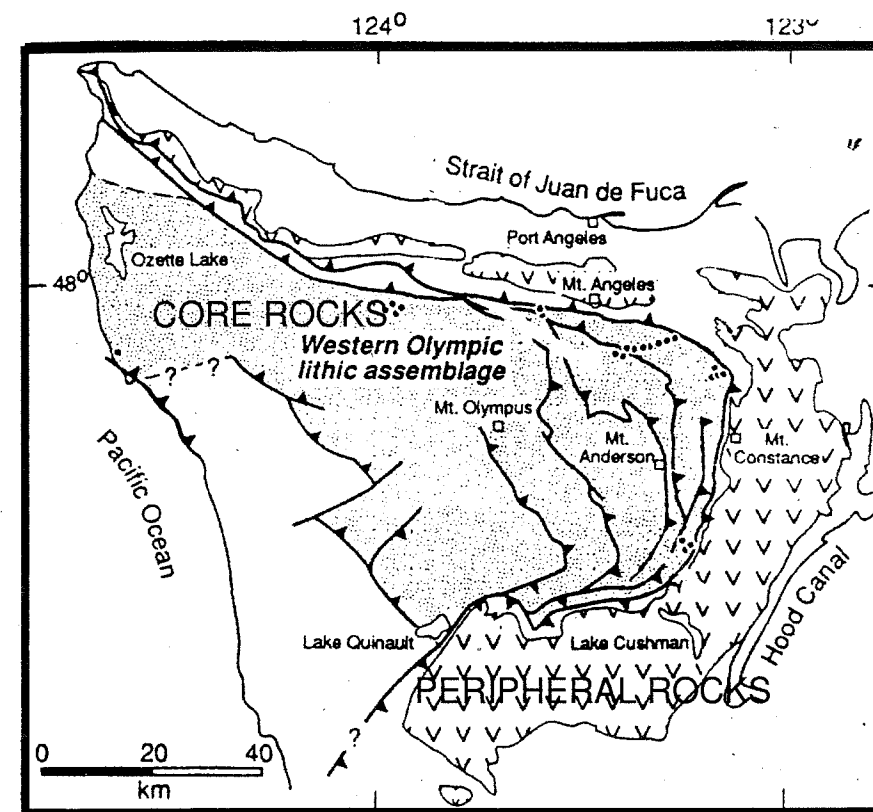
FIGURE I.5

Geological map of the Olympic Peninsula showing the Olympic "Core" rocks (marine sedimentary) and basalts of the Olympic "Peripheral " rocks (from Heller, et al., 1992).
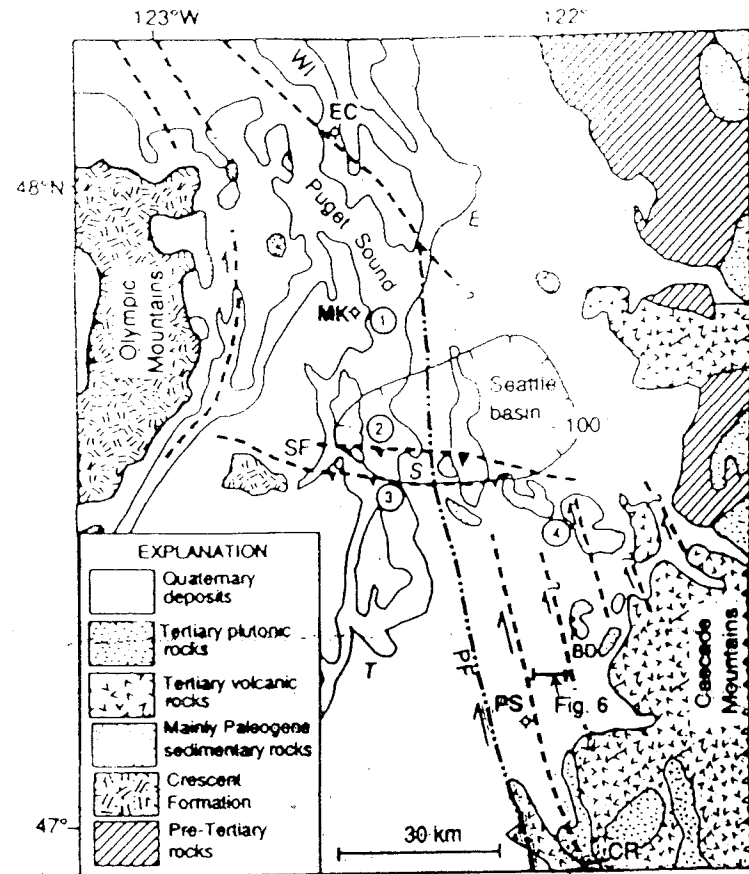
FIGURE I.6
Central Puget lowland and Puget Sound, deepest part of Seattle basin is area enclosed by −100 mgal Bouguer gravity contour. SF: Seattle fault zone, PF: Puget fault, S:Seattle, T: Tacoma, E: Everett (from Johnson & Potter, 1994).
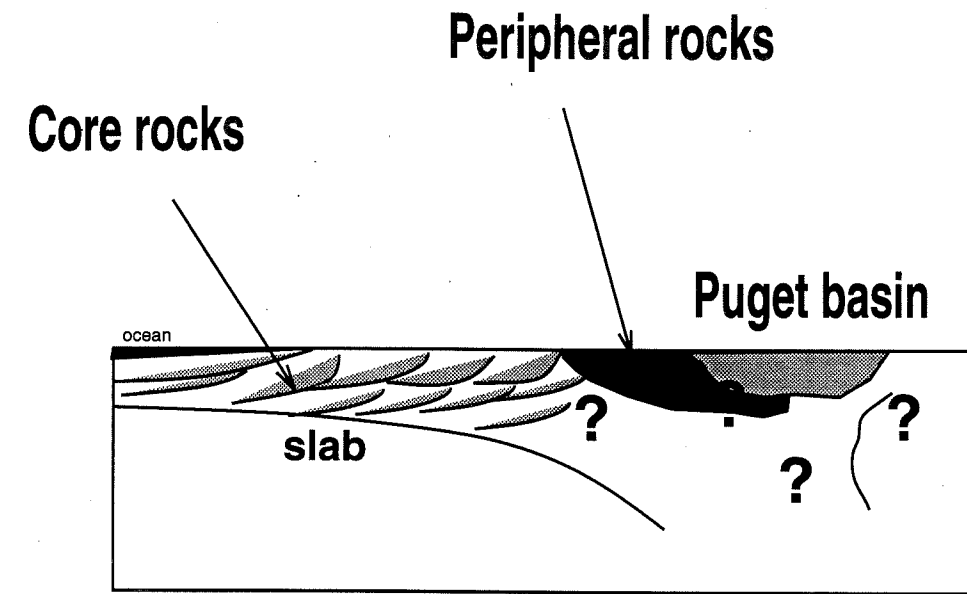
FIGURE I.7
Sketchy cross−section showing the major structures in the Olympic Mountains and Puget lowland marking questionss addressed in POM project, see text.

1. INTRODUCTION

There have been several previous geophysical investigations in the western part of Washington State, and some of them include regions that overlap our profile. These studies have provided considerable detail about the geology, structure and tectonics of the study area. I will present some of these studies, classified by the type of study.

2. PALEOMAGNETIC, PALEOSEISMIC, GEODETIC, SEISMIC AND THERMAL STUDIES AND MODELS OF THE CASCADIA CONVERGENT MARGIN

Most convergent margins have experienced megathrust earthquakes in historical times. These earthquakes occur in the primary thrust or detachment surface of the subduction zone and produce the largest earthquakes in the world. The Cascadia margin is unusual in that it has not experienced a large earthquake in historical times *(Rogers, 1988; Heaton, 1990)*. The reasons for this situation may be:

(a) there is no present convergence

(b) there is convergence, but it is being taking up by aseismic slip

(c) large earthquakes occur infrequently, with the most recent having occurred before historical records began

Plate tectonic analysis of magnetic anomalies and transform fault orientation offshore Cascadia indicate convergence for the past few million of years *(e.g.*

Riddihough, 1984; DeMets, et al., 1987). Ongoing convergence is also supported by a wide variety of data along the deformation front *(e.g. Riddihough & Hyndman, 1976; Carson, 1977; Cochrane, at al., 1988; Davis & Hyndman, 1989; Hyndman, 1990)*.

On the basis of the above evidence, convergence is occurring. Is it accommodated by aseismic slip or great earthquakes?

Geodetic studies show that the strain accumulated in the Northwestern Washington is close to that which would correspond to a model of the Cascadia subduction zone with a plate interface partially locked. Measurements of horizontal deformation in western Washington and Vancouver Island indicate an east-north-westward contraction *(Savage, et al., 1981; Dragert, 1989; Lisowski, et al., 1989)* and inferred coastal uplift and subsidence farther inland *(Darienzo, et al., 1965; Holdahl, et al., 1989*; are consistent with a locked plate offshore. The rupture of the locked segment would produce the coseismic coastal subsidence observed by *Atwater (1987)*. Strain rates in the Olympic Mountains and in the Seattle area are uniaxial east-northeast contractions. The maximum uplift in any east-west line occurs near the Pacific Coast, while uplift rates observed in the Puget Sound region are negligible *(Savage & Lisowski, 1991)*. The authors point out that geodetic data alone cannot be used to discount aseismic subduction; inelastic deformation of the Olympic Peninsula could probably account for the currently observed deformation.

Nevertheless, there is ample evidence of major earthquakes on the Cascadia margin at approximately every 300 to 600 years, including shaking and abrupt vertical motion in coastal regions, periodic turbidites flows in several deep channels, and evidence of tsunamis *(i.e., Adams, 1990; Atwater, et al., 1991)* so, overall evidence supports the idea that large earthquakes probably occur.

In cross-section, the subducted zone thrust can be divided into four subzones based on material properties and thermal regime,

(1) zone of stable sliding at the seaward end of the thrust detachment.

(2) locked zone with stick-slip or unstable sliding behavior (elastic strain may be stored between abrupt motion events, earthquakes may nucleated).

(3) transition zone, either stable sliding behavior or brittle behavior may occur (earthquakes may rupture into this zone after nucleating in the locked zone).

(4) zone of plastic behavior associated with high temperature extending to great depth.

Thermal constraints limit the width of the locked zone. *Hyndman & Wang (1993)* worked on the thermal constraints on the zone of possible megathrust earthquakes failure in the Cascadia subduction zone. They presented a model for the "locked" aseismic zone in the Cascadia margin. The term "locked" describes a zone capable of generating thrust earthquakes, but which is currently aseismic. Fault motion within the brittle or semi-brittle region may be stable sliding or stick-slip, and because faults earthquakes are manifestation of frictional instability they may initiate only in the latter case.

There is a critical temperature for the transition between unstable and stable sliding behavior, most laboratory data estimates give temperatures of 300 C° to 350 C° *(i.e.: Chen & Molnar, 1983; Tse & Rice, 1986; Wong & Chapman, 1990; Scholtz, 1990; Blanpied, et al., 1991)*. In Vancouver Island it has been shown that earthquakes nucleate above depths approximately corresponding to this range *(Tichelaar & Ruff, 1992)*.

Figure II.1 shows the resulting thrust-fault model of *Hyndman, et al. (1993)* based on three profiles (Vancouver Island, Olympic Peninsula and Oregon). In this model the

authors took the principal detachment zone as the top of the down going slab. The thermal regime in the Olympic profile was calculated using similar thermal parameters determined for Vancouver Island, and information on the thermal conductivity in the Olympic Peninsula. Using the temperatures limits of 350–450C° and the seaward limit defined by the frontal thrust, the stick-slip zone was proposed to have a width of approximately 100 kilometers, with the transition zone extending another 80 kilometers landward to just inland of the coast, with an estimated 30 kilometers error for the inland boundary.

Earthquakes and seismic data provide information about the position of the slab at depth. Using earthquake hypocenters and analysis of P to S converted phases from teleseisms, *Crosson & Owens (1987)* show a preliminary model for the subducted slab. The slab is forced upward as it is subducted, due to the concave seaward curvature along the subduction zone. A concentration of crustal and plate seismicity beneath the eastern Olympic Mountains and Puget lowland may be in indirectly related to the presence of this arch *(Chiao & Creager, 1989)*. The arch in the Juan de Fuca slab is believed to be a consequence of the curvature of the Cascadia margin, from almost NS south of 47° north latitude to approximately N30°W north of 48° north. The slab appears to be easily flexed, it dips 10–12° beneath the Puget Sound (the top of the arch), while north and south of the arch the bend is about 15–20°. Figure II.2 an schematic illustration of the development of the slab arch. *Brandon & Calderwood (1990)* postulate that this arch was formed when the Southern Cordilleran coastline swung westward.

In summary, the Cascadia convergent margin is active; although large thrust earthquakes typical of convergent margins are absent in the historical record of this

region, nevertheless there is evidence of prior-to-historical-time earthquakes; geodetic data support a model with an offshore locked thrust zone (where earthquakes may nucleate when unlocked), followed by a transition zone (partly offshore-inland); the Juan de Fuca slab is characterized by a departure from planar geometry beneath the Olympic Mountains probably caused by the change in the azimuth of the Cascadia margin; and, finally, crustal and subcrustal nucleation of earthquakes beneath the eastern Olympic Peninsula and Puget lowlands may be related to the arch in the slab.

3. ELECTRICAL CONDUCTIVITY SURVEYS

Several MT profiles have been completed across the Coast Range (see Figure II.3a). *Stanley, et al. (1990)* detected a conductivity anomaly (first discovered by *(Law, et al., 1980)* in the Washington Cascades. It is known as the Southern Washington Cascades Conductor (SWCC). Figure II.3b shows part of the MT resistivity model for the profile AA' of Figure II.3a. The SWCC has a typical resistivity of 2 ohm-m. It is interpreted by *Stanley, et al. (1990)* to be a possible fore-arc basin and accretionary prism from late Cretaceous early Eocene time which was accreted to the older continent. There is also another conductor resolved mainly by profile CC' (in Figure II.3b). *Stanley, et al. (1990)* interpreted this conductor as representing sediments from the Tertiary melange formations of the Olympic Peninsula.

In 1987 MT data were collected at the bottom of Lake Washington *(Schultz, Booker & Larsen, 1987)*. The SWCC was also detected in this study. The authors suggested the source of this anomaly is an electrical current induced in the north-east Pacific Ocean, then channeled through the Straight of Georgia and then down into the Puget Sound. The inferred north-northwest MT strike direction was 15° east of

geographic north.

In 1993, *Egbert & Booker (1993)* detected the SWCC again from a series of small overlapping magnetovariational (MV) arrays. From the resulting vertically integrated electrical conductivity they also mapped a weaker east-west trending anomaly south of Puget Sound. Data show also that the conductivity structure for the crust west of the Cascades is distinctively three dimensional. The authors suggested that rocks forming the SWCC are analogous to the present day Olympic Peninsula Core.

Two other MT studies, one in Oregon (the EMSLAB project, *Wannamaker, et al., 1989)*, the other one in southern British Columbia (Canada) *(Kurtz, DeLaurier & Gupta, 1986)* although not exactly in this study area, give relevant information to the Cascadia convergent margin. Basically both models (two-dimensional resistivity models, e.g. Figures II.4 and II.5) have some of the common features for this convergent margin with their local characteristics. Conductive material representing sediments from the Cascadia basin and subduction complex, and resistive material for the basalts of Coast Range and oceanic subducted crust.

In summary, these MT studies state that the features characterizing a convergent margin were successfully identified north and south of the study area; and give information about the presence of other further inland features.

4. GRAVITY AND MAGNETIC DATA

The magnetic and gravity maps of western Washington show large amplitude positive anomalies associated with the Coast Range mafic rocks, separated by negative anomalies over deep sedimentary basins. These large positive anomalies indicate that the Coast Range mafic basement extends at least as far east as the longitude of Seattle.

Also, many unmapped buried faults are inferred by steep gravity and magnetic gradients *(Finn, 1990)*.

Finn (1990) proposed a density model cross-section for the profile shown in Figure II.6a. Structures that produced observed gravity and magnetic anomalies were determined by Finn using 2 1/2-dimensional forward and inverse gravity and magnetic modeling program. Figure II.6b shows the part of the upper 50 kilometers of Finn's model that would overlap a 2-D model for the POM MT transect.

In Finn's study the data were not sensitive to the deeper part of the subducting plate, thus information about the deep part of downgoing slab and the asthenosphere was based on other sources. In Finn's model from gravity and magnetic data, the Coast Range basalts reach a depth of approximately 30 kilometers, the same depth for the modeled sediments associated with the subduction complex. A possible extension of the subduction complex to a depth of 40 kilometers is implied. This model also shows the presence of two blocks east of the Coast Range unit suggested to be old oceanic crust and part of an old accretionary prism; and a structure beneath the modeled Coast Range unit which is proposed by Finn to be either part of the subduction complex or mantle.

5. SEISMIC DATA

Refraction data collected onshore-offshore across a line passing through Centralia (in southwest Washington) were interpreted by *Taber & Lewis (1986)* using a velocity model which shows that the best constrained parts of the slab are the bend of the subducting slab and the clear indication of the continuity of the slab beneath Puget Sound.

Seismic experiments conducted in 1989, 1991 and 1993, by *Trehu, et al.* allowed construction of a crustal image beneath northwestern Oregon and southwestern Washington. The authors presented a velocity model *(Trehu, et al., 1994)* that shows considerable velocity variation within the crust of the studied area. Seismic data suggest that the thickness of the Coast Range basalts varies by approximately a factor of 4 along the strike of the Cascadia subduction zone. In Oregon the accreted terrane is 25 to 35 kilometers thick, meanwhile in Vancouver it is only 6 kilometers thick. *Trehu, et al. (1994)* suggest that the strength of the forearc crust increases as the thickness of the accreted terrane increases.

Analysis of seismic reflection data also revealed a Seattle basin, consisting of 9 to 10 kilometers of Eocene and younger deposits (Figure II.7), with the basalts from the Crescent Formation as the basement *(Johnson, Potter & Armentrout, 1994)*.

VanDecar & Crosson (1990), used high-quality data from teleseismic relative phase arrival times to image the deep structure of the Cascadia subduction zone, indicating that lateral heterogeneities extend to considerable depth.

Schultz & Crosson (1996), also provided a two-dimensional seismic P-wave velocity model, to a depth of about 50 kilometers for a 425 kilometers long profile extending from Hood Canal to Walla-Walla. Crustal thickening is observed reaching a maximum beneath the highest topography in the Cascade Range, this is explained as magmatic underplating driven by the dehydration of the Juan de Fuca plate.

A receiver-function array study in the Puget Sound region was carried out in 1994 *(Pullen, Creager & Malone, 1994)* across an east-west 100 kilometers line. They explain their data with a simple model of a deep, low-velocity sedimentary basin (5-10 kilometers depth) extending from approximately Toandos Peninsula to at least

Carnation Farm *(Pullen, personal com., 1996)* with a 15° dipping slab over a half space representing the subducting Juan de Fuca Plate.

6. GLOBAL SUMMARY

The position of the downgoing slab is fairly well constrained; including the position of the bend, and the variation of dip angles along the slab. The presence and position of the anomalous arch in the Juan de Fuca slab beneath the Olympic Mountains is also well constrained by data. A local spatial concentration of crustal and subcrustal earthquakes is located in the Puget lowlands and eastern Olympic Peninsula.

Several lines of evidence indicate that the current convergent regime corresponds to a model where there is a locked zone in the main detachment thrust interface, a source for a future large thrust earthquake (making up for the current absence of seismicity). This locked zone is offshore but the transition zone to stable sliding is partly inland beneath the Olympic Peninsula. These zones were modeled by temperature-dependent models and so a proposed thermal regime for the zone is available. The position of the continental Moho and the crustal velocity structure east of the Hood Canal was presented in a recent work; magma underplating was suggested as an explanation for the thickening of the crust where the highest topography exists in the Cascades.

From previous and on-going work, the extent of the Seattle basin is fairly well constrained. This deep basin apparently extends from Toandos Peninsula to some point east of Carnation Farm. Gravity and seismic data provide an estimate of the minimum extent of the Coast Range structure. In Puget lowland the results seem not to be conclusive as they differ.

MT lines north and south of our study provide useful constraints on out MT work.
Such as the conductivity range for sediments and basalts.
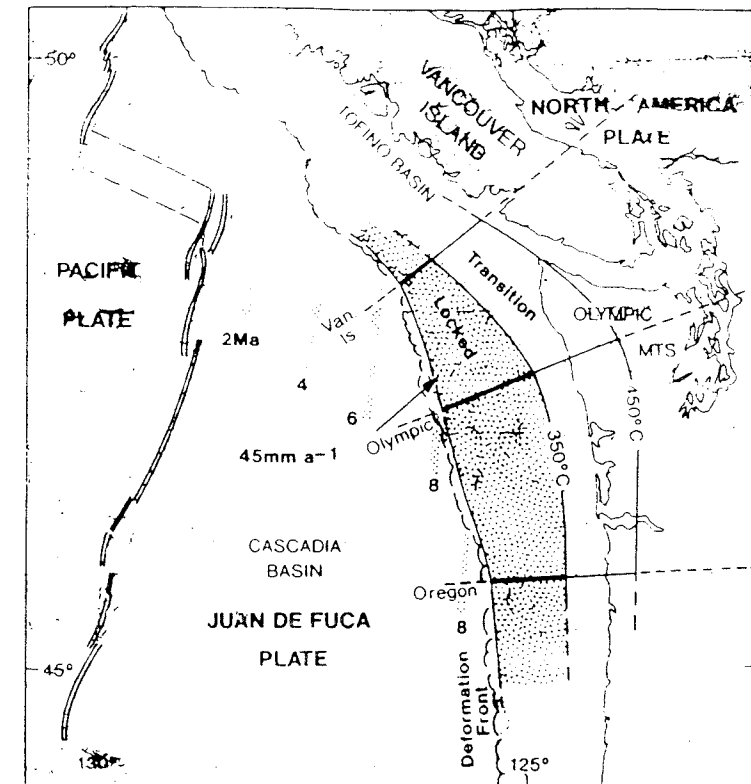
FIGURE II.1

Map showing the computed limits of the stick–slip locked stable
sliding transition zones for the subduction thrust plane (an error
of 30 km is permited in the ladward boundaries of the locked and
transition zones (from Hyndman & Wang, 1993).
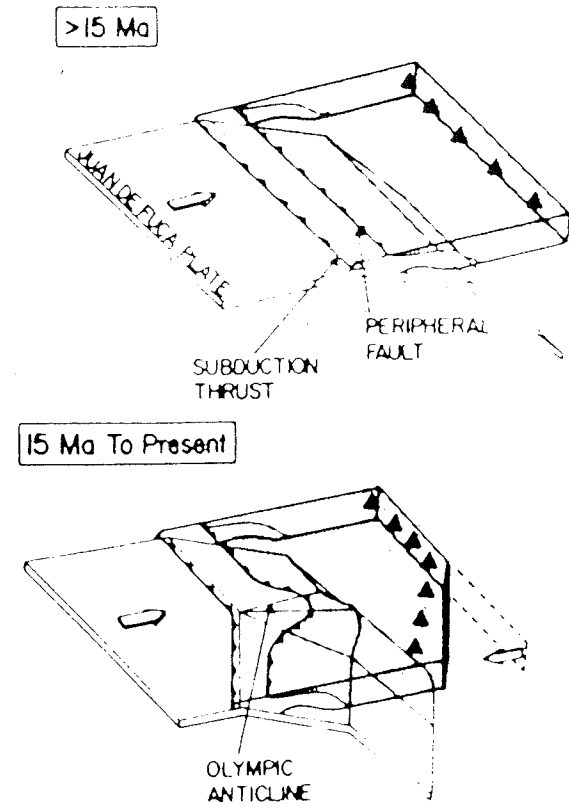
FIGURE II.2

Schematic illustration of development of slab arch beneath Olympic Mountains uplift (from Brandon, et al., 1990).
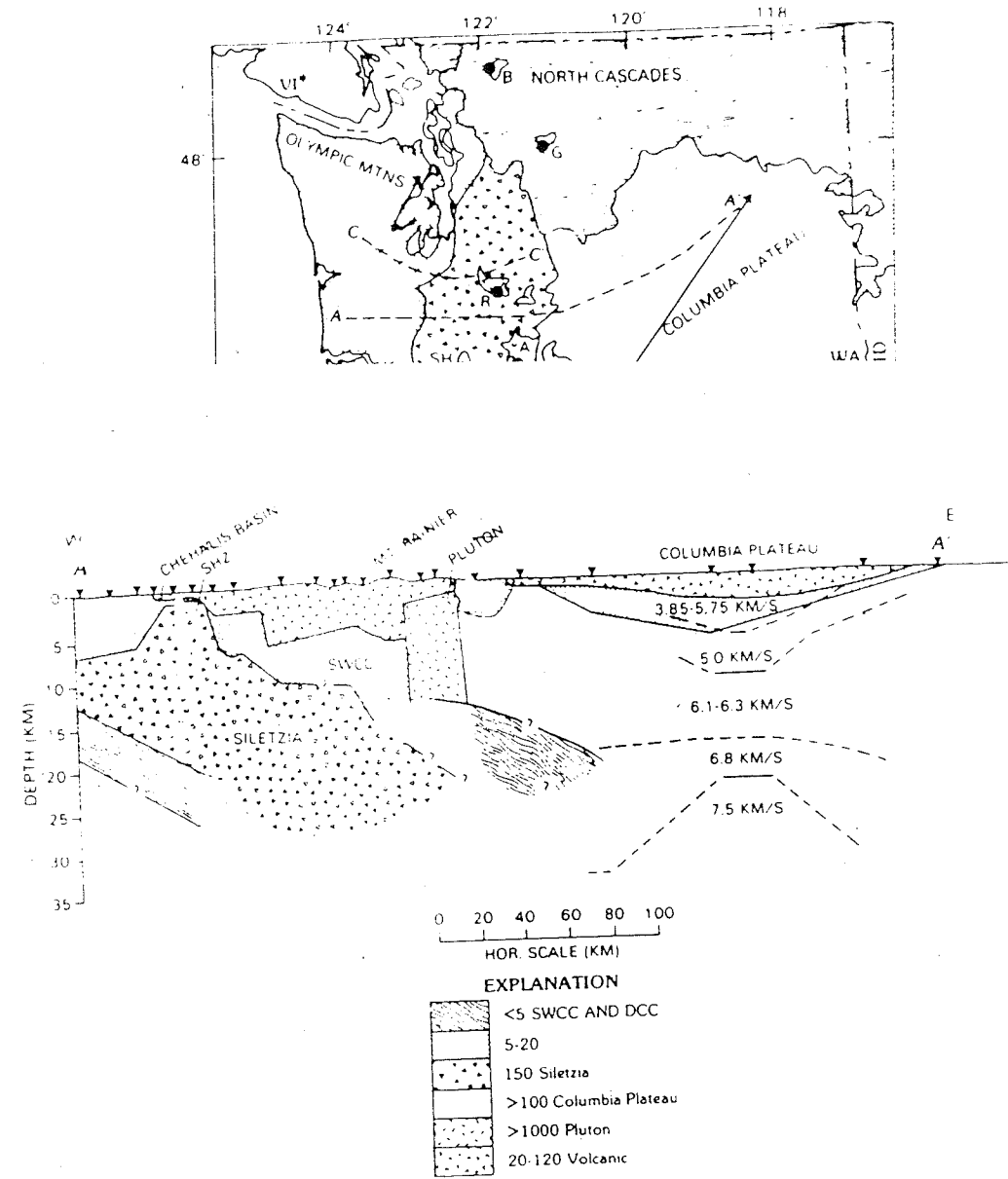
FIGURE II.3

(a)Location of some Magnetotelluric profiles in Washington State (R: rainier, SH: Saint–Helens)(from Stanley et al., 1990).
(b)MT model for profile AA' . SWCC:Southern Washington Cascade Conductor, DCC: Deep Crustal Conductor (from CC'). SHZ: saint Helens Zone, Siletzia: local name for Coast Range (from Stanley et al., 1990).
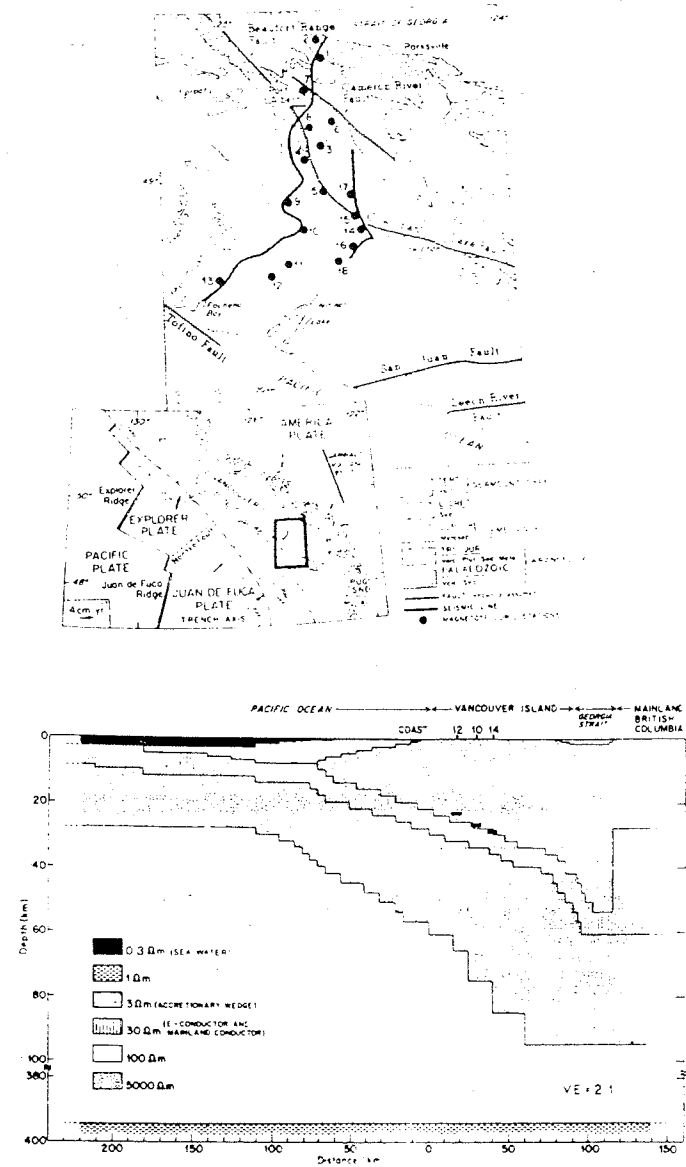
FIGURE II.4
Resistivity cross–section for transect across Vancouver Island
(from Kurtz. et al., 1986).
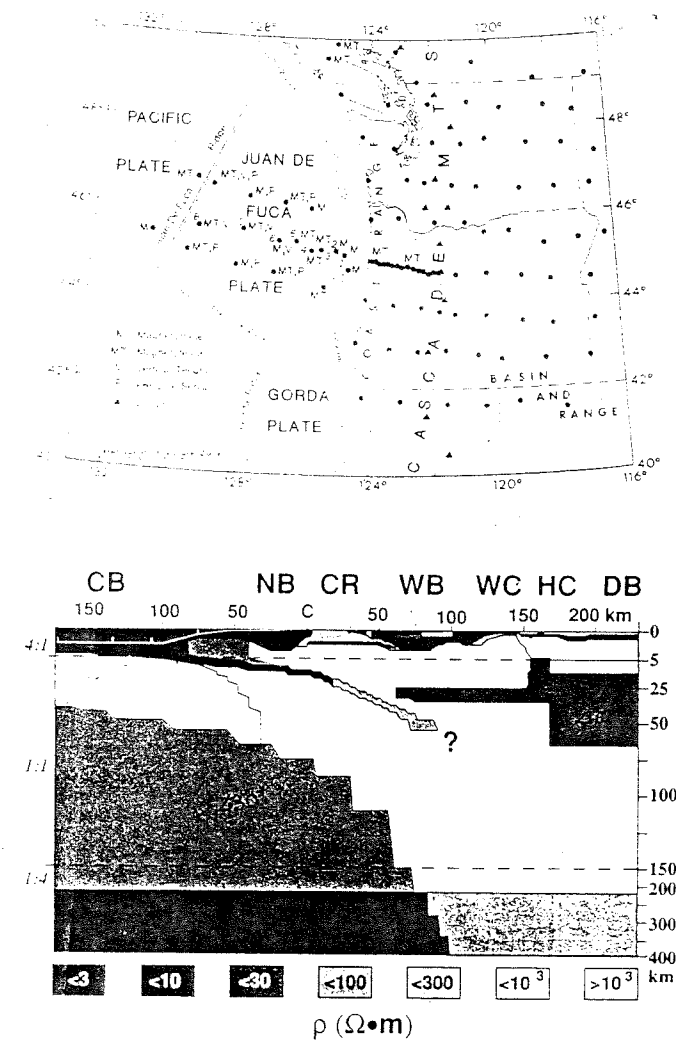
FIGURE II.5
East–West resistivity cross–section derived from EMSLAB MT data along the
Lincoln line (Wannamaker, et al., 1989).

(a)

(b)
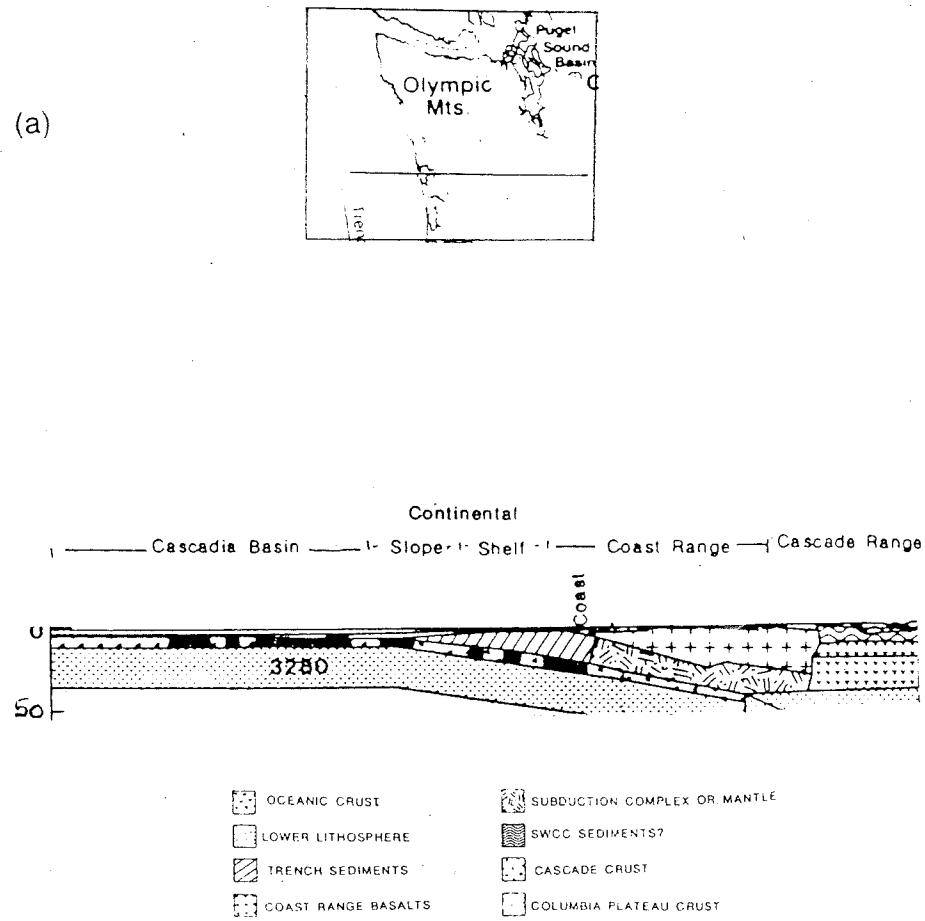
FIGURE II.6
(a) map showing location of the transect in a gravity–magnetic data study
(b) par of the resulting density cross–section for transect show in (a) (Finn, 1990)
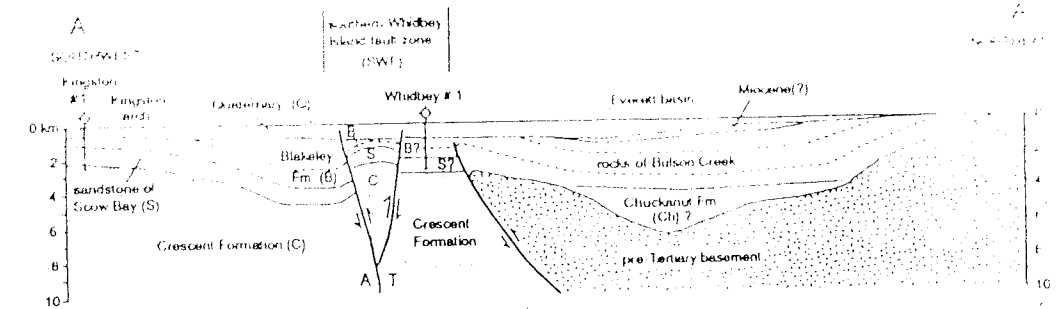
FIGURE II.7
Seattle basin as revealed from seismic reflection data (from Johnson, Potter & Armentrout, 1994).

CHAPTER III

THE MAGNETOTELLURIC AND MAGNETOVARIATIONAL METHODS

1. INTRODUCTION

The electrical conductivity of a medium measures its ability to allow the flow of electrical currents. Some materials do better than others and are called conductors (versus resistors). The S.I. unit for conductivity σ is Siemens/m, and for resistivity (ρ, defined as the reciprocal of the conductivity) is ohm-m . The conductivity of materials can be explained by different mechanisms, metallic conduction: electronic semi-conduction; and solid and aqueous electrolytic conduction (see Appendix B).

Within the earth, the range of resistivity values is very wide, ranging from less 0.3 ohm-m to greater than 10,000 ohm-m (see Figure III.1). Most materials encountered in the subsurface are poor conductors (in their solid state), nevertheless the resistivity can become very low, due to the intrusion of some conductive material (such as natural occurring metals, graphite, water, etc.).

2. THE MAGNETOTELLURIC AND MAGNETOVARIATIONAL METHODS

The use of naturally occurring electromagnetic fields for determining the electrical structure of the earth came into use about 1960. Two principal forms are the Magneto-telluric (MT) method and the Magnetovariational (MV) method.

The most important form of excitation from external fields sources, is the indirect induction of current from the ionosphere and magnetosphere into the earth (*Vanyan*

and Butkovskaya, 1980). It can be shown that the magnetotelluric field induced by large-scale magnetospheric or ionospheric currents will behave as a plane wave in a uniform or horizontally stratified earth *(Zhdanov and Keller, 1991).*

The standardized magnetotelluric sounding method consists of simultaneously recording time series of four components of the horizontal electromagnetic field, {E_x, E_y, H_x, and H_y}. The magnitudes for the electric and magnetic fields are of the order of millivolts per kilometer and nanoteslas respectively. Induction coils and flux gates are used to measure the magnetic field (**B**). Horizontal components of the electric field are measured as voltage differences over orthogonal grounded dipoles with chemically stable electrodes (a metal and its base) at its extremes (see Figure III.2). The fields are measured as time-series. Figure III.3 shows typical time series for a sample interval of 5 seconds. Voltage difference instead of the electric field is shown as this is what is actually measured. Division by the dipole lengths is needed to convert these voltages into spatially averaged electric fields.

3. THEORY

3.1. Early work

Tikhanov (1950) in the Soviet Union and *Cagniard (1953)* in France, independently discovered the important consequences of the solution to Maxwell equations for a monochromatic quasi-stationary electromagnetic field incident on a one-dimensional (1D) earth.

Maxwell equations plus Ohms Law, can be reduced to diffusive equations for either the electric (**E**) or magnetic fields (**H**) which are mutually orthogonal. When the

frequency is sufficiently low

$$\nabla \times \mathbf{E} = i\,\omega\,\mu_0\,\mathbf{H}$$

$$\nabla \times \mathbf{H} = \sigma\,\mathbf{E}$$

In the 1D case with mutually orthogonal magnetic and electric fields

$$\mathbf{H} = (\,0\,,\,H_y\,,\,0\,) \qquad (III.1)$$

$$\mathbf{E} = (\,E_x\,,\,0\,,\,0\,)$$

this coupled partial differential system reduces to

$$\frac{d^2 E_x}{dz^2} + \sigma(z)i\omega\mu_0 E_x = 0 \qquad (III.2)$$

with solution :

$$E_x = E_x(0)\,e^{kz}$$

where

$$k^2 = i\omega\mu_0\sigma$$

from which it is easy to show that

$$Z \equiv \frac{E_x}{H_y} = (\omega\mu_0\sigma)^{\frac{1}{2}} e^{-i\frac{\pi}{4}}$$

The main point here is that this relationship between the horizontal components

depends solely on the frequency and on the conductivity. Z is called the *MT impedance* and can be evaluated at the surface from the magnitude and phase of the horizontal electrical and magnetic field vectors in orthogonal directions. Once Z has been measured, one can invert the above result for the conductivity of the halfspace. *Tikhanov (1949)* was the first to apply this result to real data. In the more complicated situation, where σ depends on depth, Z will depend on ω and measuring Z(ω) permits one to determine σ(z). Since Z is complex, is has become traditional to work with its phase and a quantity determined from its modulus called the apparent resistivity, which is defined by

$$\rho_{app} \equiv \frac{1}{\omega\mu_0}|Z|^2$$

Obviously ρ_{app} is the true resistivity in the special case of a halfspace.

3.2. Extension to 2d and 3d cases

The definition of impedance involves a relationship between mutually orthogonal components of the electric and magnetic fields. The extension of the one dimensional case to a two-dimensional (2D) or three-dimensional(3D) case results in the following relations between the horizontal field components.

$$E_x = Z_{xx} H_x + Z_{xy} H_y \qquad (III.3a)$$

$$E_y = Z_{yx} H_x + Z_{yy} H_y \qquad (III.3b)$$

which can be written

$$\mathbf{E = Z \ H}$$

where

$$\mathbf{Z} = \begin{bmatrix} Z_{xx} & Z_{xy} \\ Z_{yx} & Z_{yy} \end{bmatrix} \qquad (III.4)$$

is the "impedance tensor".

In the 1D case the impedance tensor reduces to:

$$\mathbf{Z} = \begin{bmatrix} 0 & Z \\ -Z & 0 \end{bmatrix}$$

In the 2D case there is a principal axis system in which two independent polarization (or modes) can be separated (see Figure III.4). If σ=σ(y,z) (z vertical) we have:

(a) currents flowing along the strike (x̂)

$$\mathbf{J} = \sigma E_x \hat{x}$$

where

$$\mathbf{E} = (E_x, 0, 0) \qquad \mathbf{H} = (0, H_y, H_z)$$

This is called the "transverse electric" or TE mode.

(b) currents flowing perpendicular to the strike

$$\mathbf{J} = \sigma \mathbf{E}$$

where

$$\mathbf{H} = (H_x, 0, 0) \qquad \mathbf{E} = (0, E_y, E_z)$$

This is called the "transverse magnetic" or TM mode.

If the 2D impedance tensor is measured in a coordinate system aligned with the strike (the principal axis system) it becomes

$$\mathbf{Z}_{\text{principal axis system}} = \begin{bmatrix} 0 & Z_{xy} \\ Z_{yx} & 0 \end{bmatrix}$$

And equations (III.4) reduce to:

$$E_x = Z_{xy} H_y$$

$$E_y = Z_{yx} H_x$$

In the 3D case, all elements of $\mathbf{Z}$ are, in general, non-zero. The frequency-dependence of the impedance tensor contains the information about the 2 or 3-D electrical structure, although not in a simple way as in the halfspace case.

4. INFORMATION FROM THE VERTICAL MAGNETIC FIELD: MAGNETO-VARIATIONAL METHOD (OR MV)

The $\hat{z}$ -component of

$$\nabla \times \mathbf{E} = i\omega\mu_0 \mathbf{H}$$

plus the fact that

$$\mathbf{E} = \frac{1}{\sigma} \nabla \times H$$

implies that

$$H_z = M_{zx} H_x + M_{zy} H_y$$

For the 1D case, E_y and E_x are horizontally uniform and there is no vertical magnetic field. For the 2D TM mode with $\sigma = \sigma(y,z)$, $E_x = 0$ and $E_y = E_y(y,z)$. Thus H_z is also zero. Thus an observed vertical magnetic field is the result of electrical currents flowing along the strike and is one aspect of the TE mode.

In the more general situation, H_z is related to the horizontal magnetic fields by the Weiss-Parkinson relationship

$$H_z = M_{zx} H_x + M_{zy} H_y = \mathbf{M}^T \mathbf{H}$$

where the complex vector

$$\mathbf{M} = \begin{bmatrix} M_{zx} & M_{zy} \end{bmatrix}$$

is commonly written as the complex Parkinson vector

$$\mathbf{P} = M_{zx}\hat{x} + M_{zy}\hat{y}$$

It follows from our discussion above that in 2D ($\sigma = \sigma(y,z)$)

$$\mathbf{M} = [\ 0\ , M_{zy}\ ]$$

and both the real and imaginary parts of $\mathbf{P}$ are perpendicular to the strike (see Figure III.5).

Thus in more general 3D situations, the lack of co-linearity of the real and imaginary parts of $\mathbf{P}$, are a measure of the departure from 2D. $\mathbf{P}$ will point away from linear current concentration (although many authors reverse the sign of $\mathbf{P}$ so that it points towards such currents). One also show, that the real part of $\mathbf{P}$ responds primarily

to currents flowing a depth, while the imaginary part of **P** responds to currents flowing near the surface.

5. ESTIMATING Z AND M FROM THE DATA

The linearity between components of the electromagnetic fields is a result of the linearity of the governing physical equations. However E and H are typically not stationary in time. Thus the estimation of Z and M which contain presumably stationary geological information, is a statistical problem. We can write

$$E_x^i = Z_{xx} H_x^i + Z_{xy} H_y^i + r_x^i$$

$$E_y^i = Z_{yx} H_x^i + Z_{yy} H_y^i + r_y^i$$

and

$$H_y^i = M_{zx} H_x^i + M_{zy} H_y^i + r_z^i$$

where i denotes one of N quantities obtained by breaking the original time series up into N segments, applying an appropriate taper to the ends, and Fourier transforming to the frequency domain. **r** is the residual due to the imperfect prediction of **E** (or H_z) from **H**. Each of these equations has the form

$$e = Hz + r$$

where **e** and **r** are $Nx1$ vectors, **H** is an $Nx2$ matrix and **z** is a $2x1$ vector. The solution

$$Z = (H^T H)^{-1} H^T e$$

minimizes the mean square residual $r^T r$, where the **T** symbol means the Hermitian

transpose

(transpose plus complex conjugate).

If the assumption of independent, identically distributed Gaussian errors is valid, then the estimate given by this Least Square method is the best among all other estimates. However, the Gaussian assumption is not necessary correct, and, in fact, significant outliers are to be expected. These outliers may strongly perturb the estimates because Least Square estimates are well-known not to be statistically robust. The solution is to use a robust method that tests the Gaussian error distribution assumption, isolates the outliers and down-weights them automatically *(Egbert and Booker, 1986; Chave, et al., 1987; Thomson & Chave, 1989, 1991)*.

6. REGIONAL AND LOCAL STRUCTURES: DECOMPOSITION OF THE IMPEDANCE TENSOR

Experimentally determined impedance tensors (**Z**) rarely have the 2D form with zero diagonal elements. This may due to not being in the principle coordinate system, to 3D effects or data errors. If the regional structure is 1D or 2D, it is sometimes possible to extract the regional 1D or 2D impedance from the measured data.

Larsen (1977) first pointed at that certain types of 3D structure acting at the surface of a 1D earth would multiply the impedance tensor by a distortion matrix **C** whose elements were real and frequency independent.

Specially, the 3D structure must be of sufficiently small scale that its response is entirely due to the accumulation of electric charge at boundaries (or high conductivity gradients). These charges are the result of the physical requirement that the normal

component of the electric current must be continuous. Thus **E** will be discontinuous if σ is discontinuous.

A discontinuity in the normal component of **E** implies a surface charge. The MT response of such surface charges is called "galvanic" and is really a DC effect. It will thus be independent of frequency and not affect the phase of the fields.

Following Larsen's early ideas, *Bahr (1988), Groom and Bailey (1989, 1991)* and *Chackridi, et al. (1992)* have generalized Galvanic distortion to the case of a regional 2D impedance tensor. The measured impedance tensor is written

$$\mathbf{Z_m = R \, C \, Z_2 \, R^T} \qquad \text{(III.5)}$$

where **R** is a unitary rotation matrix from the principle coordinate system of the underlying regional 2D impedance $\mathbf{Z_2}$ to the coordinate system in which $\mathbf{Z_m}$ is measured. **C** is the same, real distortion matrix considered by Larsen.

The measured impedance has 8 numbers (the real and imaginary parts of its 4 elements). The right-hand-side has 9 parameters (the angle between the coordinates system, the 4 real elements of **C**, and the real and imaginary parts of the two off-diagonal elements of $\mathbf{Z_2}$). Thus this parameterization is not unique.

Groom and Bailey *(Groom & Bailey, 1989)* presented a decomposition for **C**, based on the separation of local and regional parameters characterizing the structure:

$$\text{(III.9)} \quad \mathbf{C} = g \begin{bmatrix} 1 & -t \\ t & 1 \end{bmatrix} \begin{bmatrix} 1 & e \\ e & 1 \end{bmatrix} \begin{bmatrix} 1+s & 0 \\ 0 & 1-s \end{bmatrix}$$

The local parameters are the shear angle $\psi_e = \tan^{-1}(e)$ and the twist angle $\psi_t = \tan^{-1}(t)$. The strike angle θ is a regional parameter. Both s and g are the two scaling parameters that cannot be determined, and are arbitrary set to 0 and 1. This means

that their influence is absorbed into $\mathbf{Z_2}$ and each element of $\mathbf{Z_2}$ is, in effect, multiplied by an unknown real constant called a "static shift". If the 3D-effects are truly frequency-independent the regional 2D tensor can be recovered except for the static shifts, i.e. scaling factors. The seven unknown parameters are θ, ψ_e, ψ_t, and the complex off-diagonal elements of $\mathbf{Z_2}$. These parameters are obtained by statistically fitting the eight data (real and imaginary parts of the measured impedance, $\mathbf{Z_{measured}}$). The idea is to find the simplest distortion model (for a certain frequency band) which occurs when the *twist, shear* and *strike,* are frequency independent *(Jones & Groom, 1993).*

There are various ways in which deviation from ideal distortion models can be detected. In practice, a structure that acts as part of the regional inductive structure at high frequencies may act as a frequency-independent distortion structure at much lower frequencies. The analysis of the frequency-dependence of θ and the local parameters, twist and shear, is thus very important.
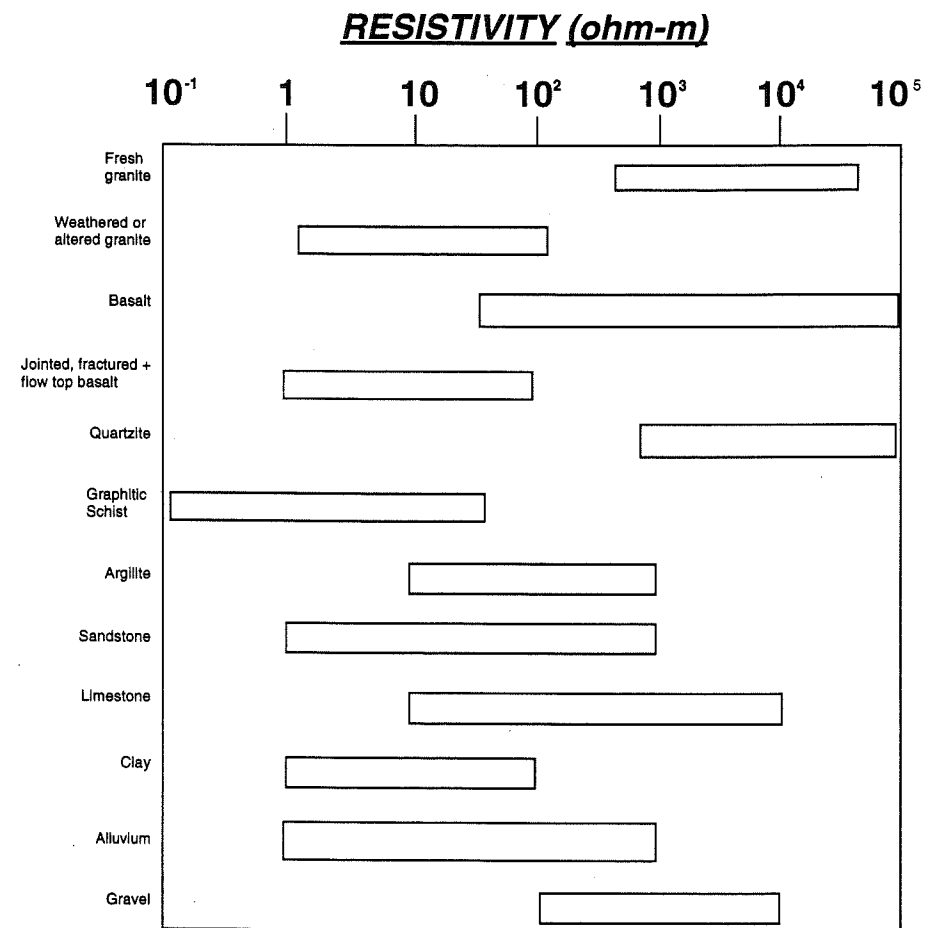
RESISTIVITY (ohm-m)

FIGURE III.1

Resistivity for most of the common materials encounterd in the earth
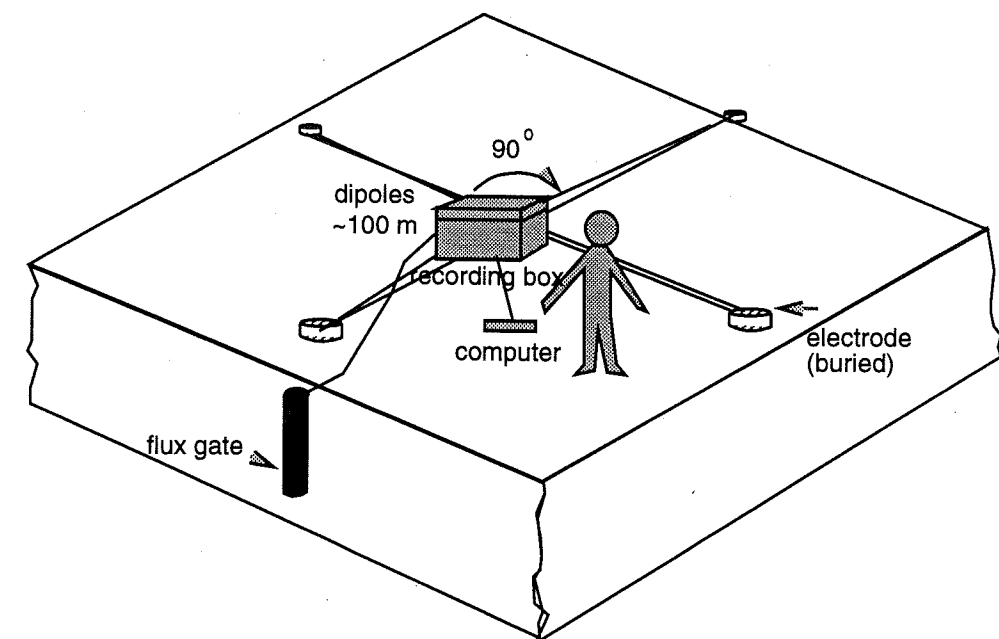
FIGURE III.2

Magnetotelluric Recording System: Fluxgate measures the magnetic components, orthogonal dipole the horizontal spatially averaged electric fields as the voltage difference between electrodes divided by the lengh of the legs.
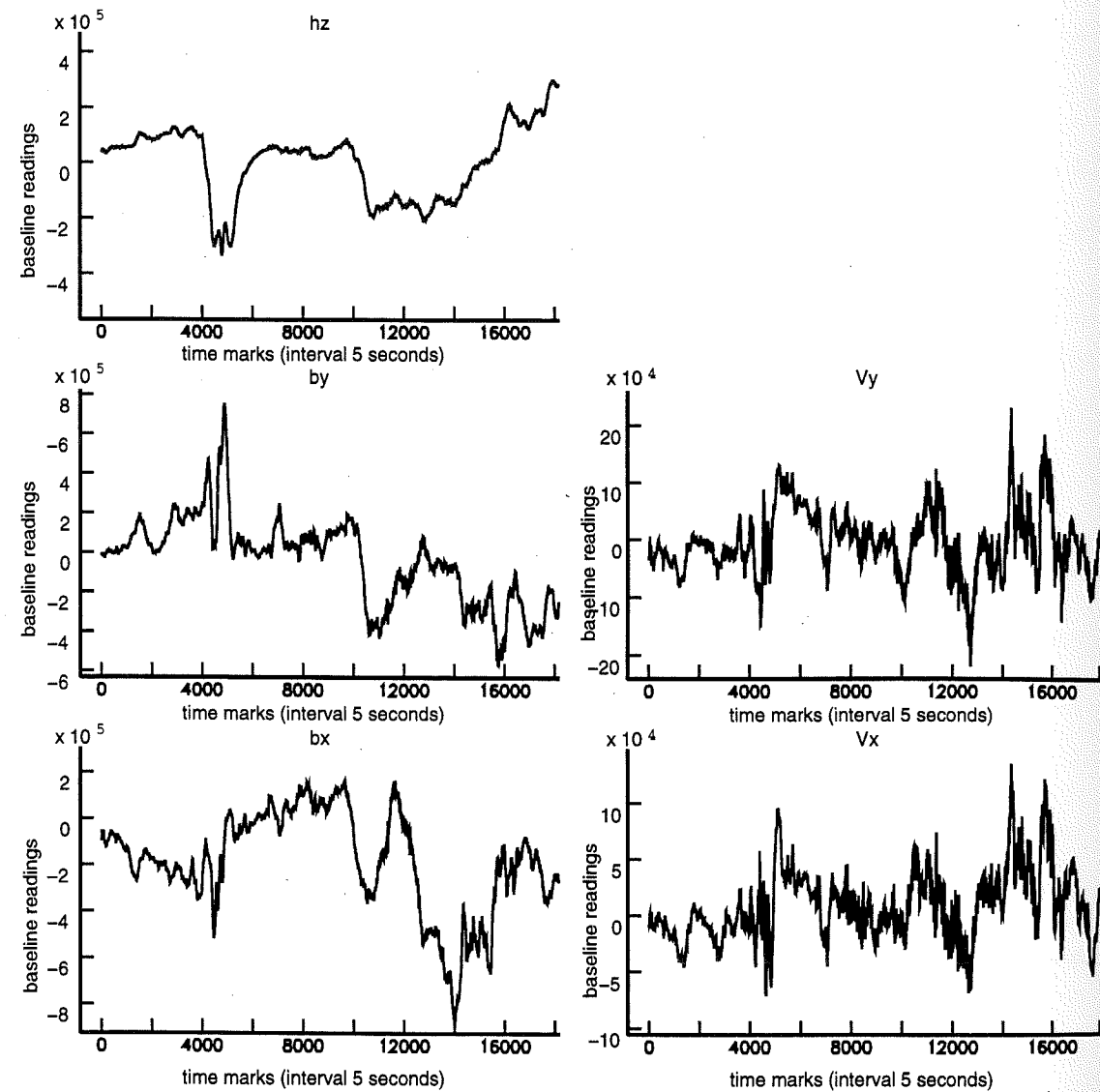
FIGURE III.3

Baselines readings for station POM 280. The sample interval is 5s. One unit in the reading is equivalent to one millivolt. Voltages (Vx and Vy) are converted to the usual unit for the electric fields (Ex and Ey) by expressing the lenght of the electrodes in meters. To convert {bx, by. bz} readings into magnetic induction, a conversion factor of must be applied.
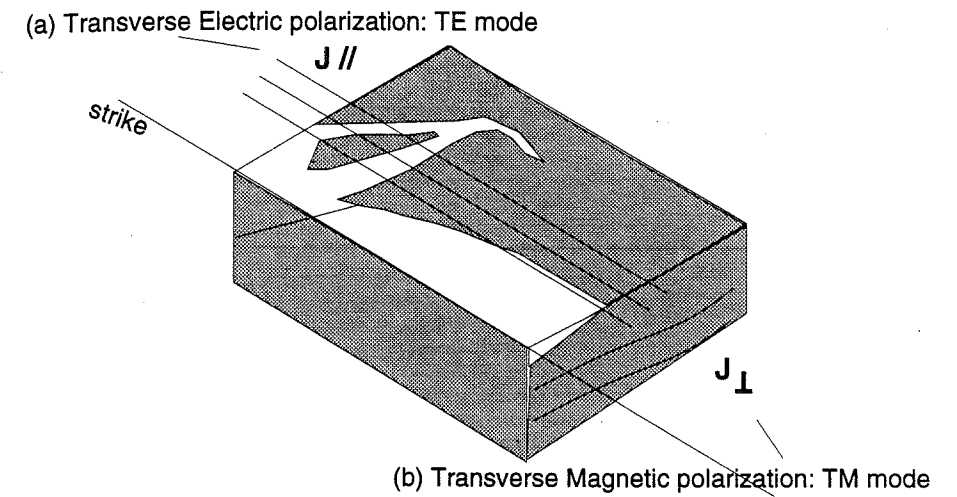
FIGURE III.4

In a regional 2D structure the responses can be separated into two approximately independent modes (exactly independent in a true 2D structure):
(a) Transverse electric (TE), currents flow parallel to the regional strike
(b) Tranverse magnetic (TM), currents flow perpendicular to the strike .

$$Hz\ (w) = (\ Mzx * Hx + Mzy * Hy\ )\ (w)$$
w: frequency
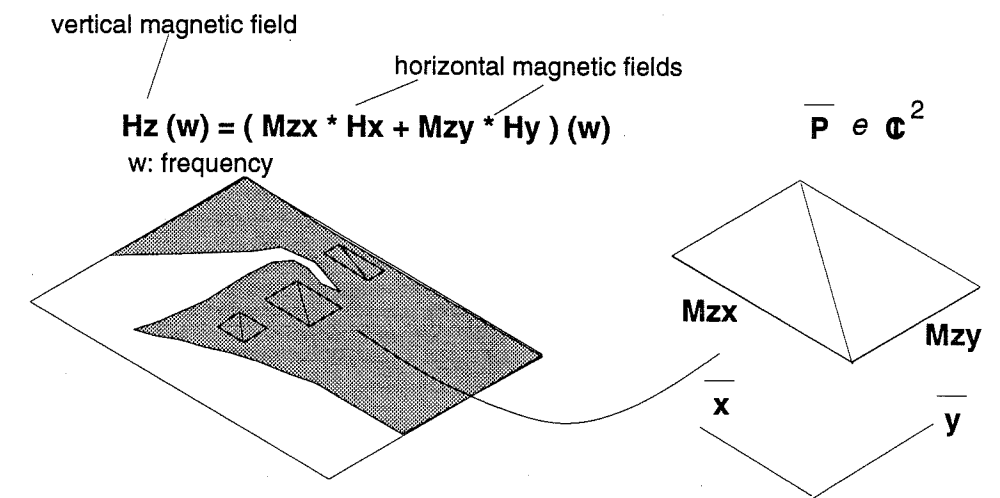
FIGURE III.5

Parkinson complex vectors (defined in text and in the figure) . In the 2D case they are orthogonal to the strike. The lack of co-linearity is a measure from 2D.

CHAPTER IV

POM MT SURVEY DATA COLLECTION AND DATA ANALYSIS

1. INTRODUCTION

As outlined in Chapter I, the picture of the Cascadia subduction zone is still incomplete. For example, how deep and how much further to the east does the subduction complex extend? Do the Core rocks squeeze beneath the Peripheral rocks? How deep and how much further to the east do the Peripheral rocks extend? What kind of material makes up the deeper structure beneath the Puget lowland? What type of structure determines the occurrence of crustal earthquakes typical of this area? Finally, what are the characteristics of the transition zone between the studied area and the pre-Tertiary continental crust to the east?

A considerable amount of data, which I reviewed in Chapter II, already exist to address these questions. However, definitive answers have not yet been given. It is to be expected that high contrasts in electrical conductivity exist been important features of this structure, such as the Olympic Core and the Peripheral Rocks and between the Peripheral rocks and the shallow sediments of the Puget lowland. It is therefore quite plausible that a geophysical method such as MT, which is sensitive to electrical conductivity, can image structural features that may be very useful in answering some of the questions posed above.

2. EXPERIMENTAL DESIGN AND DATA COLLECTION

Because fully 3D interpretation of MT data is still in its infancy, the POM MT project was designed to cross the study area in a manner that would permit useful conclusions to be drawn from 2D interpretation. In a gross sense, the ocean, the subduction complex and the Coast Range terrane define an approximately north-south strike. Previous MT transects *(Kurtz, 1988; Wannamaker, et al., 1989)* drew reasonable conclusions with an assumption of 2D structure. However, these earlier studies were in areas (Vancouver Island and central Oregon), where the reasonableness of such an assumption is more obvious. There was concern when planning the POM experiment that the area has significant 3D structure. Known 3D structures include (a) the arch in the slab beneath the Olympic Mountains; (b) the change in direction of the subduction zone; (c) the crescent shape of the Peripheral and Core Rocks; (d) the Puget Basin; (e) the sea water in the Straight of Juan de Fuca and Puget Sound.

Wannamaker, et al., (1984) show that 2D interpretation should result in a reasonable estimate of a slice of a 3D body if the 3D body is more conductive than its host, the transect is reasonably close to the center of the body and the interpretation concentrates on the TM mode (defined as the polarization with electric field along the transect). The POM MT line was located to take as much advantage of this result as possible. For instance, east-west (TM) currents in the Olympic Core will be blocked by the Peripheral rocks whether this feature is just north-south or whether it wraps around the Core to the north and south. Thus the 3D nature of the Peripheral rocks can be expected to be secondary for TM mode data on a transect along the axis of symmetry of the conductive Olympic Core. The same thing holds for the Puget Basin. If the transect crosses its center, we expect that resistive rocks to the north and south will have

essentially no effect, because there is no current flowing in them.

Unfortunately the considerations just discussed are conflict with other constraints, such as the difficulty of access in the central Olympic Peninsula and the potential for electrical noise generated by large centers of population. The actual profile is therefore a compromise. It runs perpendicular to the gross north-south geologic strike; runs approximately along the axis of symmetry of the slab arch and the crescent shape of the Peripheral rocks and across the center of the deepest part of the Puget Basin. This necessitated installing one critical site (POM245) in the Olympics by helicopter, but still left a significant gap in the profile in the center of the Core and required us to collect data in the metropolitan Seattle area. Not being able to avoid Seattle degraded some sites somewhat, but turned out not to be as big a problem as initially feared due to the fact that we were not collecting high frequency data.

Twenty MT sites were collected along an approximately 230 kilometers profile. Except for the 40 kilometers gap in the Olympic National Park, the average site spacing is about 5 kilometers. The two horizontal components of the electric field and the three components of the magnetic field were measured at each station in the Geomagnetic coordinate system. Electric and magnetic field time-series data were digitally recorded using Long Period Intelligent Magnetotelluric Systems (LIMS) belonging to the Geological Survey of Canada.

The digitization rate was 5 seconds and the shortest period estimates were centered at 20 seconds. This implies a penetration depth of about 5 kilometers in material that is at the conductive end of what is expected (5 ohm-m). Since this depth is comparable to the site spacing, the shortest period data are sampling the material between all the sites, except in the Olympic gap.

Data were recorded for up to 10 days with the goal of obtaining precise (a few percent or better) MT responses to about 10,000 seconds. This would correspond to a penetration depth exceeding 100 kilometers in 5 ohm-m rocks, assuring us of the ability to see through such structure as the Olympic Core to the mantle below. Unfortunately, a variety of problems limited recording at some sites to as little as 2 days. Additionally, we had sites with noise problems that also limited the data precision. These include electrical noise in the metropolitan areas and temperature effects resulting from our inability to bury equipment sufficiently in environmentally sensitive areas, such as the Olympic National Park and Forest. Nevertheless, data precision of 5% or better were obtained to 3,000 seconds at almost all sites. This is still adequate to ensure that we can see through the Olympic Core and the Puget lowland conductors.

The magnetic field was measured using a Narod fluxgate magnetometer. The magnetometer was generally buried in a vertical hole with the sensor about 50 centimeters below the surface and was accurately aligned with the background geomagnetic field. Aside from temperature variations that are reduced by burial, the main source of magnetic noise is tilting of the sensor in the main geomagnetic field. This can be a serious problem in forests, where wind acting on trees causes local tilts. However, such noise should not be coherent with the electric field. Environmental regulations in the National Park and Forests prevented burial of magnetometers. They were instead installed in a bucket filled with sand. This protected the sensor against thermal noise, but made vibration problems worse.

Electric fields were measured as a voltage difference along orthogonal dipoles. The dipoles were typically 100 meters long grounded at the end with lead electrodes in a plaster-of-paris matrix saturated with lead chloride to reduce the chemical contact

potential. Electrodes were buried approximately 30 centimeters to reduce the effect of diurnal and other temperature changes and provide good contact between the matrix and damp soil. The data loggers were also partially buried and were insulated using plastic bags filled with foam peanuts to protecting them from temperature fluctuations.

Sites were selected for their accessibility, flatness (in order to deploy the dipoles), and isolation from possible electrical noise contamination sources (such as electrical pumps, voltage generators, etc.) and from animal or human interference (cows or wild animals chewing cables, etc.). To allow magnetic noise contamination to be removed from the data, a simultaneous recording of the three components of the magnetic field was done at another station far away from each MT site. However, when I processed the data, I found that this "remote reference" made no significant difference, indicating that the noise was almost entirely confined to the electric fields.

3. TIME SERIES ANALYSIS

The first stage of MT interpretation is to Fourier transform E and B from the time to frequency domain. The complex relationship between the horizontal components of these fields in the frequency domain is the MT impedance. After uploading the digital time series data at each site to a portable computer, preliminary estimates of the apparent resistivity and phase were calculated to give a quick indication that the data were acceptable and that the instrument could be moved to another site. The coherences between the E and B fields were also estimated to indicate the quality of the data. A good coherence should be of the order of 0.99, although a lower limit of about 0.9 can be used.

The data were later re-processed using a statistically robust code *(Egbert and Booker, 1986)*. The steps in this re-processing of the data consist of:

(a) Cleaning the data (removing spikes and obvious problems such as parity errors).

(b) Pre-whitening (because the magnetic field spectrum rises rapidly with period).

(c) Cascade decimation. To make the robust code work, we want to use the shortest time windows allowed by the period being studied. This is because the non-Gaussian outliers are commonly of short time duration and much easier to identify in Fourier transforms of short time windows. However, as the period gets longer we must use longer windows. To reduce the numerical effort, it is convenient to apply digital anti-aliasing filters and decimate the data before the longer time segments are windowed and Fourier transformed. I use 128 points in each time window and decimate the data by four at each stage.

(d) Calculation of the Fast Fourier Transform of the windowed segments.

(e) Iterative re-estimation of the transfer functions by stacking estimates from each windowed segment. Segments that stand out as non-Gaussian outliers in the stack are down-weighted in a manner called Huber's M-estimate.

Figure IV.1 shows the coherence between the magnetic component H_y and the electrical component E_x (c_{xy}) and between H_x and E_y (c_{yx}) for station POM105. The coherence for most of the stations are very close to 1 as we want. Low coherence (less than 0.95) at longer periods is due to inadequate recording time. Occasional low coherence at other periods is due to noise. In such cases, identification of a small number of time segments with low coherence and their elimination from the stack can substantially improve the estimates. Figure IV.2 shows the coherence for site POM160 before and after "good" time-series segments were selected. This site is in Discovery Park in

the city of Seattle and the "X" electric fields are contaminated by a noise source, which is probably a water pump using cathodic protection near the northern-most electrode. The existence of such a potential problem was not known to the park personnel who suggested the particular site. Despite the fact that the coherence in this component is very low by normal MT standards, the robust code appears to have been able to discriminate against the bad data that remain and produce what appear to be good estimates at this site.

4. TENSOR DECOMPOSITION

As discussed at the beginning of this Chapter, the POM project was laid out to maximize the likelihood that a 2D interpretation would be adequate. However, 3D effects make themselves felt in the data. Thus the second stage in MT interpretation must be to test whether the data are compatible with a 2D interpretation.

In Chapter III, I discussed the fact that truly 2D structure does not exist in nature. In particular, we almost always can expect small scale, near surface 3D structure to cause Galvanic distortion even when the underlying regional structure is 2D. Small scale in this context means smaller than the skin depth in the host. In the POM, experiment, we can expect that structures as large as the sea water in the Puget Sound will be Galvanic distorters at the periods we are using. This is actually fortunate, because when the Galvanic 3D distortion model holds, one can extract the 2D regional impedance (within unknown constant factors called static shifts). The measured impedance is related to the regional 2D impedance through a unitary rotation matrix and a real distortion matrix, which involves two recoverable parameters called twist and shear by *Groom and Bailey (1989)* as well as the two static shifts. A necessary

condition for Galvanic distortion is that the twist, shear and strike be frequency-independent. This can be tested with the data.

I used a code written by Chave (see *Chave and Smith, 1994*) to estimate the twist and shear and regional strike at each site. This was first done for each frequency to test whether these parameters were frequency-independent as the Galvanic distortion model requires. For reasons that will become clear, I then repeated the decomposition with additional constraints.

4.1. Unconstrained Groom-Bailey decomposition

Figure IV.3 shows the estimated strike and distortion parameters, twist and shear as a function of period and site. This sort of summary plot of all the data is called a pseudosection. The strikes are clockwise relative to Geographic North. Note the gap in the profile (no data) in the center of the Olympic Peninsula. We hope that twist and shear are frequency-independent, but we expect them to vary form site to site, since they depend on structure very close to each site. Thus the pseudosections of twist and shear should look like a series of vertical color stripes. We also hope that the regional strike is the same at all sites and all frequencies. Thus the pseudosection of strike should be all one color. At some sites and in some frequency ranges the pseudosections do look as we hope, but at others they do not. The behavior can be broken down into several groups:

(a) *Western Section (sites POM280 to 249)*

This group of stations is located in the western part of the Olympic Peninsula, (Core rocks of the Olympic Peninsula). Figure IV.4a shows the distortion parameters as a function of period. The decomposition appears to be reasonably valid,

with twist and shear fairly constant for all sites except POM250 except at the longest periods. At the long periods, the parameter estimates are poor because the error estimates for the impedance data are large and so the observed frequency-dependence is meaningless.

(b) *Peripheral Section (sites POM245 to 210)*

This group comprises the eastern Olympic Core and the sites in the Peripheral rocks. It is clear from Figure IV.4b that there is frequency-dependence covering most of the period range.

(c) *Eastern Section (sites POM200 to 105)*

This section covers the Puget lowland up to the foothills of the western Cascades. Figure IV.4c shows strong frequency-dependence at the western end of this section, smooth functions for both twist and shear at sites POM200, POM180 and POM170 and diverse frequency-dependent behaviors at the remaining sites.

Based on these observations, one might conclude that the Galvanic distortion model is untenable. However, fitting the distortion model to the measured impedance involves solving for 7 parameters with 8 data (see Chapter III). The strike is associated with a small eigenvalue of the linear system and is consequently often unstable in the presence of even a small amount of noise *(Jones & Groom, 1993)*. Thus the significant frequency-dependence just noted may be the result of poor estimation of strike, rather than true frequency-dependence.

4.2. Constrained Groom-Bailey decomposition

One can imagine several ways to try to stabilize the strike calculation. One could simply assume that the parameters are frequency-independent over a band and do the least squares problem again. The problem with this is that it gives little insight into when the assumption is wrong. Alternatively, one could simply assume that the strike is the same at all sites and frequencies and simply do the coupled least squares problem for the a single strike for all sites and the twist and shear at each site. Again, one would like a method that gives insight into whether the assumption is a good one. Jones and Groom (1993) advocate estimating a frequency-independent initial estimate of twist and shear by taking the average of these parameters in period ranges where they are nearly constant. The twist and shear are then constrained at these values and the strike is re-estimated by re-solving the least squares problem. When a large number of sites are involved, this requires estimating a large number of parameters, which are non-linearly coupled to the unknown strike and at many of my sites do not initially seem to have any period range in which one can confidently say that the parameters are constant. I have therefore tried an alternate approach, which is more related to solving for a global strike, but which allows one to still test the frequency-dependence of twist and shear.

I first plotted histograms of the calculated regional strike for sites where twist and shear were weakly dependent on frequency. These histograms were plotted for groups of sites in several geographic areas These are shown in Figure IV.5a. Although these histograms are clearly not Gaussian, they all show a peak slightly west of Geographic North. Figure IV.5b lumps all the sites together. The median strike is −12°, which is very consistent with the peaks within the individual regions. Accepting this value for

the regional strike at all sites, I rotated the impedance tensors to this strike and re-estimated the twist and shear as a function of period holding the strike fixed.

The resulting twist and shear versus period are plotted on top of each other in Figures IV.6a, b and c. At sites in the *Western* and *Eastern* sections (Figures IV.6a and c), which already had slowly varying twist and shear, there is little change in these local parameters. The new estimates for twist and shear are substantially less frequency-dependent at sites POM110 and POM105. In the *Peripheral* section, however, there is a truly remarkable change in behavior. Sites that were formerly highly frequency-dependent have become only weakly frequency-dependent except at the longest periods, where the impedance estimates are poor. Sites POM220, POM230 and POM242 are particularly striking in this regard. It is thus evident that much of the frequency-dependence in these parameters was indeed due to instability of the strike determination. Pseudosections of the distortion parameters for both the unconstrained and constrained case are compared in Figure IV.7. The considerable decrease in frequency-dependence of the twist and shear when the strike is constrained to a reasonable global value is quite obvious.

Jones and Groom (1993) argue that when the true strike angle is known, statistically superior estimates of the regional impedances result when fitting the galvanic distortion model to the data, rather than rotating the measured impedance tensor to strike and then fitting the distortion model as I have done. The reason for this is that the data are weighted differently in the two coordinate systems. However, the rotation angle is so small that this is unlikely to be important in this case.

4.3. The diagonal elements of Z

Another test of the consistency of the Galvanic distortion model involves the phase of the diagonal elements of the impedance tensor. Equation (III.5) can be manipulated easily to give

$$\mathbf{R^T Z_m R = C Z_{2D}} = \begin{bmatrix} C_{xy}Z_{yx} & C_{xx}Z_{yx} \\ C_{yy}Z_{yx} & C_{yx}Z_{yy} \end{bmatrix}$$

Since the elements of **C** are simply real constants, we can immediately conclude that the diagonal elements of the measured impedance tensor rotated to strike should be the same as the off-diagonal elements in the same column except for a *different* static shift. In particular, this means that the phases of the off-diagonal elements should be identical to the phases of the diagonal element in the same column. This was first pointed out by *Bahr (1988)* in his seminal paper on 3D distortion. He advocated using this property as a means of estimating the strike. One should rotate the measured impedances until the phases in the appropriate elements were equal. Unfortunately, it is clearly unstable to do this and would, in fact, fail completely in the case that the measured impedance was 2D, because then the diagonal elements would be zero and have indeterminate phase. Tensor decomposition is often called Groom-Bailey decomposition, not because they invented the idea, but because they proposed a numerically tractable way to calculate the parameters.

Although Bahr's method for determining strike is not practical, it still provides a consistency check of the data once the strike has been determined. Figure IV.8 shows pseudosections of the phases of all four elements in the coordinate systems 12° west of Geographic North. Z_{xx} and Z_{yx} are reasonably similar. However, the modulus of Z_{yy} is

so small that its phase is dominated by noise and cannot be compared in any reasonable way to the phase of Z_{xy}. These data, are thus, a very clear example of why Bahr's method can fail.

5. INDUCTION VECTORS

I have transformed E and B time series into frequency domain impedances and performed tensor decomposition on these impedances to determine that the most appropriate 2-D strike direction is 12° west of Geographic North. I can further test the appropriateness of this strike direction by using independent information derived from the transfer function between the horizontal and vertical magnetic fields. This transfer function is neatly summarized in the Parkinson (induction) vector (see Chapter III).

As discussed in Chapter III, both the imaginary and real parts of the Parkinson vector are perpendicular to the strike direction for an ideal 2D structure. For real data we expect these vectors to be approximately normal to the regional 2D strike if there is one. Pseudosections of the angle of the Parkinson vectors with respect to Magnetic North are shown in Figure IV.9a. Relative to Magnetic North, a Parkinson vector normal to the Geographic strike of −12° should be +58.8° or −121.2°. These values correspond to yellows and blues on the color scale. In looking at the pseudosections, however, one must keep in mind that the Parkinson vector direction becomes unstable when the vectors magnitude is small (i.e. where is reversing its direction). Taking this into consideration, it is evident that the Parkinson vectors do generally support the regional strike determined by MT tensor decomposition. Figure IV.9b demonstrates this conclusion in another way. The Parkinson vectors along the profile are shown for several periods together with the direction that they should be parallel to if they are

normal to strike. For the most part, the vectors are closely parallel to the desired direction where they are large. This is more true for the real parts, which correspond to deep electric currents than for the imaginary parts that are more influenced by very shallow structure. I conclude that the induction vectors support my choice of regional 2D strike direction.

6. CONCLUSION AND DISCUSSION

Overall, the Groom-Bailey tensor decomposition supports a regional 2D model with an electrical strike of 12° west of Geographic North. Nevertheless, some non-Galvanic 3D effects may be present as indicated by sites that do not show a full frequency-independence in the calculated distortion parameters. Independently, the transfer function between the horizontal and vertical components of the magnetic field support the same regional strike.

From now on, *data* will refer only to the non-diagonal components of the measured impedance tensor rotated into the coordinate system with the horizontal $\hat{x}$ component parallel to 12° west of Geographical North or to quantities such as apparent resistivity and phase derived from these impedance elements. The two polarizations (modes) TE and TM will refer to the impedances with the electric field aligned with and normal to this strike. Note that our transect is close to, but not exactly aligned with the normal to strike. We will ignore this difference.

Figure IV.10 shows pseudosections of the measured TM and TE data. To convert these apparent resistivities and phases (functions of period) to true resistivity (a function of position and depth) requires forward modeling or inversion. However, we can already reach some conclusions regarding the geologic structure directly from these

raw data. I would like to point out the most striking features before proceeding with more complicated interpretation.

Consider first the TM mode. The apparent resistivity data clearly correlate with our expectations from surface outcrop. The Olympic Core is conductive, the Peripheral rocks are resistive, The Puget lowland is conductive and the foothills of the Cascades is again resistive. However, the fact that the very low apparent resistivity extends to very long period over the Peripheral rocks does not mean that this resistor is very deep. This low resistivity is largely a Galvanic response of charge accumulations at the east and west boundaries of the resistive zone and you will recall that the Galvanic response is frequency-independent. Phase is unaffected by the Galvanic response and thus more indicative of depth-dependence. We see that the TM phase everywhere initially decreases with increasing period. This implies that the model is getting more resistive with depth. One has to be quite careful about this last conclusion, however. This is because electric current induced in the very conductive ocean must cross the coast at very shallow depth. Two things could then happen. The current could be blocked with a very large charge accumulation at the coast or the current circuit can be completed by a current path across the entire model. This path can be shallow or deep. There is no evidence of a charge accumulation at the coast. On the contrary, the very low long period phase across the pseudosection is to a considerable extent, probably the result of the ocean electric current flowing at too shallow a depth to be in equilibrium with the *local* conductivity structure. The fact that the low phase persists across the model suggests that the current path is relatively shallow and is not down the slab as observed in Oregon *(Wannamaker, et al., 1989)*. The first element in this path is clearly the Olympic Core conductor, which can be thought of as an onshore extension

of the ocean. The very important influence of the ocean current source means that interpretation of the TM data absolutely require inclusion of the ocean in the model and make conclusions from 1D intuition suspect.

One must also be careful about simplistic interpretation of the TE pseudosections due to the likelihood of distortion by off-profile 3D structure. The vertical color stripes in the TE apparent resistivity are clear evidence of the presence of static shifts. However the TE apparent resistivity pseudosection shows generally the same pattern as the TM mode: conductive-resistive-conductive-resistive from west to east. The TE phase differs in several very significant ways from the TM phase. The very low long period phase is missing. This is not a surprise, because there should be no ocean currents in this polarization. Instead we see a long period rise in phase, which suggests a deep conductor that is stronger at the west and east ends of the profile. The TE phase at short period in the Puget lowland is also qualitatively different than the TM phase. This suggests a resistive, rather than conductive shallow structure. This is undoubtedly a 3D effect, since there is little question that the Puget lowland is a conductive sedimentary basin. The TE phase is probably due to the off-profile resistive shallow structure south of a major east-west fault zone south of our transect.
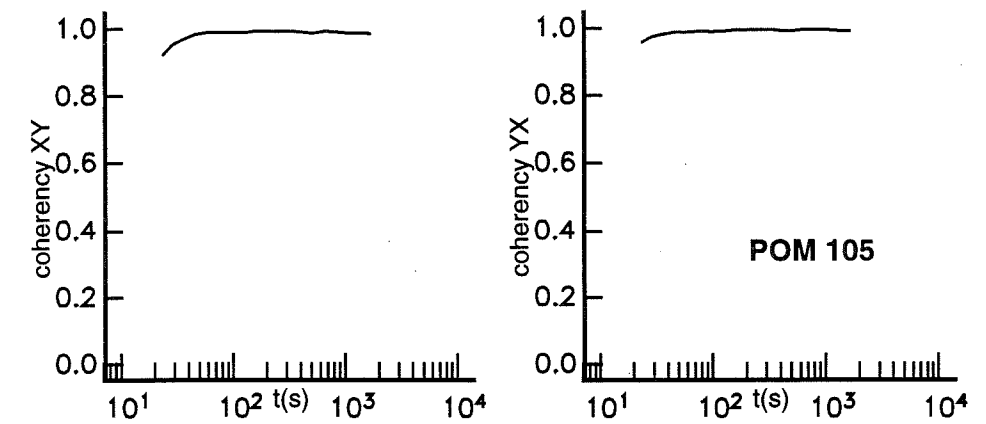
FIGURE IV.1
Coherency as a funtion of period for station POM 105: cxy and cyx
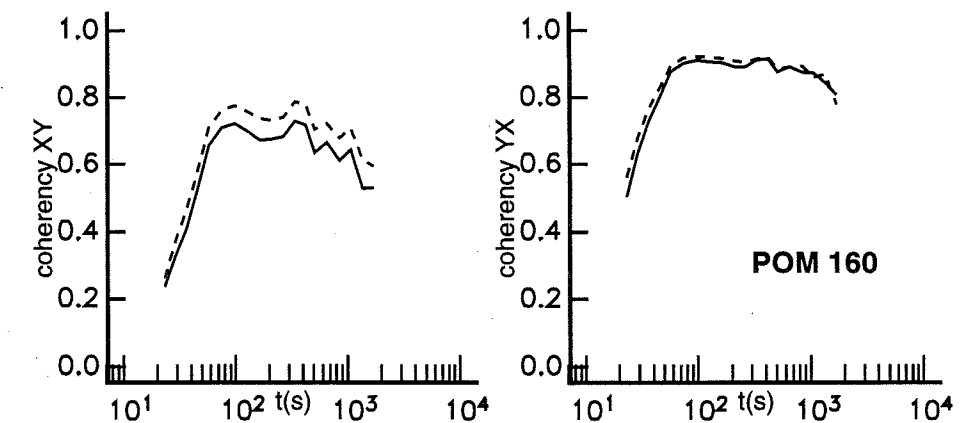
FIGURE IV.2
Coherency for station POM160 before (solid lines) and after (dashed lines) working with the time series selecting good intervals
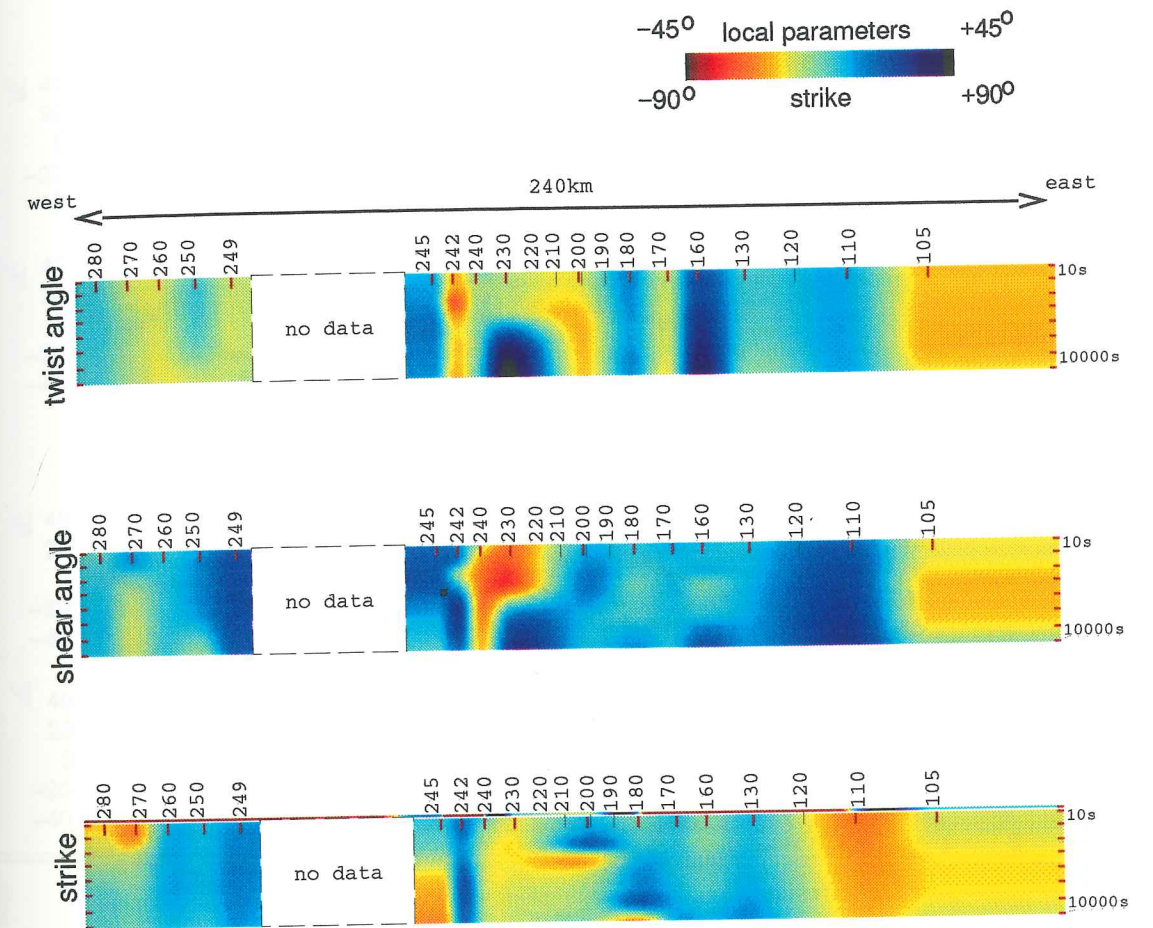
FIGURE IV.3
Local distortion parameters, twist and shear angles, and strike for
the Groom–Bailey decompostion
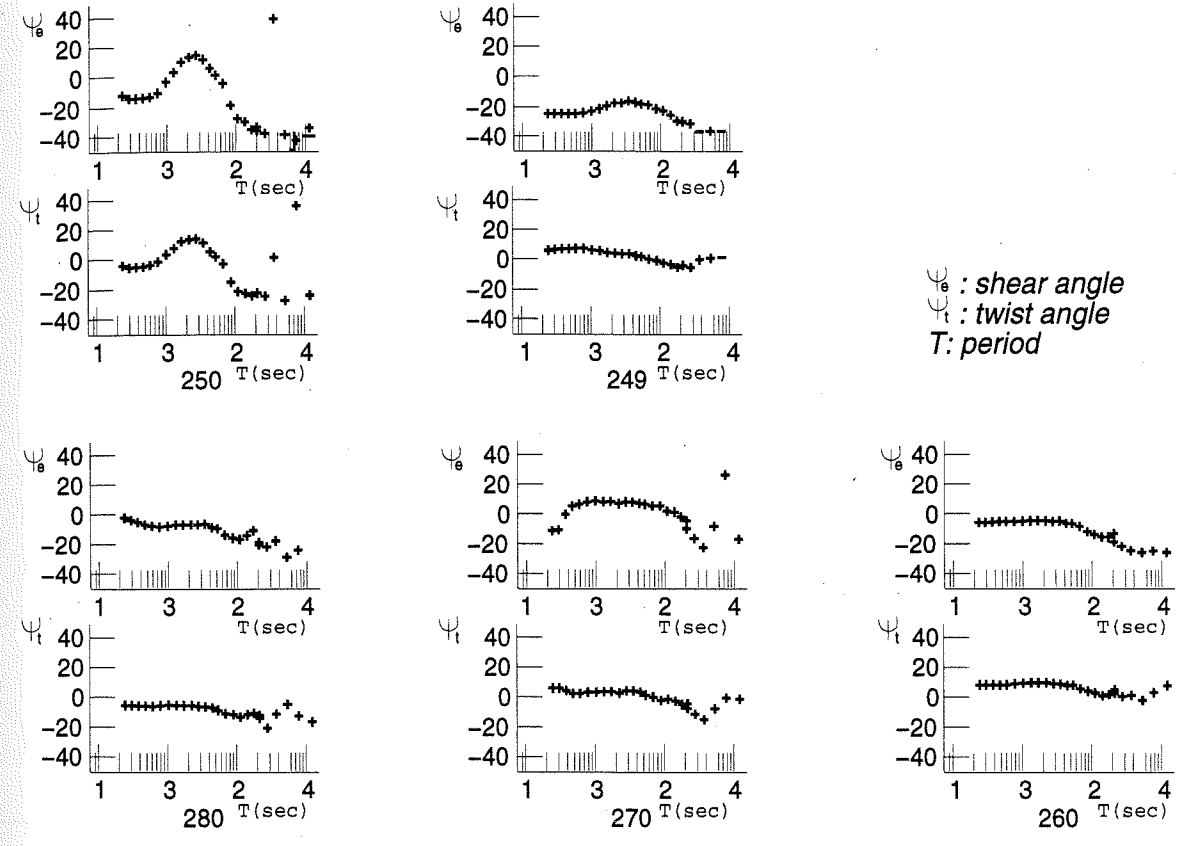
FIGURE IV.4a
Twist and shear angles for the western section: sites POM 280–to–249
Western part of the Olympic Peninsula
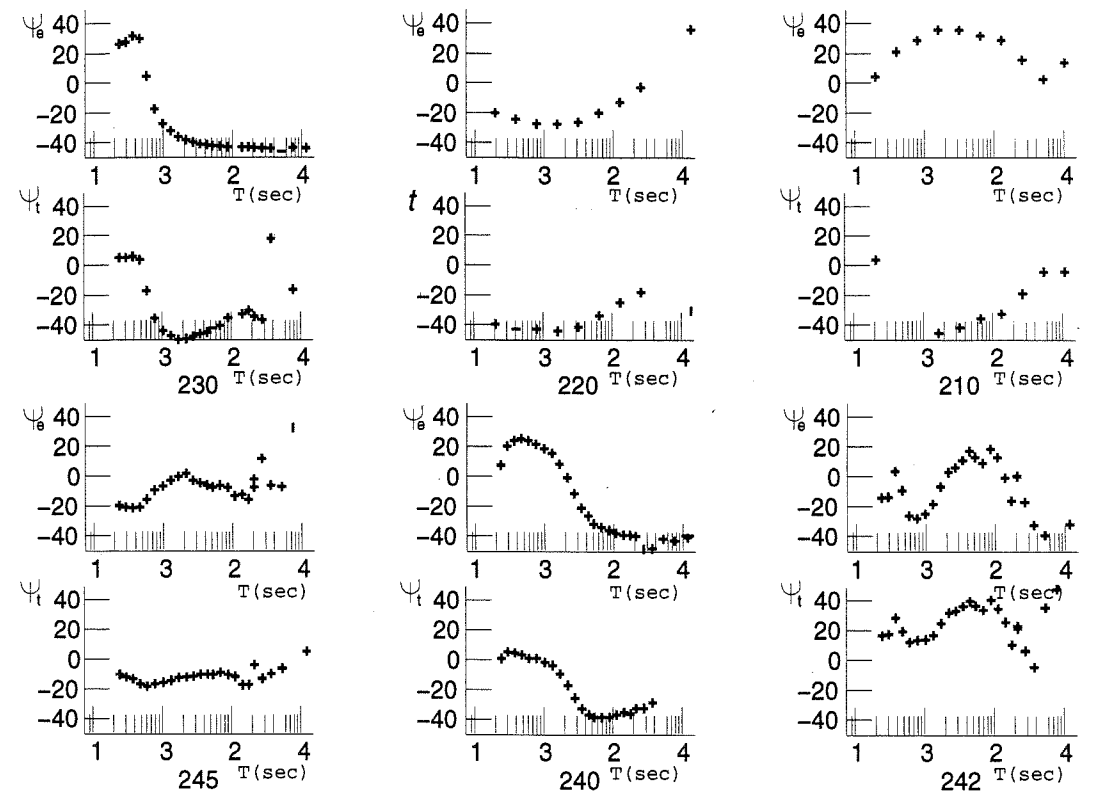
FIGURE IV.4b
Twist and shear angles for the Peripheral section: sites POM 245–to–210
(Eastern part of the Olympic Peninsula).
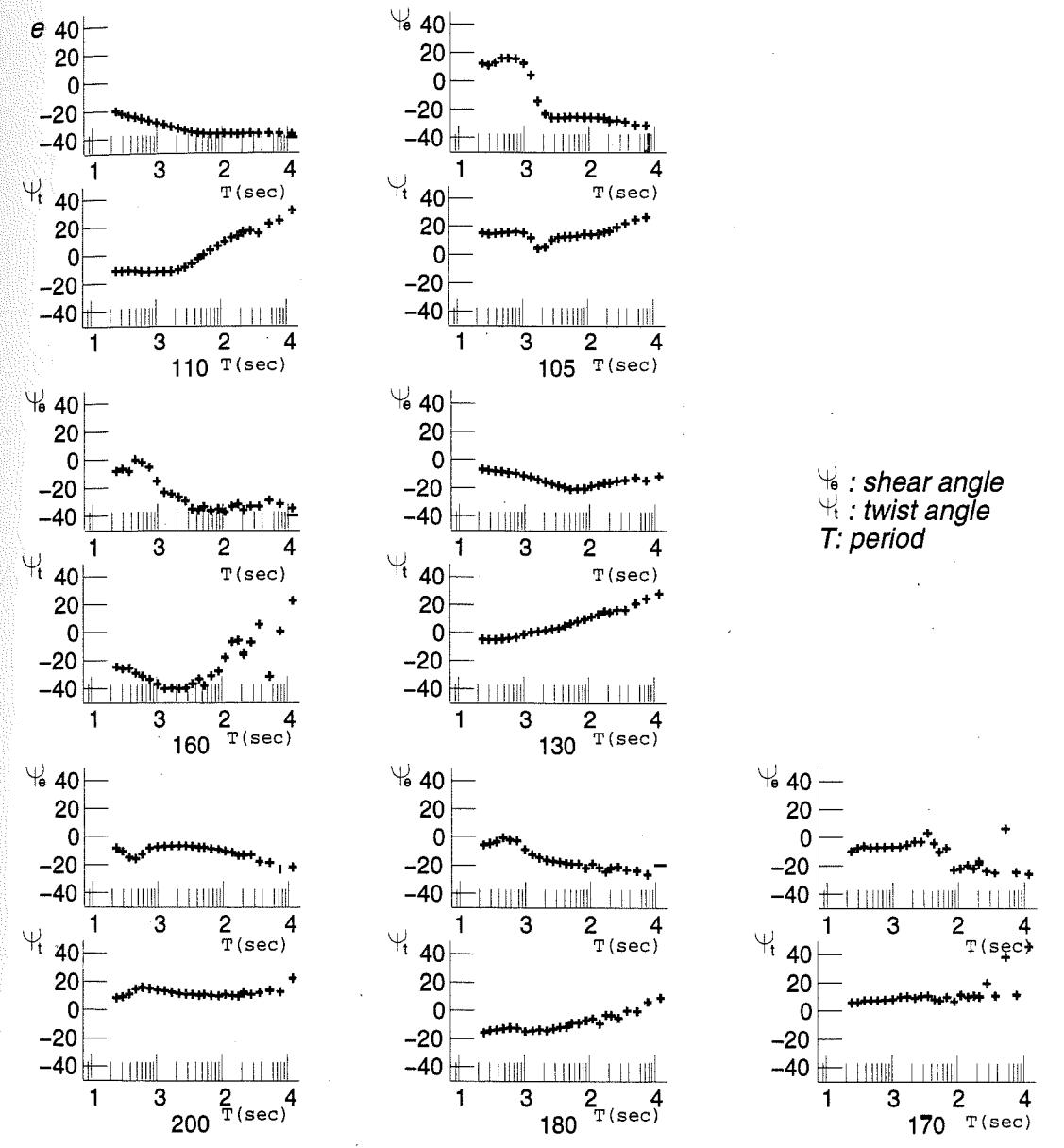
FIGURE IV.4c
Twist and shear angles for the eastern section: sites POM 200–to–105
Puget Lowland area.
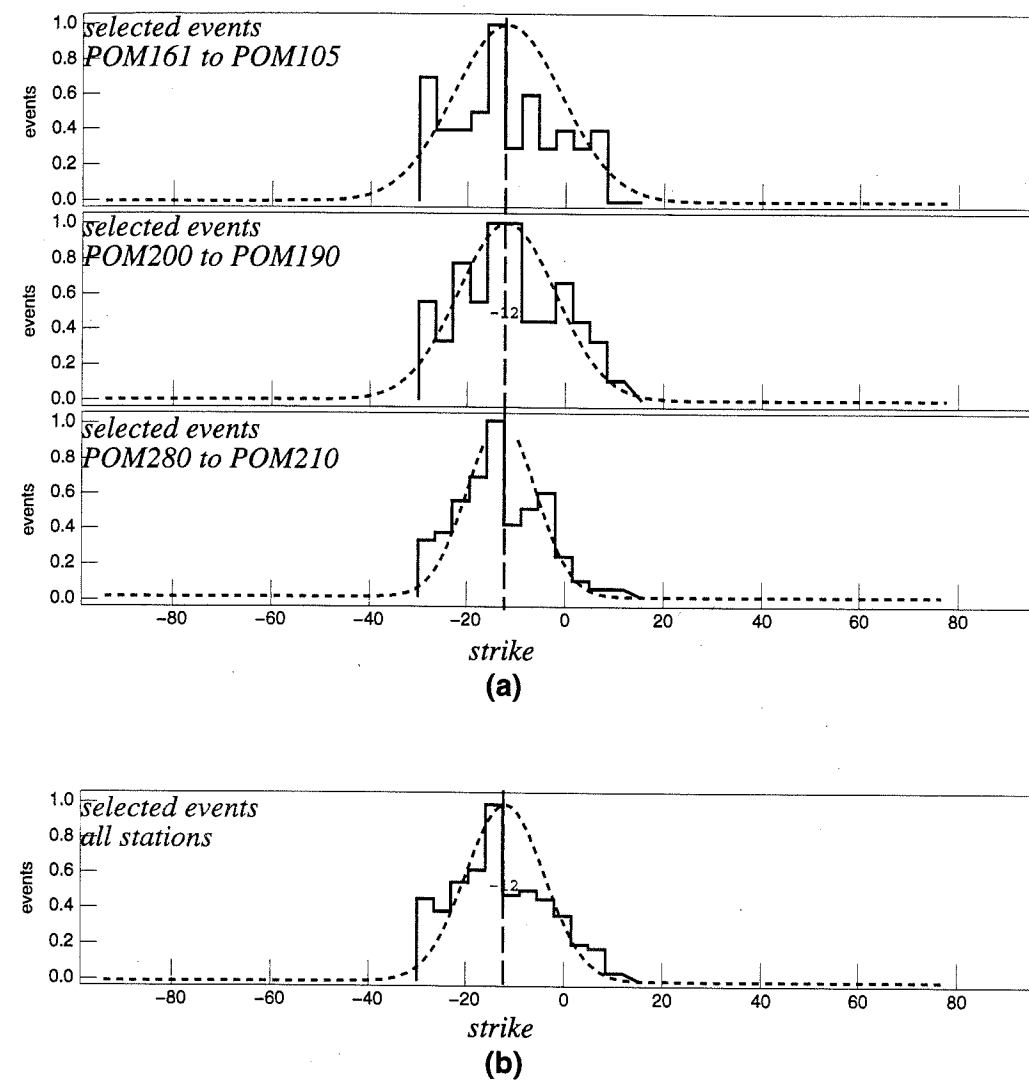
FIGURE IV.5

Histograms showing distribution of selected strikes at different geographical areas (a) and all stations (b). Gaussian bells shown as ilustration although the distributions are not Gaussian. Dashed vertical line corresponds to the' calculated median (−12 9.
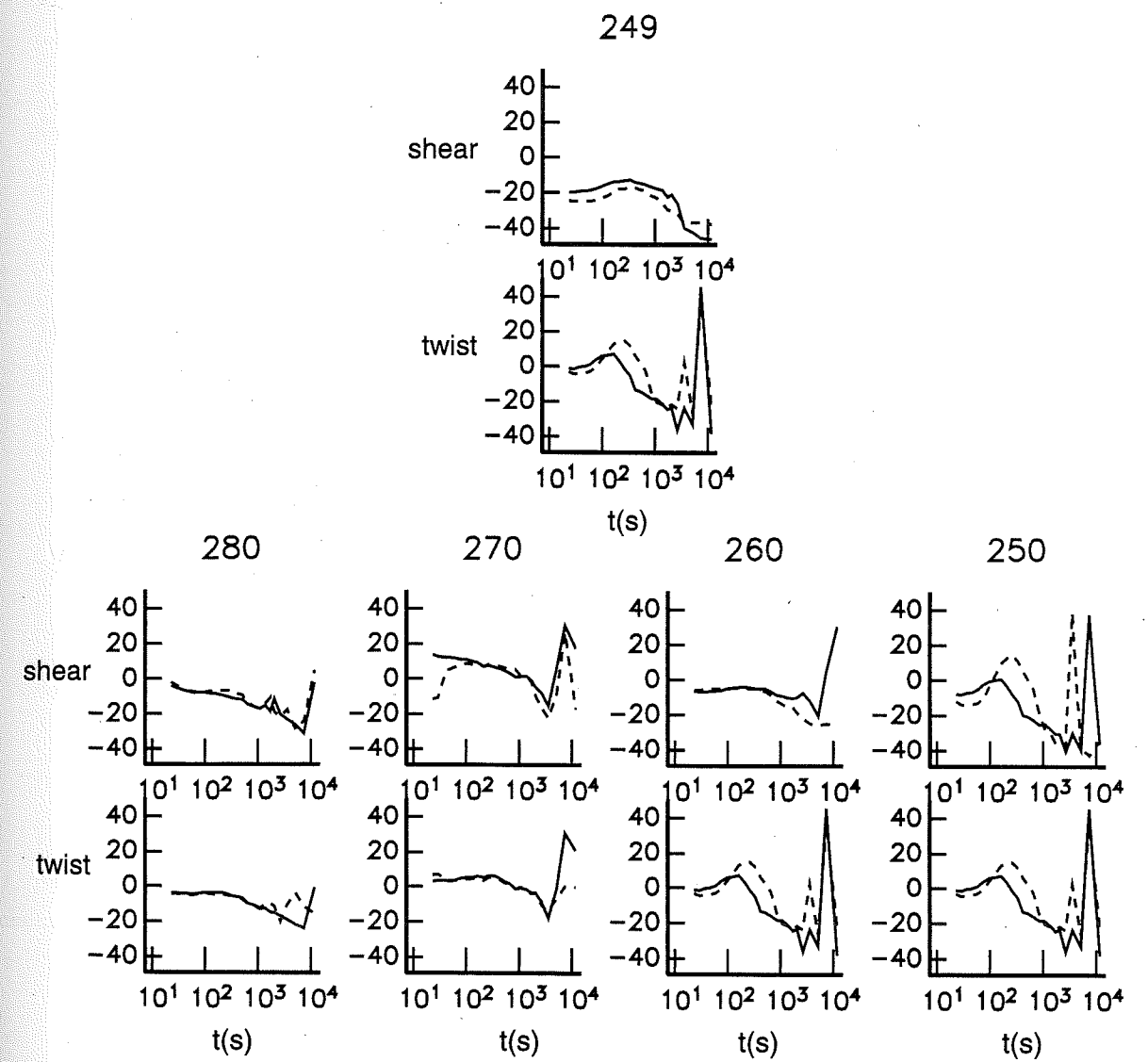
FIGURE IV.6a
Distortion parameters, twist and shear angles for the constrained (solid lines)
and unconstrained (dashed lines) decomposition: western section.
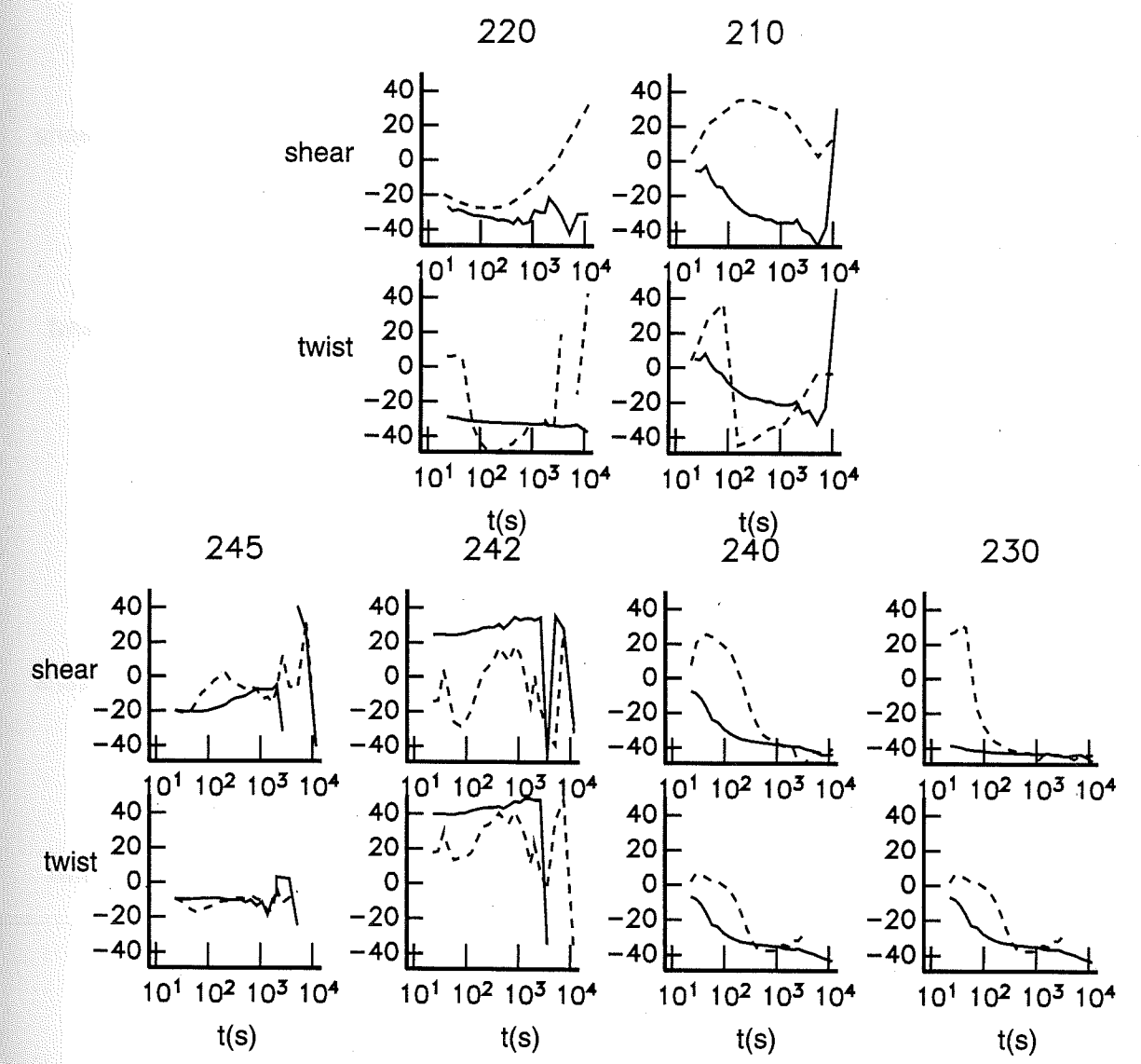
FIGURE IV.6b
Distortion parameters, twist and shear angles for the constrained (solid lines)
and unconstrained (dashed lines) decomposition: Peripheral section.
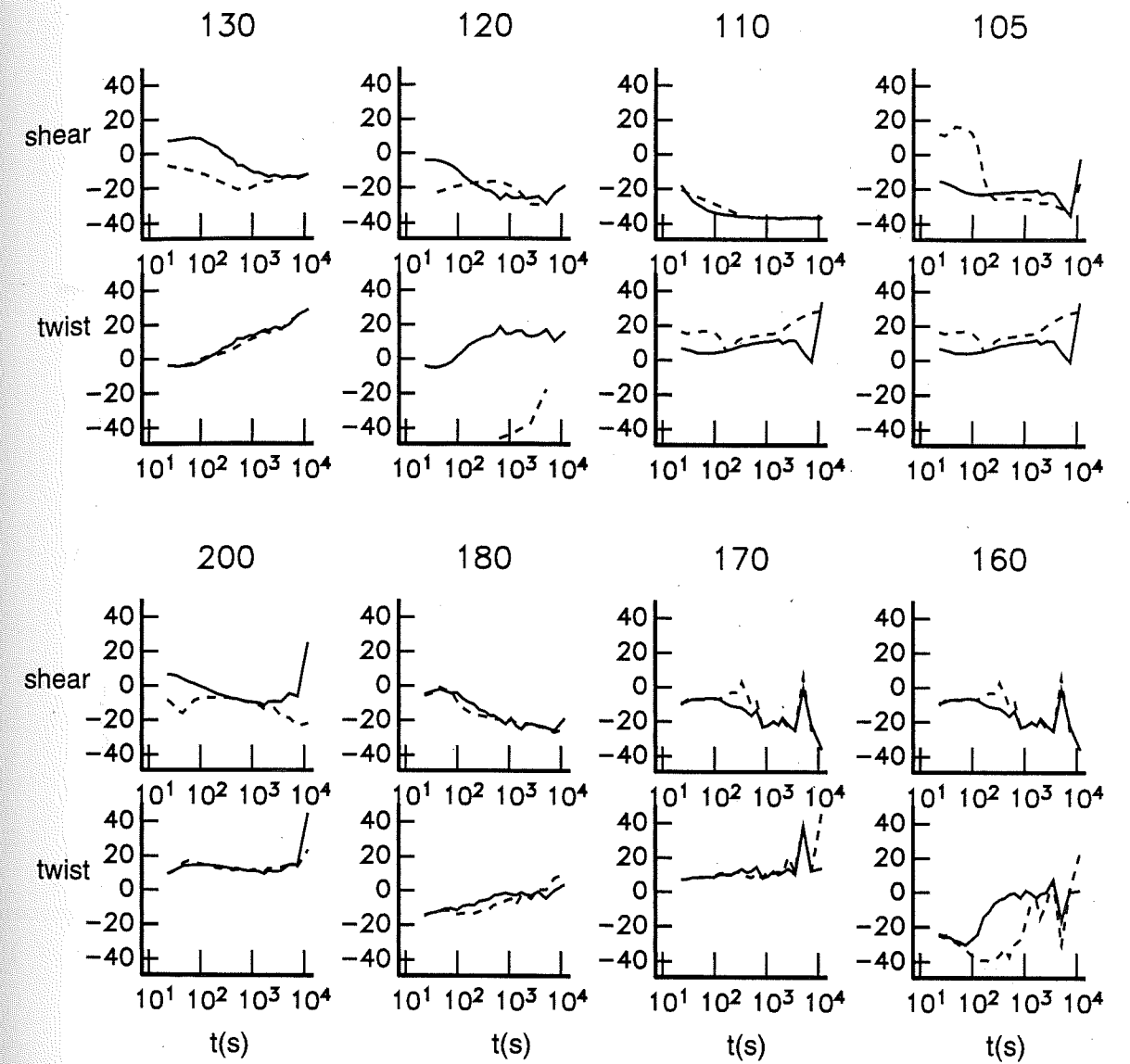
FIGURE IV.6c
Distortion parameters, twist and shear angles for the constrained (solid lines)
and unconstrained (dashed lines) decomposition: eastern section.
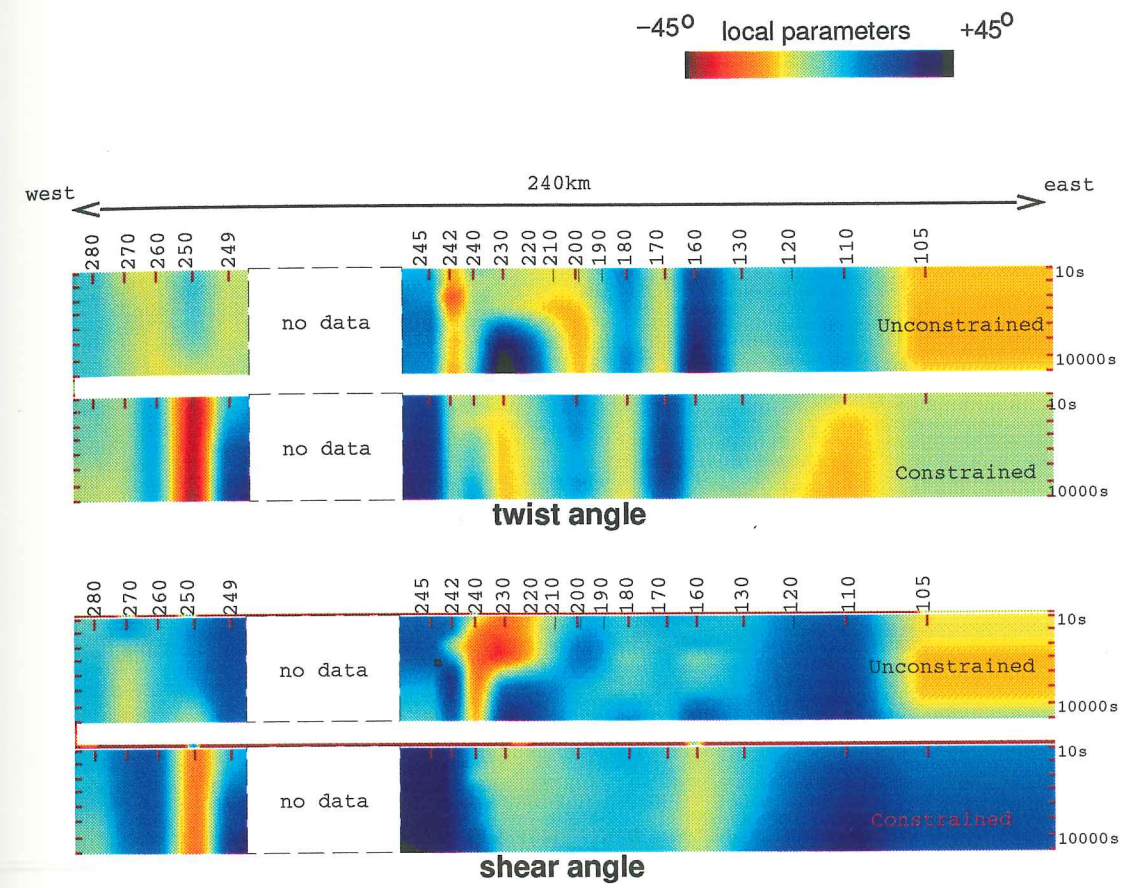
FIGURE IV.7
Local distortion parameters, twist and shear angles, for both the constrained and unconstrained decomposition. The local parameters from the constrained decomposition show weaker dependence with frequency.
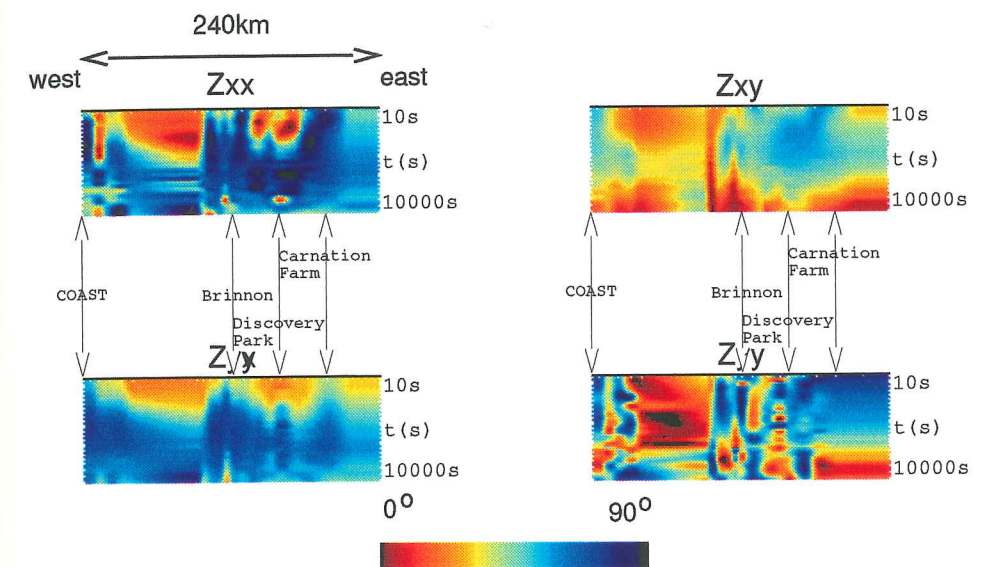
FIGURE IV.8
Phases for Zxx and Zyx and for Zxy and Zyy. For a 2D regional structure with 3D local galvanic effects, {Zxx and Zyx} and {Zxy and Zyy} should have phases approximately equal (each pair). See details on text.
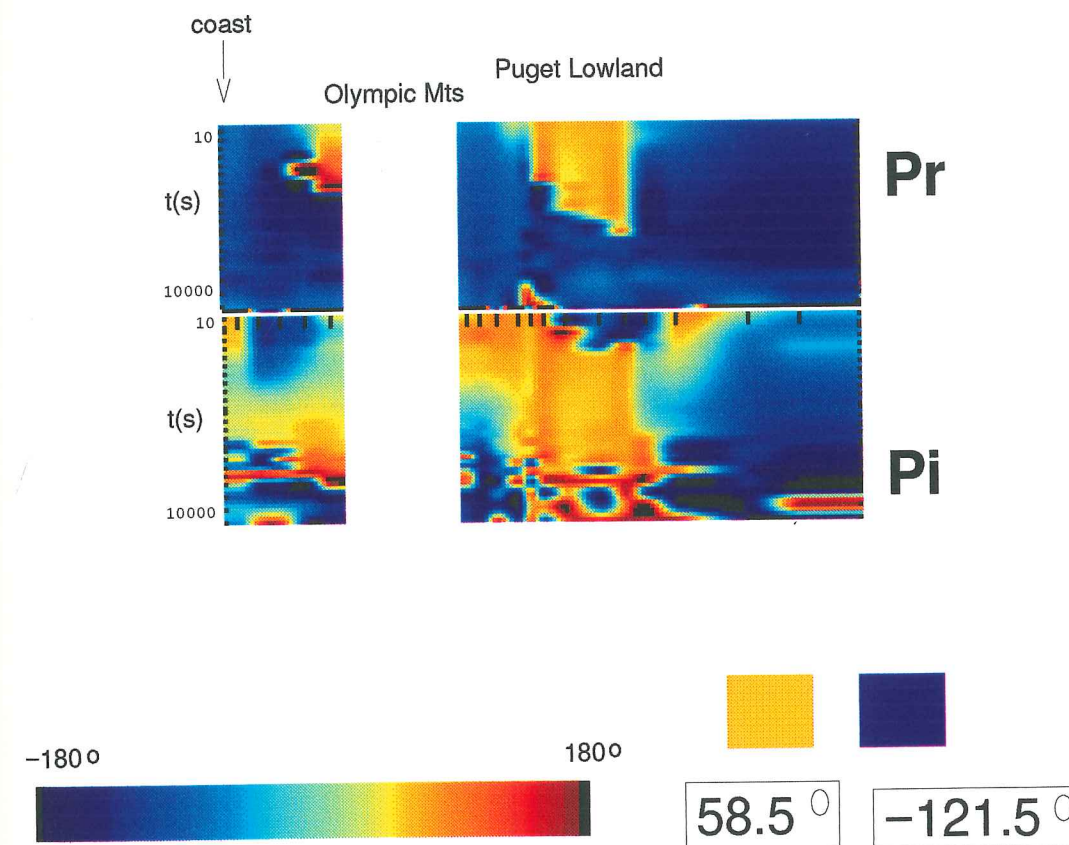
FIGURE IV.9a

Parkinson vector angles measured from the magnetic north (positive clockwise). If the hypothesis of a 2D regional structure with a strike at 31.2 west of the magnetic north is valid, then theoretically Parkinson vectors should be aligned perpendicularly to that direction (58.8 or −121.5). Yellows and blues (representing both angles respectively) are the dominant colors for the real part. See details in text.
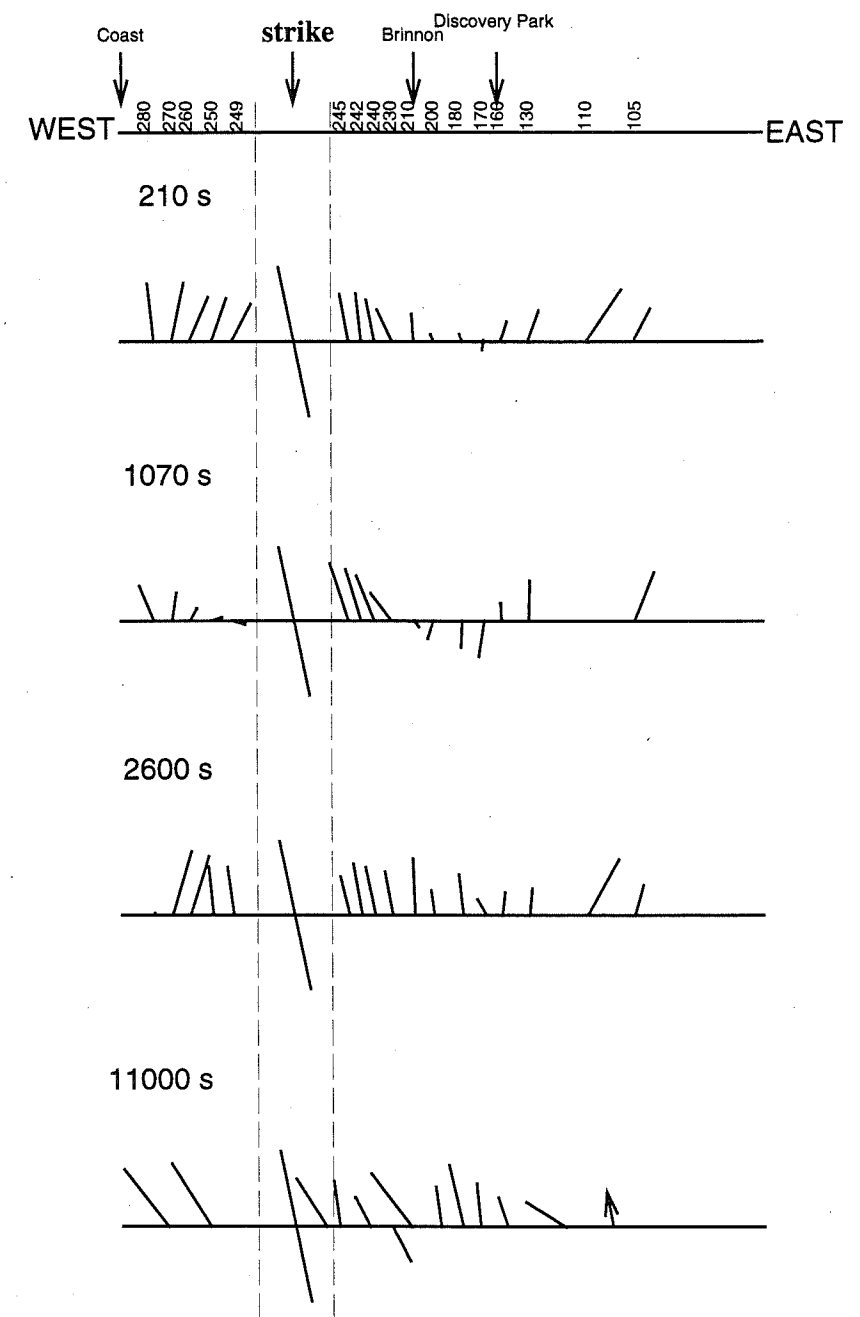
FIGURE IV.9b

Real and Imaginary parts of Parkinson vectors rotated 90 so they will be parallel to an eventaul strike. Dashed lines show direction of the resulting strike (12° west of geopgraphic north) to compare with the data vectors. Note that the both the direction and angles are subjected to errors which are not shown. Four periods are shown.
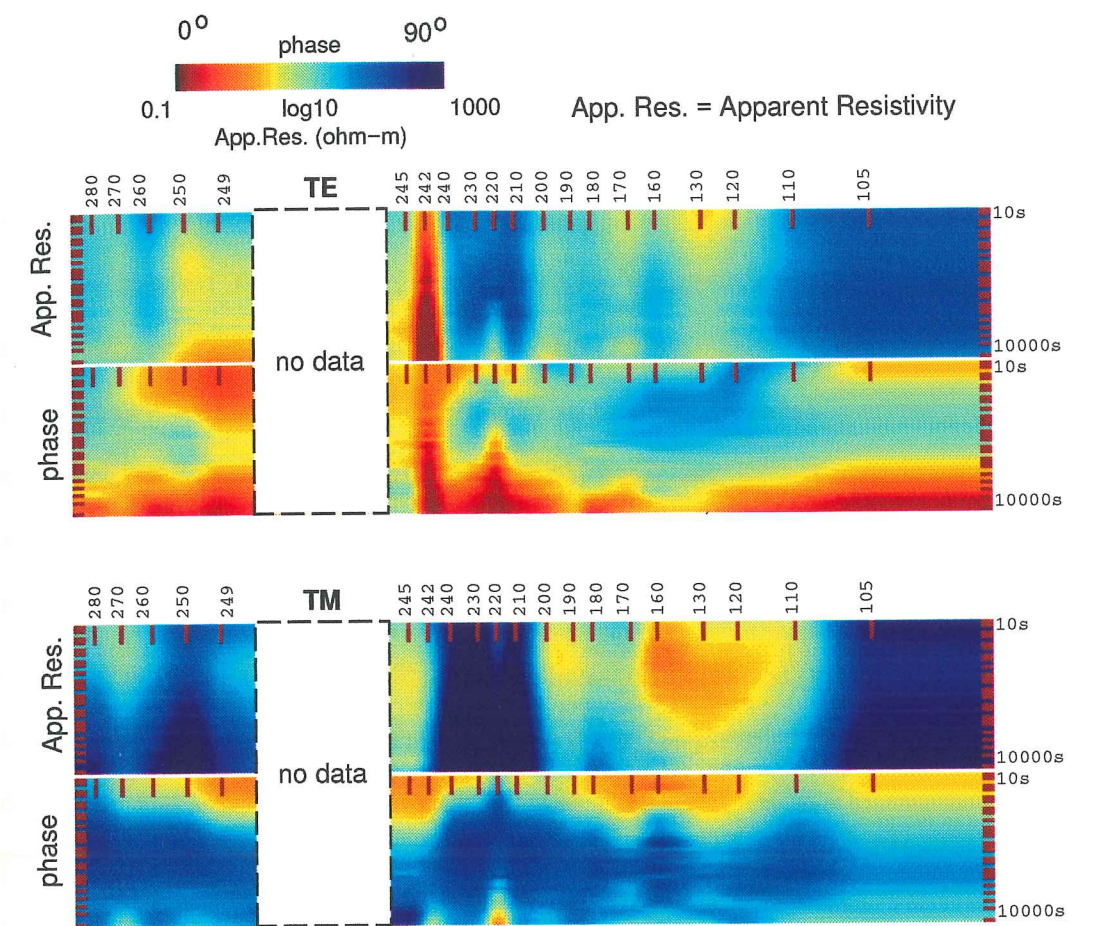
FIGURE IV.10
Pseudosections for the measured TE and TM data in the principal coordinate system.

CHAPTER V

MODELING AND INVERSION OF THE POM DATA

1. INTRODUCTION

To convert the apparent resistivity and phase that were estimated in the last chapter to a model of resistivity beneath the Olympic Mountains and Puget lowland, it is necessary to use forward modeling or inversion. Forward modeling is a trial-and-error process in which a resistivity model is proposed; its MT responses are computed and compared with the measured data; then model is systematically improved until it agrees with the observed data.

Inversion is an automatic process that computes the sensitivity of the data to changes in the resistivity model and uses these sensitivities to change the model in a direction that improves the misfit of the calculated to the measured data. Both processes are non-unique, because there is more than one model than can reproduce the same data. Inversion is preferred because constraints to make the answer unique are more easily implemented and quantified. This chapter describes forward modeling and inversion of the POM data. I also briefly describe improvements that I have made to these techniques.

2. METHODS

2.1. Forward Modeling

The key to a good inversion code is an accurate forward calculation. In prior work, Aprea and Booker (unpublished) investigated three finite difference approximations (FDA) of the partial differential equation to be solved: an FDA for continuous models that fails to give the correct responses when steep gradients are involved; an FDA, which is accurate for discrete models with regions of constant conductivity separated by infinite gradients passing through nodes; and finally, a semi-discrete FDA that handles both situations. The semi-discrete FDA involves 8 abutting triangles around each node and uses an appropriate average of conducting over the triangles for the TE mode and four appropriate averages of resistivity (corresponding to what the node sees to the left, right, up and down) for the TM mode. This FDA easily permits construction of sloping interfaces and gives results for discrete boundaries placed between the nodes that are comparable to the discrete FDA.

2.2. The Rapid Relaxation Inversion Method

In recent years a number of inversion techniques have been proposed for MT data over a 2-D earth (e.g. Oldenburg, 1978; deGroot-Hedlin, 1990). We have chosen to use the Rapid Relaxation Inversion (RRI) of Smith and Booker (1991) because of its superior speed and flexibility and because it was fairly easy to modify to serve out intentions. The principles of RRI are summarized in an appendix, but can be summarized as follows: If you know the 2D electric (or magnetic field) inside a 2D model, then, to first order for small perturbations, changes in the data at an MT site depend

only on changes in the conductivty beneath the site. Thus one can improve a 2D model under a site by solving a 1D inverse problem. If the 2D fields that you know under the site are actually only an approximation to the exact fields, you can improve them by interpolating the conductivity improvements under each site to from a better 2D model and doing a 2D forward problem to calculate the improved fields. This obviously leads to an iterative way to solve the fully 2D inverse problem without the numerically time and memory-consuming need to calculate fully 2D Frechet derivatives. This process is called Rapid Relaxation Inversion (RRI). It is rapid because only 1D inversions separated by 2D forward calculations need to be calculated. It is a relaxation procedure because the information about horizontal gradients in the structure, which enters indirectly though the 2D fields are held fixed at each step. RRI has been well-tested on synthetic examples including candidate structures for the POM area and is orders of magnitude faster than a more conventional 2D inversion.

Given a discrete set of uncertain data, there are infinitely many possible solutions to the inversion. RRI solves the problem of non-uniqueness by finding the solution that is extreme in some sense. Specifically it minimizes a linear combination of a structure penalty function and the sum of the squares of the data misfits weighted by the claimed data errors. The structure penalty is related to a scaled finite difference Laplacian and treats horizontal and vertical gradients differently (see Appendix A and *Smith and Booker, 1991*).

2.3. Modifications to RRI

Two important modifications were made to the original version of RRI in preparation for interpretation of the POM data: incorporation of the ability to freeze the value of the model at certain nodes and to have surface topography. Freezing nodes was key to adding the ocean off-shore and to testing whether certain features in the model were essential. The highly conductive ocean water has a major effect on data near the coast (see Appendix A) and cannot be ignored. We have no data off the coast, but the bathymetry and conductivity of the sea water is well-known and is therefore best incorporated as a constraint. We initially believed that topography would important in the Olympic Mountains. This turned out not be needed, because the effect of the mountains reduced to an additional static shift (see Appendix A). Further details of the modified version of RRI are presented in Appendix A.

2.4. Static-Shifts

Static-shifts are constants multiplying the magnitude of the impedance (i.e. the apparent resistivity). They have the effect of vertically shifting curves of $\log(\rho)$ versus period. The origin of these constants is the presence of charges that accumulate where electric current flows along gradients in the conductivity. This is most easily understood in the special case of a current flowing perpendicular to a boundary between two conductivities. The normal component of electric current $\mathbf{j}$ must be continuous across the boundary. Ohm's Law states that $\mathbf{j}=\sigma\mathbf{E}$ in an isotropic medium and thus the continuity of the normal component of j at a discontinuity in σ implies a discontinuity in the normal component of $\mathbf{E}$. Such discontinuity in $\mathbf{E}$ requires a surface electric charge on the boundary. This charge is called "Galvanic". It is really a DC effect and thus

persists to infinite period and has no effect on the phase of the electric or magnetic fields or on the phase of the MT impedance. It does, however, affect the magnitude of the impedance. Its spatial variation is governed by the Poisson equation and thus depends on the geometry of the charges rather than on the diffusion equation that governs the behavior of the inductive part of the MT response.

The Galvanic response due to the Galvanic charges is a fundamental part of the TM mode response, since it is in this mode that the electric current flows perpendicular to strike. The spatial wavelength of the inductive part of the TM mode is related to the skin depth, but the spatial wavelength of the galvanic part is related to near-surface geometry. It is quite common to have sites sufficiently close to adequately sample the spatial scale of the inductive TM response, but spatially alias the Galvanic part. To the extent that the Galvanic response is adequately sampled spatially, it contains information about the structure that can be recovered by modeling or inversion. However, because the Galvanic response is frequency-independent, spatially aliasing appears as a multiplicative constant in the magnitude of the data, put does not affect the phase. It is thus a static shift. This shift must somehow be removed before one can do a reliable interpretation of the data. Unfortunately, due to very small scale, near-surface irregularities it is almost impossible to escape some static shift unless the electric dipoles are actually placed end-to-end.

Since the TE mode involves currents that are everywhere parallel to boundaries, it is theoretically unaffected by Galvanic charges and hence static shift. However, real Earth structure always involves some variation along strike, especially in the near-surface. Thus there will always be a Galvanic contribution to supposedly TE data. If you only have one profile across strike, then you have no information about the

spatially variation of the Galvanic contamination of the TE mode and the entire Galvanic response of off-profile structure becomes a static shift. Thus static shifts in real TE data are often more important and certainly more difficult to deal with than Galvanic effects (including static shift) in TM data. This discussion is, in fact, the physical basis for the observation by *Wannamaker, et al. (1984)*, that TM data is more reliably interpreted in a 3D environment than TE data when the TM polarization is aligned with the transect. You may recall that this was used to justify the experimental design of the POM profile discussed in Chapter IV and further justifies primarily emphasis on interpretation of the TM data.

Although RRI can simultaneously estimate static shifts as additional model parameters, this is a tricky problem in practice. The way I approached the problem is as follows:

* I inspected the apparent resistivity and phase curves. When the phases were very similar for a group of stations, but the log apparent resistivity curves were offset by a constant, I conclude that significant static-shift was present. See Figure V.1 for an example at the coastal stations.

* I then did trial inversions that started from half-spaces with and without static-shifts, to see which of the sites were more difficult to fit with respect to the apparent resistivity.

* When such an inversion fit the phase well, but differed from the apparent resistivities by a constant, I this constant as the static shifts a further trial.

The goal at every stage was to find a static shift that allowed the inversion to converge easily to the phase (and thus the shape of the resistivity curve), with minimal structure.

3. INVERSION AND MODELING OF THE DATA

3.1. Initial Inversion and Forward Modeling

My first inversion of the TM data started from a 100 ohm-m half-space. This resistivity is within the expected range of resistivity in the POM area. The inversion reduced the object function very slowly and converged to a model that had very little structure and poor data fit. Such behavior suggests that the inversion is caught in a local minimum of the object function and such behavior is not uncommon in a non-linear inversion if the starting model is too far from the model that truly minimizes the object function.

To be reasonably sure that I was starting in a valley of the object function likely to include the minimum structure model that I was seeking, I decided to use an alternative strategy. Based on the surface geology, and reasonable assumptions about the structure, I constructed a model which fit the data much better than any of my initial attempts at inversion. With careful experimentation, I adjusted this model (including the static shifts as described above), until I was satisfied that I had a model that fit most of the important details in the response curves. The exercise involved a limited number of blocks of constant conductivity and used the discrete FDA. Although my goal was to primarily fit the TM data, I also examined the TE data and included structure that improved fit to the TE data, but did not violate the TM data. Figure V.2 shows the calculated responses, the observed data and the model used to start additional inversions.

3.2. Inversion

Forward modeling gives us one model that fits the data and can be quite useful in exploring the range of structure necessary to fit the data. However it does not directly address the uniqueness of the model. Furthermore, as a result of its method of construction, the model of Figure V.2 is likely to contain structure that is permitted by the data, but is also likely to be more complicated than is actually required by the data. To see if a simpler model would also fit the data, this model was used to start a series of RRI inversions. Figure V.3 shows a "tree" of inversions that totaled more than 20 different trials with different parameters and constraints (such as local freezing of nodes, exclusion of of selected data, etc.). I will discuss only the most "successful" branch, which is actually the least constrained. This branch involves four inversions, $I1 \rightarrow I2 \rightarrow I3 \rightarrow I4$. The arrows imply that the starting model for the next inversion is one of the iterations of the previous inversion. Each inversion involves many iterations. These inversions are characterized by:

* Error floor: 5% in resistivity, which corresponds to 1.5° in phase. Setting of a floor is done to encourage the inversion to fit data across the full bandwidth rather than concentrate on the data with very small statistical uncertainty.

* Desired misfit : one standard deviation of the errors modified by the error floor.

* Maximum amount of new model to use in each iteration: 0.7. RRI use dynamic control of both the amount of model to use and the attempted reduction in misfit at each iteration to ensure that the object function continuously decreases.

* Minimum resolution length : 4000 meters. The structure penalty increases logarithmically with depth. This minimum length prevents this penalty from becoming singular at the earth-air interface.

* Vertical to horizontal structure penalty: 4. This reflects the fact that we generally expect vertical variations in structure to be faster than horizontal. It does not prevent high horizontal gradients if absolutely required, but is a prejudice against them.

* Constraint: the ocean water remains unchanged.

Figures V.4a shows selected steps of the model evolution. Figure V.4b shows the r.m.s misfit as a function of iteration number for the entire process. The final valued of 2.1 means that the r.m.s. misfit to the data is 2.1 times that expected for the stated errors given by the time series analysis (modified by the error floor). Although this value is above the goal, we note that it always wise in a minimum structure inversion to under fit the data rather than overfit them. That way you can be even more confident that your model does not contain structure resulting from fitting the noise in the data.

The initial misfit in inversion I1 is somewhat higher than actually achieved by the forward modeling exercise, because the the forward modeling used the discrete FDA, while RRI uses the semi-discrete FDA, which is less accurate for a truly discrete model, but quickly becomes accurate as the inversion smooth out the infinite gradients of the starting model. The initial rapid rise in the misfit during the first few iterations is due to the fact that the starting model is much too rough in the opinion of the structure penalty. Thus the inversion initially reduces the object function by destroying structure in the starting model at the expense of the fit to the data. It is only after several iterations, in which the structure (particularly in the area of the boundary between the Olympic Core and the Peripheral rocks) is heavily smoothed, that the Lagrange multiplier that controls the relative importance of the misfit to the structure

penalty, becomes large enough for the inversion to begin to reduce the misfit. In fact, after many iterations the inversion eventually restores much of the high gradient at the Olympic core boundary wiped out in the initial steps. For this reason, I am convinced that the these high gradients are only weakly controlled by their existence in the starting model.

Figure V.4c shows pseudo sections of the data and calculated responses. You can see that not only are the data well-fit in a global sense, but the details of data structure are also well-fit. If one looks at the details of the misfit at each site, one finds that the inversion systematically underfits the phase at maxima and minima and at strong inflections. This is precisely what one expects for a minimum structure inversion. It chooses to preferentially misfit the data that would result in rough structure in the model.

Although the misfit achieved by the inversion is considerably better than the forward modeling exercise, the final model in the inversion, while generally being similar to the final forward model, is considerably simpler in many respects. One major difference between the starting and final models is the complete disappearance of the mantle conductor near the coast. This was included in the starting model because such a conductor was seen on the EMSLAB Lincoln line *(Wannamaker, et al., 1984)*. Its response is almost entirely in the TE mode and is thus not required by the TM data and is correctly eliminated by the inversion.

Another major difference is the presence in the final model of a generally quite resistive region below the shallow Puget lowland conductor that was not suspected while constructing the starting model. This is the most problematic element of the inversion and its significance is not yet established. Its top is between the two

conductive toes that extend down at either end of the Puget lowland shallow conductor. This is likely a real feature although it seems counter-intuitive that a resistor at depth can be sensed through highly conductive overburden that absorbs most of the vertically propagating energy. One must keep in mind, however, that there are resistive windows on either side of this shallow conductor and energy gets below the conductor from the sides. Furthermore, the resistive region blocks the horizontal flow of TM current at depth and consequently has a Galvanic response, which satisfies the Poisson equation and is not subject to skin depth limitations. However two possible contributors to the deep resistive body are an overshoot (similar to the Gibbs phenomenon in Fourier analysis) associated with a sharp lower boundary to the high conductive shallow structure and an incorrect average static shift over the entire Puget lowland.

3.3. TE mode and Induction Vectors

The TE data were not explicitly fit, due to concern about the 3D effects. Figure V.5a shows the calculated and observed TE responses. The final model from inversion of the TM data does not do a very good job of fitting the TE data. It would clearly be worthwhile trying to quantify the 3D effects in some way so that the TE data could be used. This is because there are structures, such as thin, vertical conductors that have strong TE response, but are essentially invisible to TM. The conductive toes at the edges of the Puget lowland are obvious candidates for improved resolution if the TE data could be reliably incorporated. Nevertheless, it is worthwhile to test a foward calculation for the TE mode with the same final model but with the inclusion of an ocean-mantle conductor. This conductor was included in the starting model because it was seen in the EMSLAB Lincoln line results *(Wannamaker et al., 1989)* and by

inspecting TE data. As already noted, it is not required by the TM data. Fig V.5b shows the calculated responses for such a model. There is considerable improvement in the phase at middle periods across the entire pseudosection. This suggests that an effort to further understand the TE the would be very worthwhile. The very long period TE phase, which may be due to an even deeper ''asthenospheric'' mantle conductor is still not fit.

Another aspect of the TE mode is the vertical field response. Figure V.6 shows pseudosections of observed and calculated Parkinson vectors (see the discussion of the Parkinson vector in Chapter III). Since this response depends only on magnetic fields, it is not directly disturbed by the static charges asociated with the Galvanic response and is thus less disturbed by 3D comunications than the TE MT response. One can see that the calculated vertical magnetic field responses do qualitatively reproduce the observed data lending further credence to the model and incentive to the need to find a way to use these data to improve the model.

4. CONCLUSION

The final model is shown in Figure V.7. Before considering the geologic interpretation of this model in the next chapter, I will review it robust features. From west to east they are:

* A surface conductor coincident with the the Core rocks of the Olympic Peninsula, which thickens to the east and is terminated on the east by a sharp, near vertical boundary.

* A surface resistor that correlates with the surface outcrop of the Peripheral rocks. This structure is bounded by high horizontal gradients to both the east and west.

* A surface conductor coincident with deep sedimentary basins in the Puget lowland. This conductor strengthens eastward and is associated with sub-vertical conductive toes on either end that wrap around a more resistive region below the surface conductor.

* A resistive surface unit in the Cascade foothills that overlies a significant, but poorly delineated lower crustal or upper mantle conductor that extends eastward under the the Cascades.

* A conductive path across the entire model that consists of the Core rocks conductor, a subtle, sub-horizontal conductor under the Peripheral rocks resistor, the Puget lowland conductor and its two drooping toes and finally the deep conductor under the Cascades. If this path were broken, it would drastically alter the TM responses along most of the transect because the electric current entering the model from the highly conducting ocean would have to find some other way to complete its circuit to the deep eastern conductor.
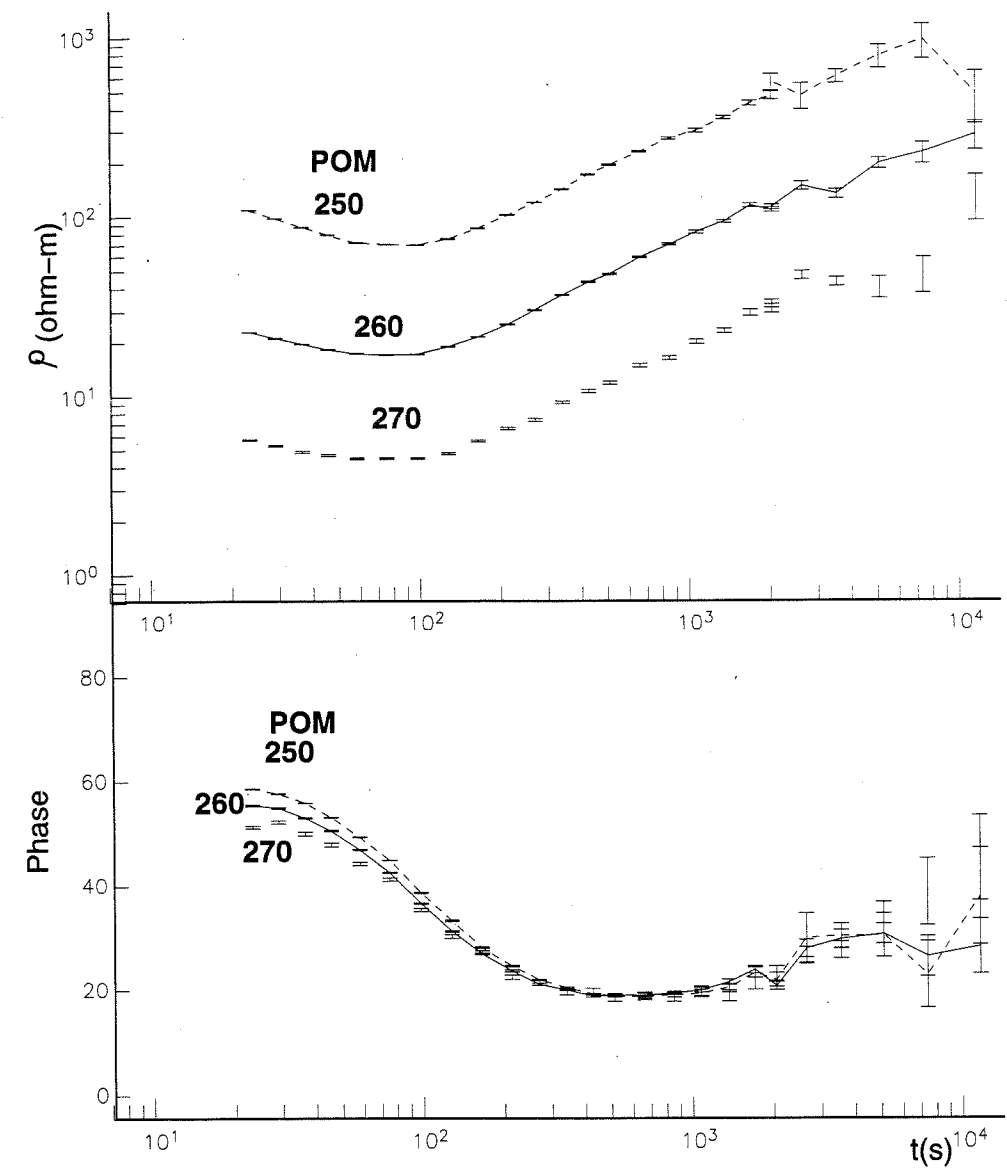
FIGURE V.1
Apparent Resistivity and phase curves for stations POM 270, 260, and 250.
Phases differ at small periods implying differences in the shallow structure,
static shifts affect the apparent resistivity curves. See text.
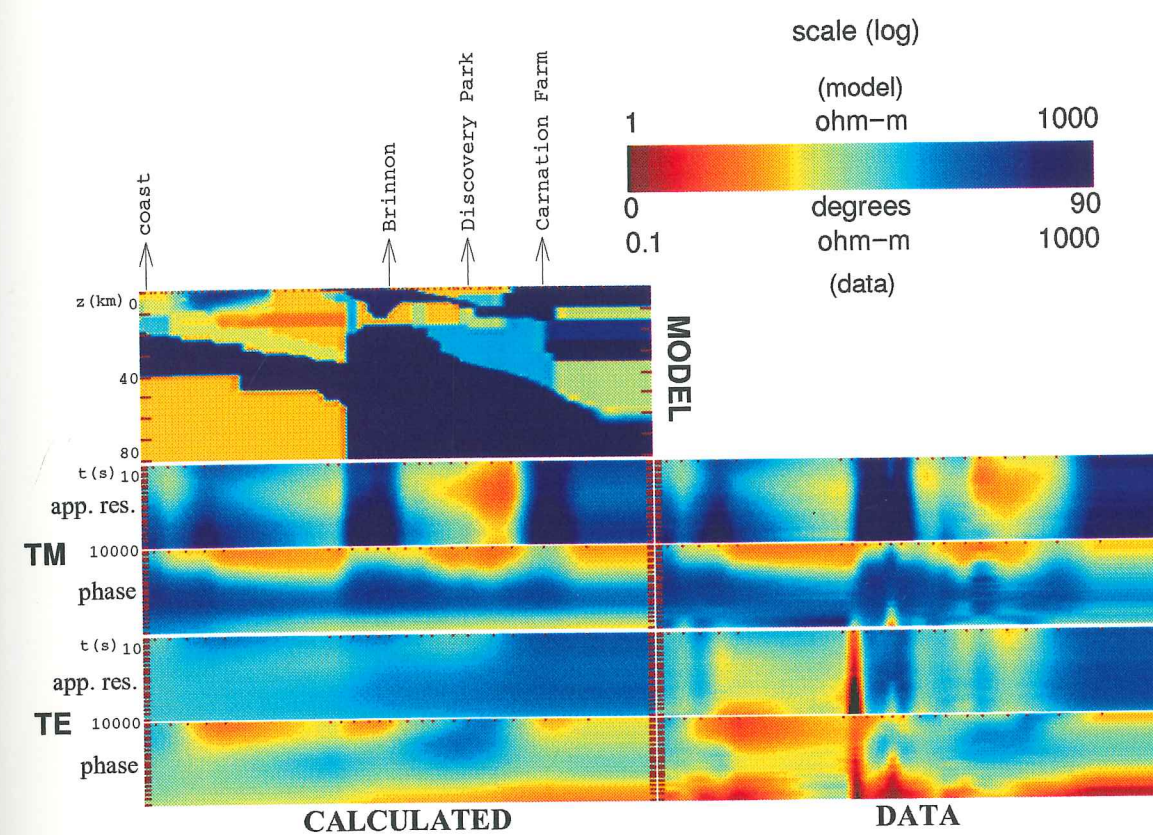
FIGURE V.2
Model constructed from forward modeling trials including previous information. Calculated responses for both modes (TM and TE) are shown with the data (scale 1:1)

model 1

half space   various Forward models
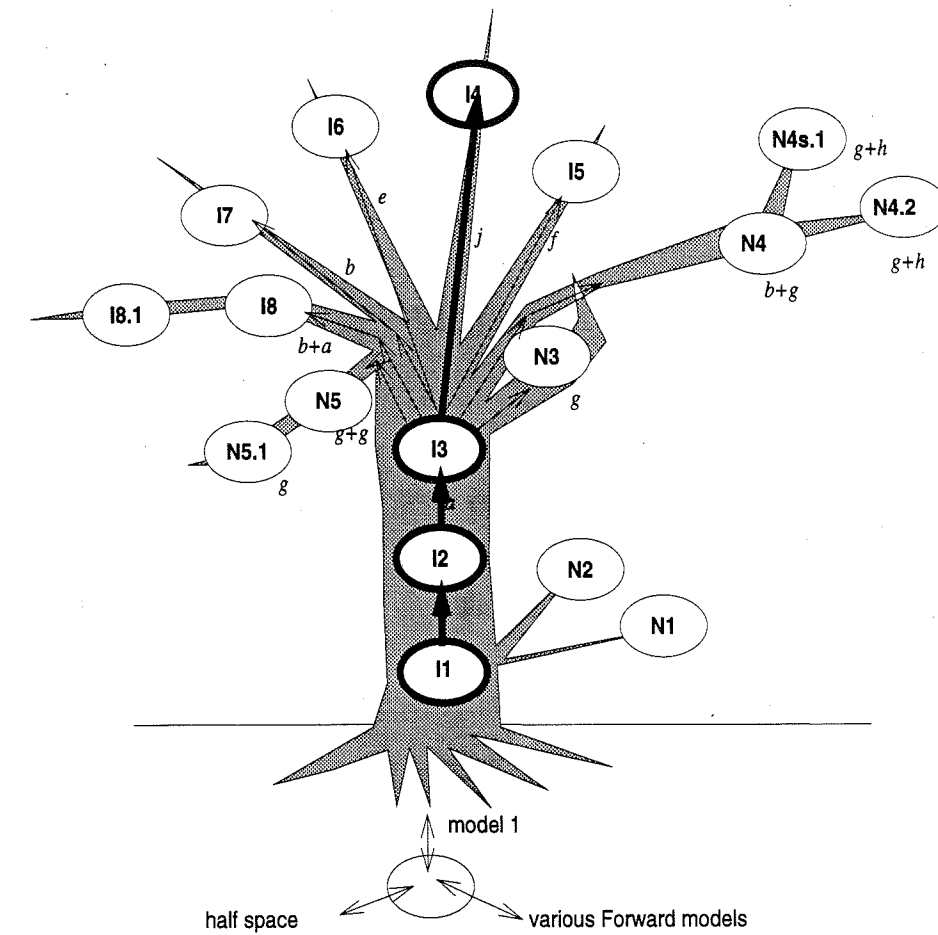
LIST OF THE MOST IMPORTANT DIFFERENCES BETWEEN EACH
 OF THE INVERSIONS:

a* different set of static shifts   f* different level for misfit
b* excluding some data   g*constraints in boundaries
c* upper 1km unchanged   discrete boundaries at some places
d* upper 6km unchanged   h* downweight data
e* different weight for horizontal versus   i* finer grid
 vertical variations   j* offshore structure fixed

FIGURE V.3
Schematic idea about the process of inversion used in this project. The branch
I1--->I2--->I3--->I4 is the only one described in text.

EVOLUTION OF THE MODELS FOR THE INVERSION BRANCH:
I1—>I2—>I3—>I4
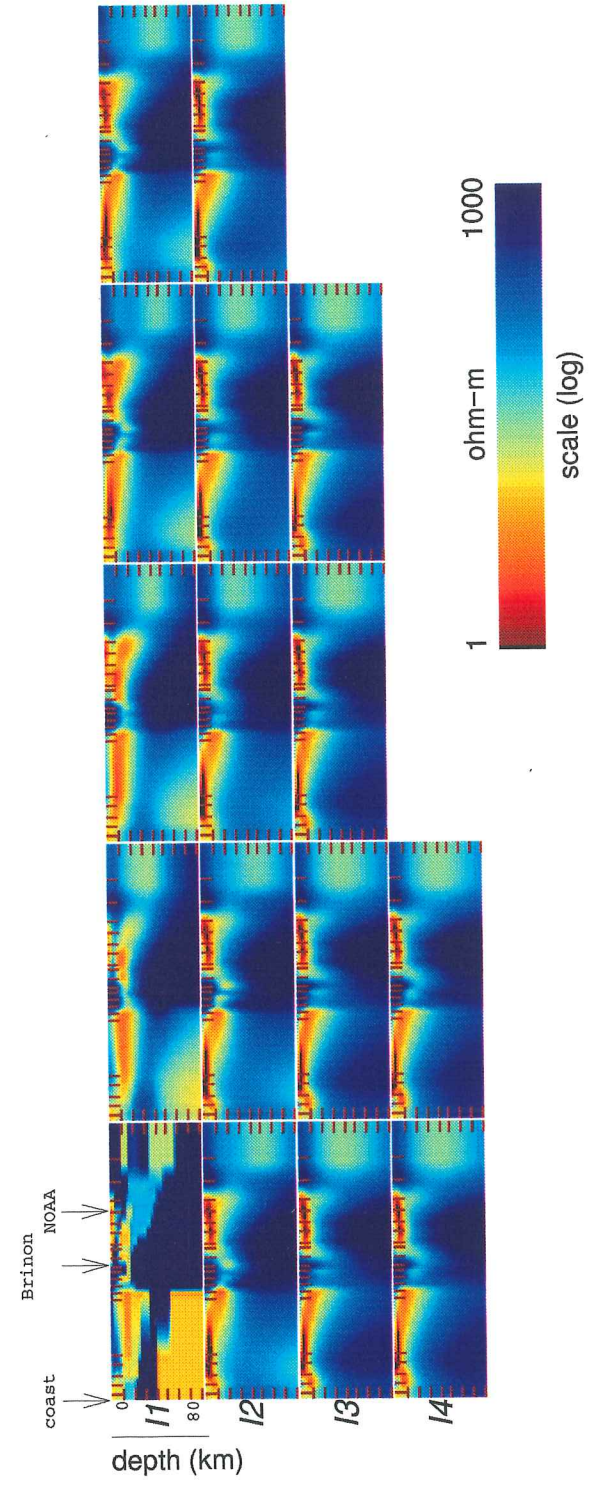
FIGURE V.4a

Model evolution for the inversion branch I1—>I2—>I3—>I4 (from top to bottom, left to right). Selected stages in the evolution are shown. Inversion I4 did not show more than subtle modifications, only two stages are shown. Scale 1:1, ivertical interval 10km. See text for details.

number to station
equivalences:

0	280
1	270
2	260
3	250
4	249
5	245
6	242
7	240
8	230
9	220
10	210
11	200
12	190
13	180
14	160
15	130
16	120
18	110
19	105

$$residual(i,j,k) = (data(i,j,k) - calc(i,j,k))/error(i,j,k)$$
per station/per mode

$$misfit(j,k) = \sum_{i=1}^{nfreq} residual(i,j,k)^2$$

j=1,nmodes (nmodes=2 App. Res., phase)
k=1, nstations

$$misfit = \sum_{k=1}^{ntotal} residual(i,j,k)^2$$

ntotal=nfreq*nstations*nmodes
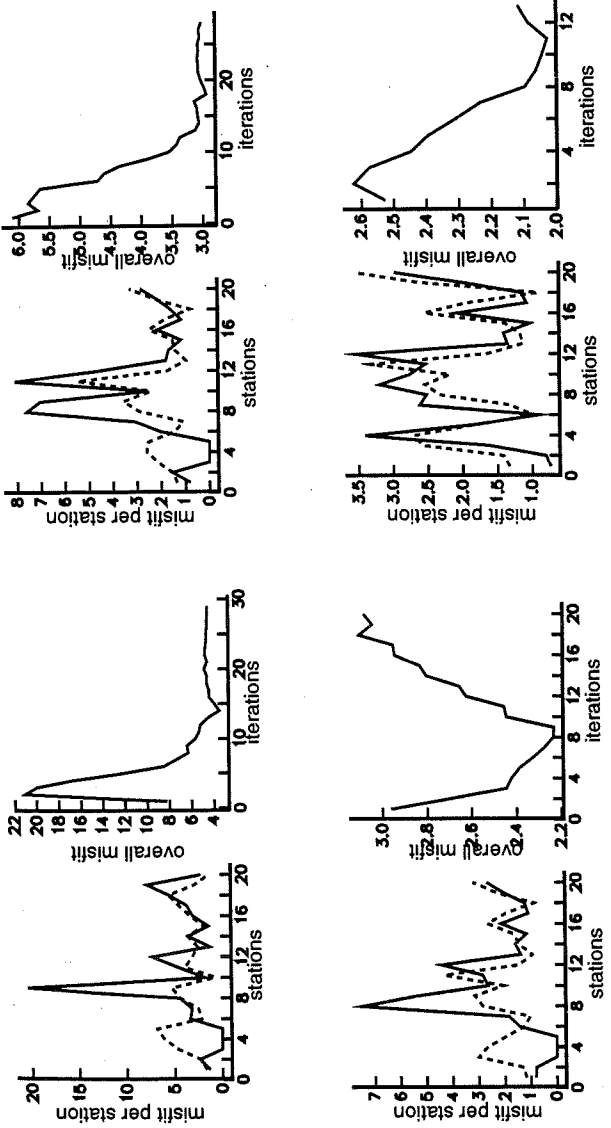
FIGURE V.4b

(a) Apparent resistivity (solid lines) and phase misfit (dashed lines) per station for the best
model of four inversions of branch I1—>I2—>I3—>I4
(b) overall misfit as a function of the number of succeseful iterations

92
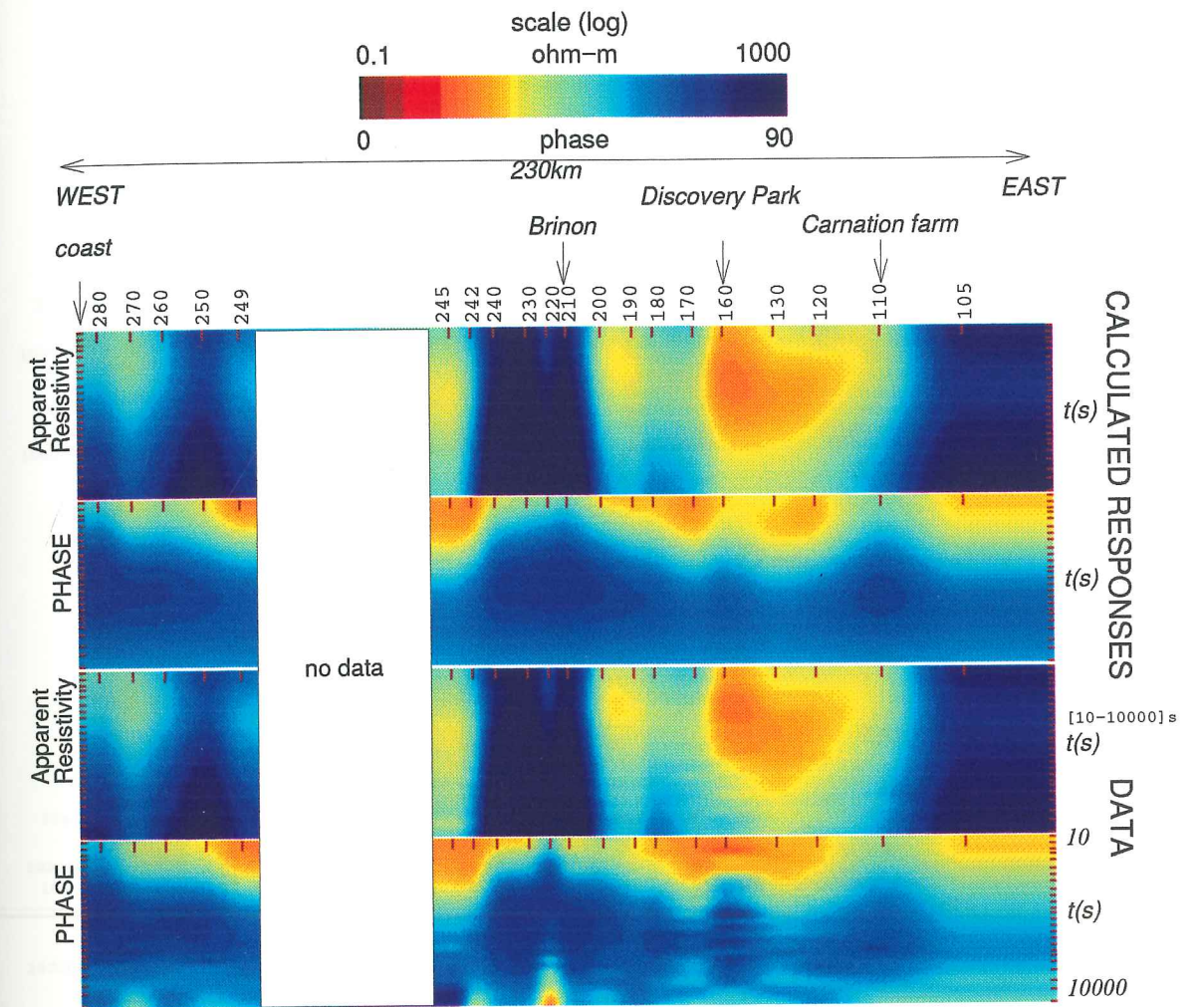
FIGURE V.4c
Calculated Responses versus data for TM mode. Tick marks are stations
The top two pseudosections show apparent resistivity and phase for the
calculated responses, the other two pseudosections are for the data.

93
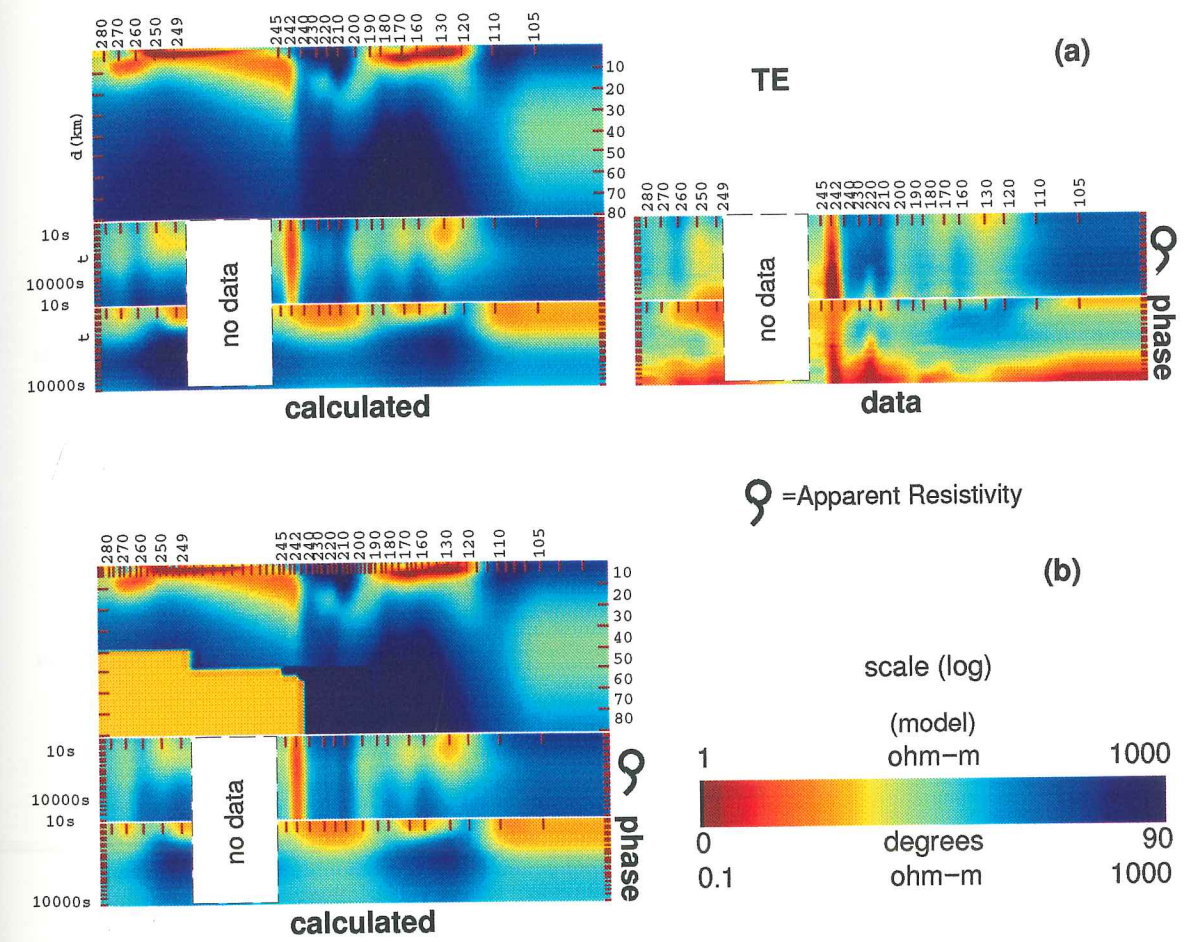
FIGURE V.5
(a) Calculated TE responses and data. See text
(b) Calculated TE responses for the same model but with an ocean−mantle conductor. Note that although the phase is still not fit, the calculated responses are closer than the model shown in (a). See text for further discussion.

PARKINSON VECTORS: modulus
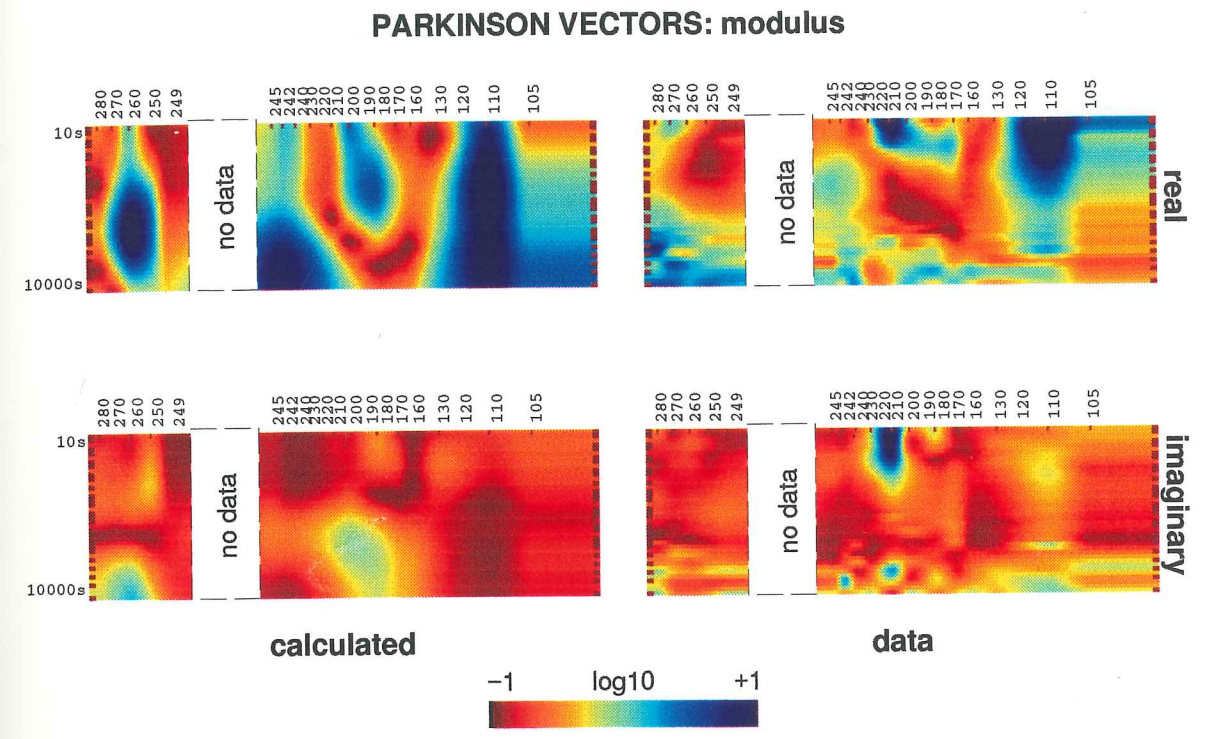
FIGURE V.6

Parkinson vector (defined at each station and for each period) is a complex vector, with modulus and angle. In our 2D model angles for both real and imaginary parts are orthogonal to the strike by definition. To compare data and calculated responses only the modulus for the real and imaginary parts of these vectors are shown. Angles were discussed in Chapter IV.
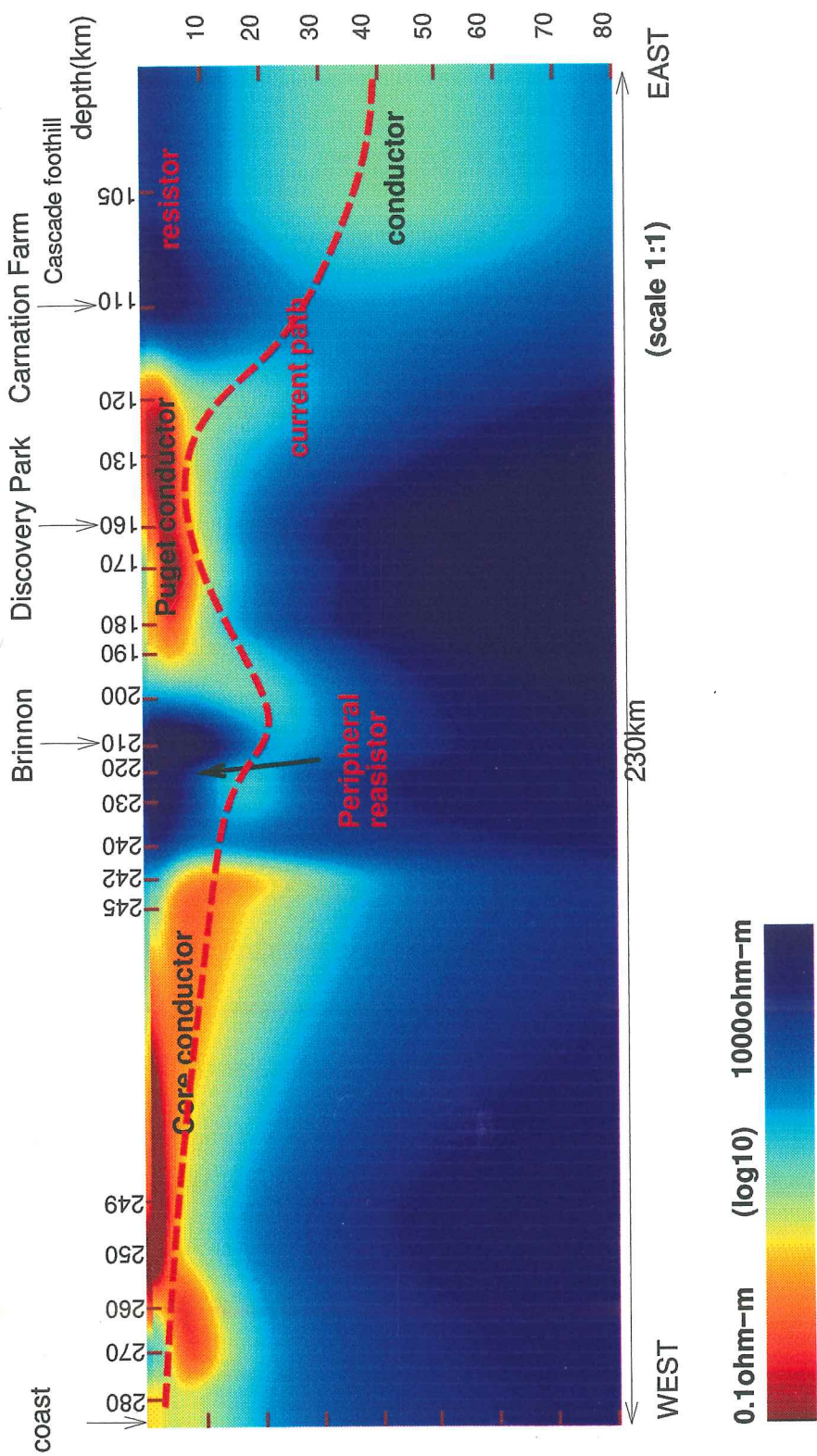
FIGURE V.7

Final resistivity model. The robust features are labeled: Core conductor, Peripheral resistor, Puget conductor, Cascade foothills's resistor and lower–crust–upper–mantle conductor. The dashed line indicates the presence of a current paths (conecting conductors from west to east)

CHAPTER VI

INTERPRETATION OF THE MODEL

1. INTRODUCTION

In the previous chapter a resistivity model for the Olympic Peninsula-Puget low-land profile was derived. This model is shown in Figure VI.1. Features of this model are required by the data and the model is able to replicate most of the details of the TM data and the general features in the induction vectors. In this chapter I will present a geological interpretation of this model and discuss the tectonic implications of my interpretation.

Resistivity data can be interpreted in both a relative and an absolute sense. In the first, the resistivity variations are treated simply as an image of the structure, without actually explaining the cause of the high or low resistivity. In the second, the resistivity data are combined with laboratory measurements of earth materials (e.g. its chemical composition, porosity and temperature) to provide information about the physical state of the material.

2. GEOLOGICAL INTERPRETATION OF THE MODEL

2.1. Correlation with surface geology and regional structure.

Part of the Geologic Map of Washington (*Schuster, 1992*) north of our profile is appended at the appropriate scale above the model in Figure IV.1. We can make the following obvious correlations:

"Core" conductor: The westward-dipping structure very close to the coast correlates with the outcrop of an imbricated slice of Upper Tertiary marine rocks. The triangular-shaped conductor, which thickens to the east, correlates with the surface exposure of the Olympic "Core" rocks, which are series of slices of Lower Tertiary (Eocene-early Oligocene) marine rocks, increasing in age to the east. This resistivity of this structure appears to increase with depth. Although the conductivities generally are high for crustal rocks extending at depths of more than 10 km, we shall see that one can explain them if there are interconnected fluids, probably brines, contained in rocks.

"Peripheral" resistor: The resistive unit east of the "Core" conductor is clearly associated with surface exposures of the Crescent Formation (the major basalt unit of the Peripheral rocks). Its high resistivity is consistent with this unit being basalt. As discussed in Appendix B, resistivity of rocks generally can be explained by the solid electrolyte mechanism of conduction, which with the exception of metal inclusions (such as gold, copper,etc.) gives high values for the resistivity in most the rocks. Basalts fall into this category (over 500 ohm-m), so the high resistivity of this unit is in agreement with that expected from laboratory data. Jointed and fractured basalt with brines in interconnected pore space can have much lower resistivity. This does not seem to apply here. The high horizontal gradient at the western edge of this unit correlates well with the mapped fault contact between the Olympic "Core" rock and Crescent basalts between sites POM242 and POM240 in the Dosewallips valley.

"Puget" conductor: East of the Peripheral resistor is an approximately rectangular

conductor, which deepens slightly to the west, but is more conductive to the east. The thickness of the highly conducting part of this body is approximately 10 km and is therefore consistent with the total depth of sedimentary units reported by others for the Seattle basin (for instance, *Johnson, et al., 1994, Pullen, et al., 1994; Pullen, personal communication, 1996*).

Cascade foothills resistor: East of the conductive Seattle basin there is a surface resistive unit, which thickens to the west and has sub-vertical contact with the Puget conductor. The most obvious resistive correlation is with the Mt. Persis volcanics (*Tabor, et al., 1993*), which outcrop slightly to the north of the profile and may underly thin veneer of Quarternary sediment at the eastern end of our profile. Although of similar general age to the Peripheral rocks, these volcanics are non-marine and may lie over the edge of the pre-Tertiary continent, which would also be expected to be fairly resistive.

The following features do not have surface exposures, but correlate with structures inferred from regional tectonic and geophysical studies.

Resistor beneath the Core conductor: The base of the Olympic Core rocks is characterized by an increase in resistivity. This interface dips eastward. Its precise position is uncertain due to the highly smoothed nature of the minimum structure model, but is quite consistent with the top of the subducting Juan de Fuca Plate. Beneath any surface sediment and the the zone of pillow basalts, oceanic crust and lithosphere are known to be very resistive (*Chave, et al., 1991*).

High Cascades Deep conductor: This feature is diffuse because it is not well-resolved. It is sensed primarily by our easternmost site. Its top may be as shallow as 10 km although it is centered at a depth of about 40 km. It may be much thinner than imaged by the minimum structure model. It may the western edge of a deep Cascade conductor inferred using the magnetovariational (MV) technique by *Gough, et al., (1989)* and attributed by them to a zone of partial melt, which is presumably the root zone for the Cascade volcanos. More recently, *Schultz & Crosson, (1995)* have explained seismic data as requiring a thickened crust under the Cascades and have suggesting magma underplating as the cause. Whether this is an active process is not known. Finally, a recent north-south seismic refraction line that intersects our transect near its eastern end (*Gridley, 1993*) finds a crustal low velocity zone at a depth of about 10 km that may extend as far south as our transect. Its cause is unknown, but may be a tectonic slice of sediments.

2.2. Discussion

Core rocks - Porosities in Core rocks- Buttress

We have suggested that the low resistivities in the Olympic Core are due to fluids in sediments and have mapped their spatial extent. I shall discuss whether the observed conductivities can be produced with geologically reasonable values of porosity and fluid salinity.

Archie's Law is an empirical formula that calculates the conductivity of a porous, fluid-filled rock, given the conductivity of the brine, porosity, and two empirical constants. Archie's Law is discussed in Appendix A. Despite the simplicity of Archie's

Law, it has been successful used for very different rock types.

In order to apply Archie's law, we have to establish first the empirical parameters to use, and secondly to evaluate the range for both porosity and brine resistivity. Porosity and brine resistivity are difficult to determine in a precise way. We know that sediments that enter accretionary complexes may have more than 50% porosity, but due to the deformation and compaction that takes place in the process of accretion, porosity will be reduced to less than 10% (i.e. *Orange, Geddes, Moore, 1993*) . A well offshore of the Olympic Mountains has porosities of 10-20% at about 1 kilometer depth (see *Finn, 1990*). Hyndman & Wang (1993) conclude that 10% porosity is allowed above the slab at the deformation front, and at to 3-4 kilometers 50 kilometers east of the front for Vancouver Island. We can expect that these porosities will increase with depth (probably to less than 1% for depths below 6 kilometers). Thus for a constant brine resistivity and for the same empirical parameters, resistivity should increase with depth.

Figure VI.2 shows conductivity of a host rock versus porosity for different values of brine conductivity. To construct this figure, I used empirical parameters listed in Table B.I in Appendix B (those corresponding to Tertiary rocks and to rocks with less than 4% porosity). The lower limit for brine resistivity is a reasonable assumption base on calculations done by *Hyndman & Wang (1993)* for Vancouver Island. They assume an average salinity of 3.5%, temperatures of the order of 375° and find that the brine resistivity could be as low as 0.02 Ohm-m. Using this lower limit for brine resistivity, Archie's law and the minimum structure resistivity model I obtain the cross-section of the minimum required porosity also shown in Figure VI.2.

Based on the discussion above, there seems little question that the high conductivity at depths above 5 km can easily be explained by pore fluid conductivity. Since the required porosities at greater depth are mostly well below 1%, pore fluid is probably also tenable throughout most of the Core. The area that is clearly problematic is the eastern Core near the boundary with the Peripheral rocks, where we seem to need porosities exceeding 1% at 20 km and of order 3% at 10 km. However, there seems no geological justification for any conduction mechanism other than pore fluids (such as graphite, sulfides or metals). We are therefore forced to conclude that eastern Core rocks must contain an unusually high volume of brine at considerable depth.

The high horizontal gradient separating the Core and Peripheral rocks, implies an interface that initially dips eastward, but which becomes essentially vertical below a depth of about 5 km. This boundary extends down to where we expect the Juan de Fuca Plate. There is no evidence that any significant conductivity is required in the lower crust or at the top of the subducted slab as observed in Oregon (Wannamaker, et al. 1989) east of the vertical boundary of the conductive Core. The only evidence for significant conductivity just east of this boundary is at shallower depth. Furthermore, this mid-crustal conductor is much less conductive than the Core, despite being in a region where the surface is resistive and thus easily penetrated by electromagnetic energy. We can conclude that the conductive Core rocks do not exist east of the western edge of the Peripheral rocks. If there are Core rocks beneath the Peripheral rocks, their physical state is very different. More likely the Core rocks are buttressed against a sub-vertical backstop of unknown, but resistive rocks. The position of this buttress coincides with a steep gradient in the Bouguer gravity anomaly (*Finn, 1990*); and a major break in topography and seems to point to the possibility a vertical fault.

Geometry of the Peripheral rocks

The Peripheral resistor, which we have correlated with the outcrop of the Peripheral rocks is approximately triangular in shape, with its deep end at about 20 km at its eastern end. This thickness is reasonable (*Trehu, et al, 1994*). However, this resistive unit does not extend beneath the Seattle basin. The forwarding modeling exercise included a resistive unit connected to the Peripheral rocks under the Seattle basin as suggested by such authors as *Johnson, et al. (1994)*. This structure was wiped out by the minimum structure inversion and is thus not required. Instead, the inversion introduced a steeply dipping conductive zone that extends to at least 20 km at the west end of the Puget conductor. The west side of this conductive "toe" coincides with the Hood Canal fault. This conductor is an important element in a continuous conducting path for electric current to flow across the model from the ocean (discussed in Chapter V and to be discussed further later). Highly resistive Peripheral rocks extending continuously from the Peripheral resistor under the Puget lowland, would break this path. I cannot exclude the presence of Peripheral rocks under the Puget conductor, but they cannot be must be in a physical state in the conductive toe that makes them substantially more conductive than they are in the Peripheral resistor. Fluids in fractures may be the answer.

Structure of the Seattle basin

As discussed previously, the inferred depths for the rectangular-shaped Puget conductor are consistent with depths for the basin inferred by others. Figure VI.3 compares the north-cross section of *Johnson, et al. (1994)* with a detail of our east-west resistivity model. The regions where the two slices intersect are indicated. Note the

correspondence of the lowest resistivity in my model with the Blakely Formation in the model of Johnson, et al. We can infer that this formation becomes shallower to the east. Note also the higher near surface resistivity in the western half of the basin.

Structural boundaries and faulting in the eastern Olympics and Puget Sound area

Both the Peripheral resistor and the Puget conductor are bounded by very steep gradients. The presence of high resistivity gradients does not imply presence of a fault, but where such gradients coincide with mapped faults at the surface, which separate units of differing resistivity, it is perfectly reasonable to use the behavior of the gradient at depth depth to infer the behavior of the fault at depth. Figure VI.4 shows the resistivity model together with part of a geological map from *Johnson, et al. (1996)*, which shows inferred major faults. We have already discussed the behavior of the fault boundary between the Olympic Core and the Peripheral rocks and concluded that it becomes near vertical and probably extends through the entire crust. The east side of the outcrop of the Peripheral rocks coincides with the Hood Canal fault, which also appears to be sub-vertical in the resistivity model and to separate the Peripheral resistor from a zone of more conductive material that is generally thought to also be Peripheral rocks. The east end of the Puget conductor is almost a mirror image of the west end with a steeply dipping conductive "toe" abutting a resistive region that is deepest at its contact with the toe. *Johnson, et al. (1996)* argue that the eastern edge of the Seattle Basin is bounded by a southward extension of the South Whidbey Island Fault (SWF), a possibly seismically active, but largely un-exposed feature that separates pre-Tertiary from Tertiary basement. The resistivity model lends considerable credence to this. A much more detailed MT survey at the eastern end of our survey

and across the SWF somewhat further north is probably warranted.

Figure VI.5 shows a projection of earthquake hypocenters (Crosson, personal communication) in band 70 km wide about our transect onto the resistivity model. The correspondence between structure in the seismicity and the contours of the resistivity model is very interesting. For instance, there are essentially no seismic events in the Peripheral resistor, which suggests that it may be a mechanically strong element. There are, however, events within the conductive toe at the west end of the Puget conductor, which adds strength to the idea that the difference in electrical conductivity of this zone is not that it not Peripheral rocks, but that that rocks are fractured and contain conductive fluid. There are also appear to be events within the subtle conductor beneath the Peripheral resistor and there is one event on the deep segment of the vertical eastern edge of the Core conductor. Another striking feature is that the seismicity east of the Seattle Basin is confined to the resistive unit above the the deep conductor. The lower limit to the earthquakes faithfully follows a top contour of this conductor. This supports the idea that the conductor is related to a deep thermal feature that controls the depth of the brittle-ductile transition. Beneath the Seattle Basin, the maximum seismicity is clearly within a resistive block between the two toes hanging down from the Puget conductor. Finally, there appears to be a definite change in the Benioff zone seismicity at the intersection of the eastern edge of the Core conductor and the top of the Juan de Fuca Plate. There are many more smaller events east of this point. An exciting possible explanation for this is that the events are on the mega-thrust and that difference in activity is related to having different materials across the thrust or to having different amounts of fluid in the the thrust. In any case, it adds support to the idea that the material that buttresses the core rocks is quite different than the Core.

2.2.1. Comparison with other studies of the Cascadia subduction zone

The interpretations of both the Oregon (*Wannamaker, et al., 1989*) and Vancouver Island (*Kurtz, et al., 1988*) MT lines concluded that a thin dipping conductor near the mega-thrust east of the accretionary wedge is due to sediment being carried down by the slab. *Finn (1990)* also concluded that subduction complex sediments extend under the Coast Range basalts of southwest Washington. In the Olympic Peninsula, however, the accretionary wedge is on land and our results strongly argue against any sediment being carried past a lower crustal block that buttresses the wedge. This implies that the physical state of the mega-thrust beneath the Puget lowland is quite different than along the rest of the subduction zone. This undoubtedly means that the potential for a mega-earthquake is significantly different although I am not in a position to say what this effect will be.

3. CONCLUSION

At the beginning of Chapter IV, I listed a series of unanswered questions about the structure and tectonics of the Puget lowland-Olympic Mountains region and argued that MT had the potential to provide significant insight. Let me summarize progress on each question:

* *How deep and how much further to the east does the subduction complex extend?*

The Olympic Core probably extends to the top of the subducted Juan de Fuca Plate. The core is buttressed almost directly below surface contact between the Core and Peripheral rocks. No sediment is carried down the subduction zone east of this point.

* *Do the Core rocks squeeze beneath the Peripheral rocks?*

No. There is a weak, middle-crustal conductive unit of unknown origin under the Peripheral rocks, which overlies a more resistive lower crust. All of these units are part of the buttress for the Core rocks.

* *How deep and how much further to the east do the Peripheral rocks extend?*

We learned nothing about the actual presence of Peripheral rocks under the Seattle Basin. However, east of the Hood Canal Fault, Peripheral rocks, if they exist, are substantially more conductive than further west, presumably due to fracturing.

* *What kind of material makes up the deeper structure beneath the Puget lowland?*

It is still unknown, but it is highly resistive except in two conductive toes that extend down from both ends of the conductive Seattle Basin. These seem very likely to be associated with two bounding faults, the Hood Canal Fault and a postulated southern extension of the South Whidbey Island Fault. The enhanced conductivity is probably the result of deep circulation of fluids in fractured rock. the

* *What type of structure determines the occurrence of crustal earthquakes typical of this area?*

The resistivity structure is highly correlated with the seismicity, the exact explanations for the correlations remains unclear, because in some cases it is resistive blocks that are quiet and in others it is conductive blocks. However, shallowing of seismicity in the foothills of the Cascades seems likely to be due to a thermally-controlled change in the depth to the brittle-ductile transition. A reduction in the rate of small Benioff zone earthquakes on the portion of the thrust

beneath the Olympic Core as compared to the thrust beneath the buttress is probably due to a difference in the actual material on either side of the thrust or to a change in the amount of fluid present.

* *What are the characteristics of the transition zone between the studied area and the pre-Tertiary continental crust to the east?*

The mirror image for the structure on the east and west ends of the Seattle Basin argues that both ends have similar, probably active, near-vertical faults. On the east, this fault separates the pre-Tertiary basement from the accreted terranes. We have found additional evidence that the deep crust or upper mantle under the pre-Tertiary crust is probably anomalously warm.

I have not exhausted the information that can be obtained from the POM data set and have not even discussed a parallel magnetovariation (MV) array data set that was collected at the same time as the MT data. The MV array should provide considerable information about the 3D nature of the area and thus permit extracting far more insight from the TE MT data. Additionally filling the gap in the Olympic National Park should add considerable confidence to the interpretation of the Core conductor and extending and densifying the MT profile in the eastern Puget lowland and the Cascades, would greatly improve resolution of the deep Cascades conductor.
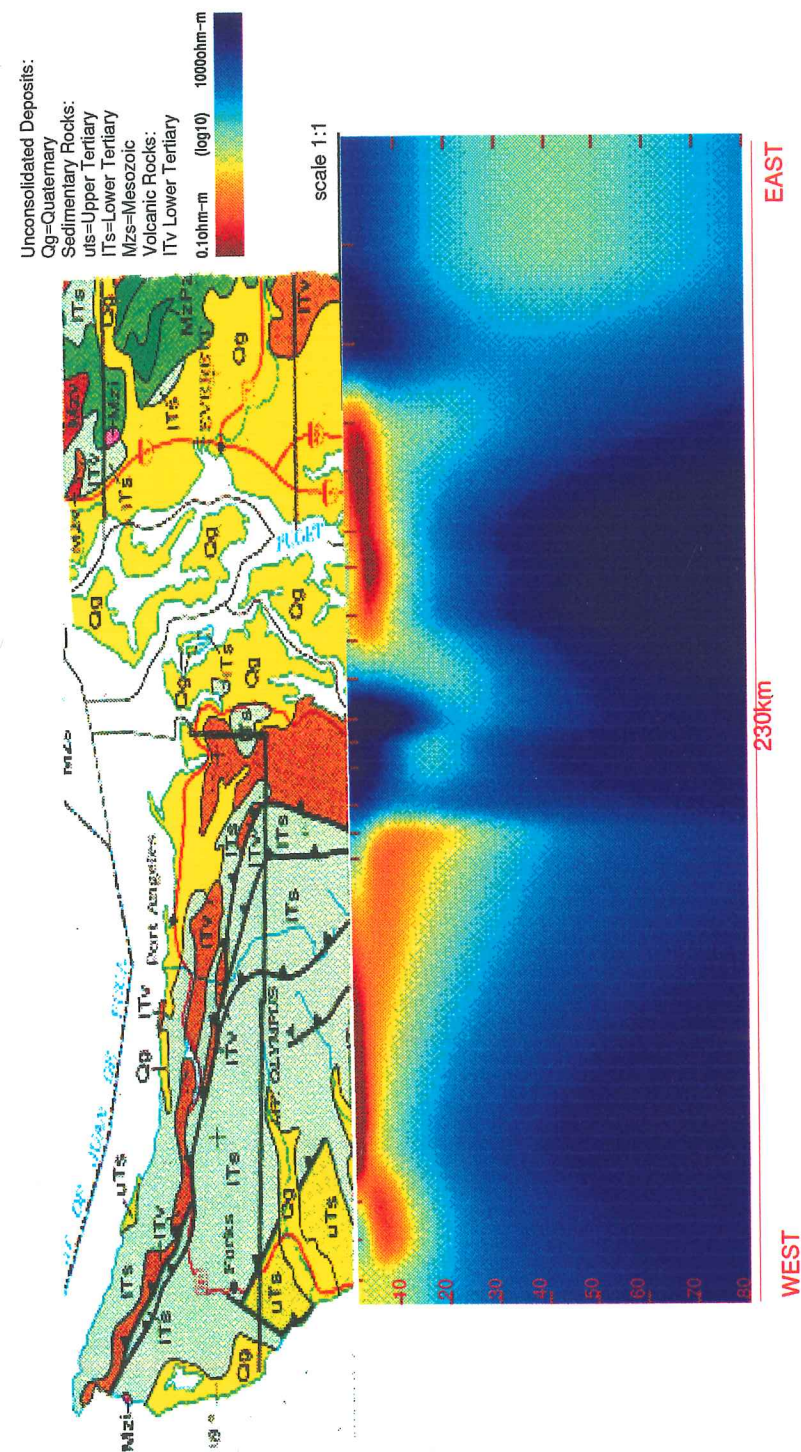
FIGURE VI.1

Resultin resistivity model compare with surface geology (Schuster, 1992).
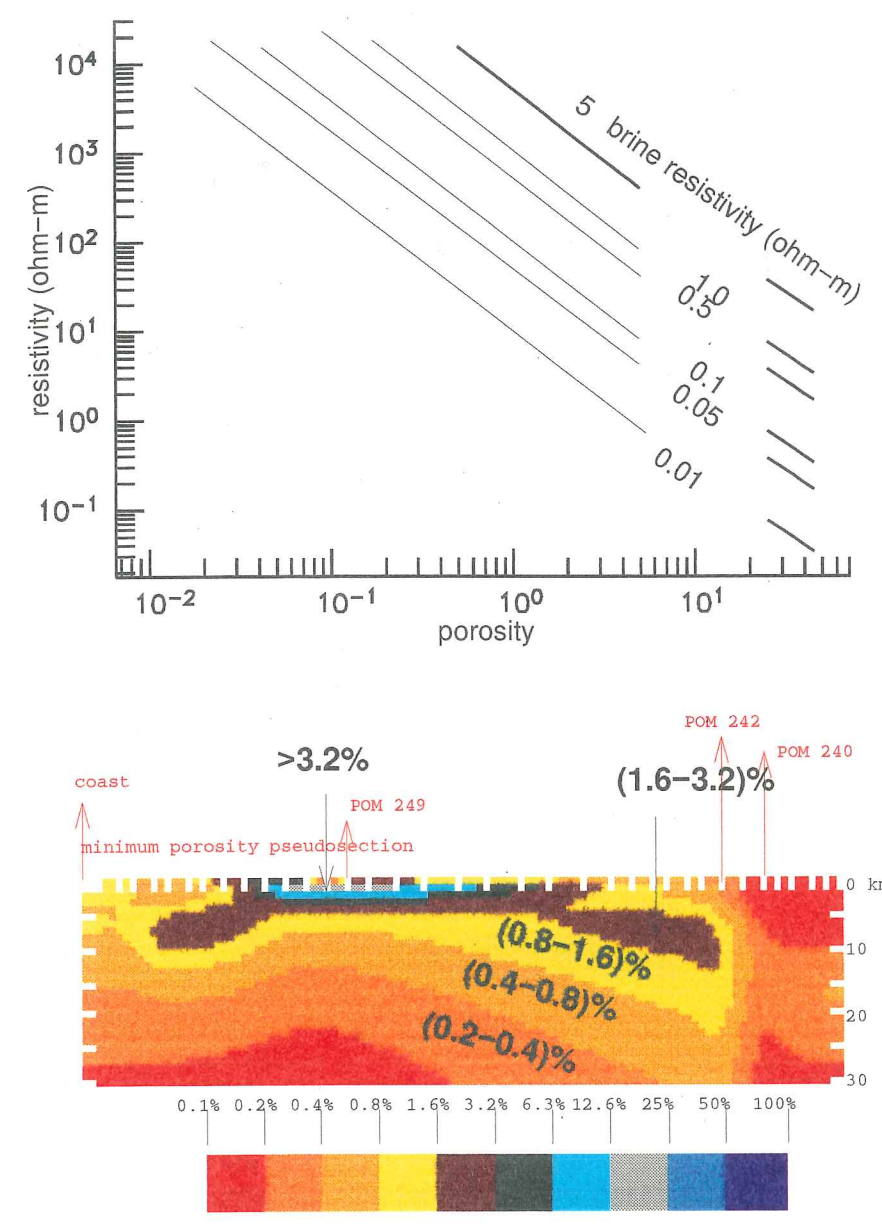
FIGURE VI.2
(a) Lines of constant brine resistivity: resistivity of the host rock for different values of porosity using Archie's Law. See TABLE B.I.
(b) Cross section for the Core conductor showing minimun requiered porosity for brine resistivity of 0.01 ohm−m and Archie's Law parameters for rocks with less than 4% porosity.
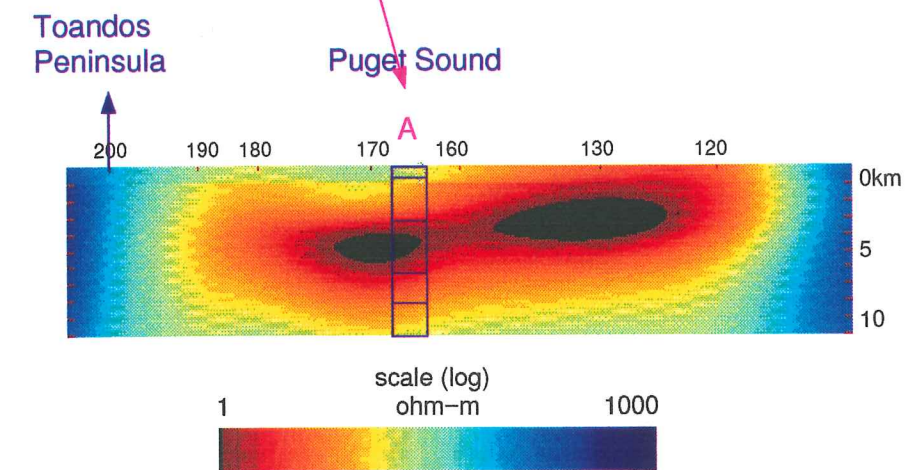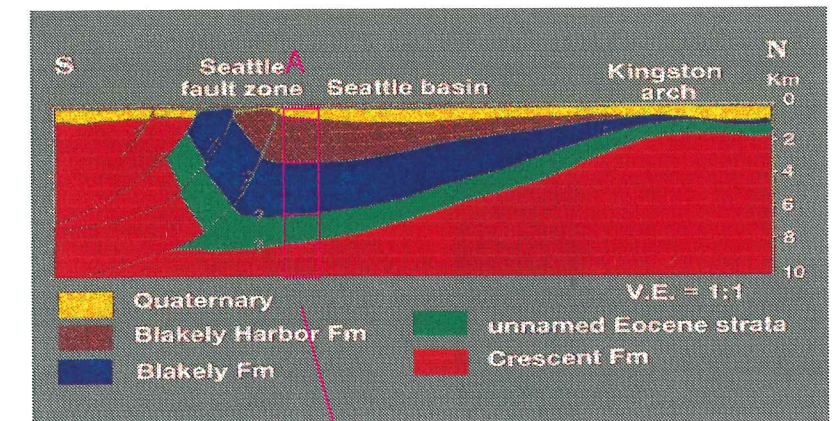
FIGURE VI.3

(a) North–south cross section for the Puget basin showing five different units (from Johnson, et al., 1994). MT transect line intersects at point A.
(b) Resistivity cross-section for the Seattle basin. A marks column corresponding to point A in (a)..
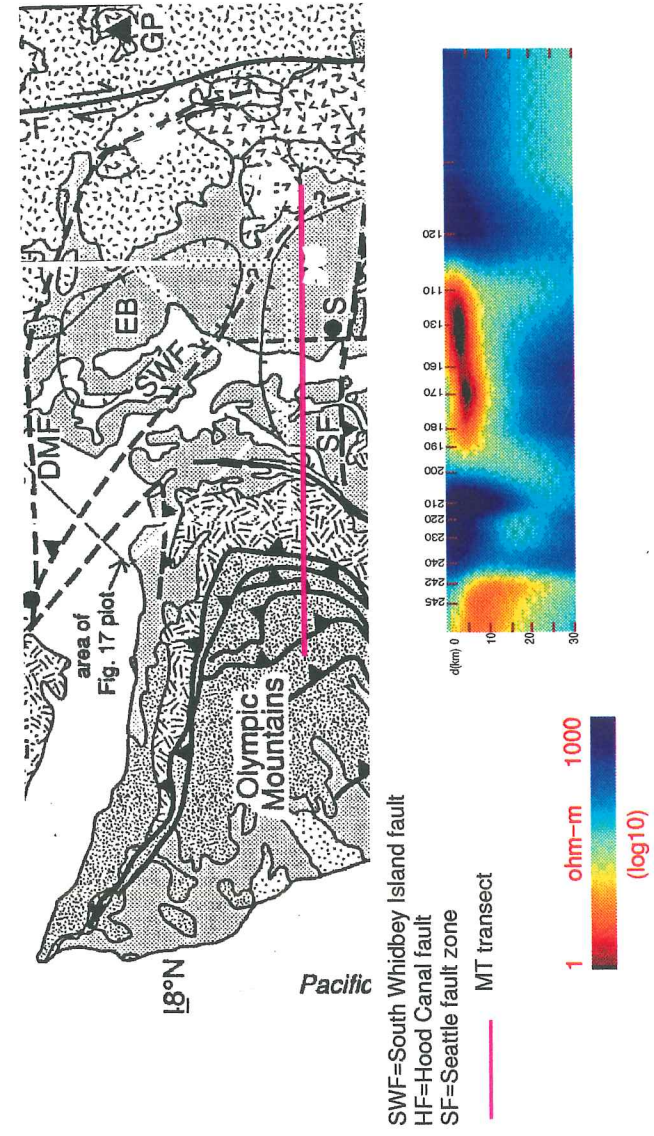
FIGURE VI.4

Location o high resistivity gradientsin the model may be correlated with mapped faults in the area. See text for details (from Johnson, et al., 1996)..
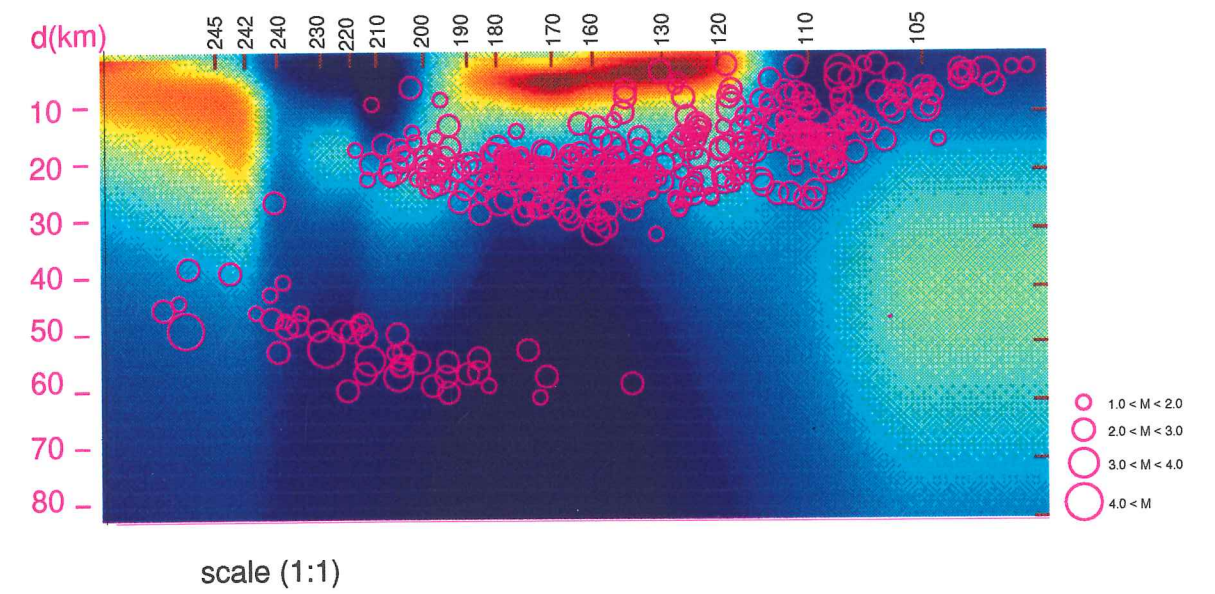
FIGURE VI.5

Detailed cross-section showing all hypocenters of selected earthquakes plotted against the resistivity model to show correlation (earthquakes, from Crosson, 1996, personal. com.).

BIBLIOGRAPHY

Adams, J., Paleoseismicity of the Cascadia subduction zone: Evidence from turbidites off the Oregon-Washington margin, *Tectonics, 9*, 569-583, 1990.

Atwater, B.F., Evidence for great Holocene earthquakes along the outer coast of Washington State, *Science, 236*, 942-944, 1987.

Atwater, B.F. and D.K. Yamaguchi, Sudden, probably coseismic submergence of Holocene trees and grass in coastal Washington State, *Geology, 19*, 706-709, 1991.

Bahr, K., Interpretation of the magnetotelluric impedance ten- sor: regional induction and local distortion, *J. Geophys., 62*, 119-127, 1988.

Batzle, M. and Z. Wang, Seismic properties of pore fluids, *Geophysics, 57*, 1396-1408, 1992.

Blanpied, M.L., D.A. Lockner, and J.D. Byderlee, Fault instability inferred from granite sliding experiments at hydrothermal conditions, *Geophys. Res. Lett., 18*, 609-612, 1991.

Brandon, M.T. and A.R. Calderwood, High pressure metamorphism and uplift of the Olympic subduction complex, *Geology, 18*, 1252-1255, 1990.

Bray, C.J. and D.E. Karig, Porosity of sediments in accretionary prisms and some implications for dewatering processes, *J. Geophys. Res., 90*, 768-778, 1985.

Cagniard, L., Basic theory of the magnetotelluric method of geophysical prospecting, *Geophysics, 18*, 605-635, 1953.

Carson, B., Tectonically induced deformation of deep-sea sediments off Washington and northern Oregon : Mechanical consolidation, *Marine Geology, 24*, 289-307, 1977.

Fyfe, W.S., N.J. Price, and A.B. Thompson, *Fluids in the earth s crust*, p. 388, New York, 1978.

Gridley, J.M., Crustal structure of western Washington State, *Ph.D. Dissertation*, Univ. of Texas, El Paso, Texas, 1993.

Groom, R.W. and R.C. Bailey, Decomposition of Magnetotelluric Impedance Tensors in the presence of local Three-Dimensional Galvanic distortions, *J. Geophys. Res., 94*, 1913-1925, 1989.

Groom, R.W. and R.C. Bailey, Analytical investigations of the effects of near surface three-dimensional galvanic scatterers on MT tensor decompositions, *Geophysics, 56*, 496-518, 1991.

Heaton, T.H., The calm before the quake?, *Nature*, 343, 511-512, 1990.

Heller, P.L., R.W. Tabor, J.R. O'Neil, D.R. Pevear, M. Shafiqullah, and N.S. Winslow, Isotopic provenance of Paleogene sandstones from the accretionary core of the Olympic Mountains, Washington, *Geol. Soc. Am. Bull., 104*, 140-153, 1992.

Heller, P.L., R.W. Tabor, J.R. O'Neil, D.R. Pevea, M. Shafiqullah, and N.S. Winslow, *Geol. Soc. Am. Bull., 104*, 140-153, 1992.

Holdahl, S.R., F. Faucher, and H. Dragert, Contemporary vertical crustal motion in the Pacific northwest, in *Slow Deformation and Transmission of Stress in the Earth, Geophys. Monogr. Ser.. 49*, S.C. Cohen and P. Vanicek (Ed.), Am. Geophys. Un., Washington, D.C., 17-29, 1989.

Hsu, K.J., Exhumation of high pressure metamorphic rocks, *Geology, 19*, 107-110, 1991.

Hyndman, R.D., Dipping seismic reflectorselectrically conductive zones and trapped water in the crust over a subducting plate, *J. Geophys. Res., 93*, 13391-13405, 1988.

Hyndman, R.D., C.J. Yorath, R.M. Clowes, and E.E. Davis, The northern Cascadia subduction zone at Vancouver Island: Seismic structure and tectonic history, *Can. J. Earth.Sci., 27*, 313-329, 1990.

Hyndman, R.D. and K. Wang, Thermal constraints on the zone of major thrust earthquakes failure: the Cascadia Subduction Zone, *J. Geophys. Res., 98*, 2039-2060, 1993.

Hyndman, R.D., K. Wang, T. Yuan, and D. Spence, Tectonic sediment thickeningfluid expulsion and the thermal regime of subduction zone accretionary prisms: The Cascadia Margin off Vancouver Island, *J. Geophys. Res., 98*, 21865-21876, 1993.

Johnson, S.Y., C.J. Potter, and J.M. Armentrout, Origin and evolution of the Seattle fault and Seattle basin, Washington, *Geology, 22*, 71-74, 1994.

Jones, A. and R. Groom, Strike angle determination from the magnetotelluric impedance tensor in the presence of noise and local distortion: rotate at your peril!, *Geophys. J. Int., 113*, 524-534, 1993.

Kurtz, R.D., J.M. DeLaurier, and J.C. Gupta, A magnetotelluric sounding across Vancouver island sees the subducting Juan de Fuca plate, *Nature, 321*, 596-599, 1986.

Larsen, J.C., Removal of local surface conductivity effects from low frequency mantle response curves, *Acta Geodaet. Geophys. Acad. Sci. Hung., 12*, 183-186, 1977.

Law, L.K., D.R. Auld, and J.R. Booker, A geomagnetic variation anomaly coincident with the cascade volcanic belt, J. Geophys. Res., 85, 5297-5302, 1980.

Lisowski, M., Results from 1986 and 1987 GPS surveys across the Strait of Juan de Fuca, Washington and British Columbia, *Seismol. Res. Lett., 60,* 1, 1989.

Muller, J.E., P.D. Snavely Jr., and R.W. Tabor, D. Davis, J. Supple, and F.A. Dahlen, Mechanics of fold and thrust belts and accretionary wedges, *J. Geophys. Res., 88,* 1153-1172, 1983.

Oldenburg, D.W., One dimensional inversion of natural source magnetotelluric observations, *Geophysics, 44,* 1218-1244, 1978.

Orange, L., D.S. Geddes, and J.C. Moore, Structural and fluid evolution of a young accretionary complex: The Hoh rock assemblage of the western Olympic Peninsula, Washington, *Geol. Soc. Am. Bull., 105,* 1053-1075, 1993.

Parker, R.L., The Inverse problem of electromagnetic induction: Existence and construction of solutions based upon incomplete data, *J. Geophys. Res., 85,* 4421-4428, 1980.

Pullen, J., K.C. Kreager, and S.D. Malone, Receiver function array study in the Puget Sound region, Washington, *Eos, 75,* 485, 1994.

Quist, A.S. and W.L. Marshall, Electrical conductances of aqueous sodium chloride solution from 0 to 800 degrees and pressures to 4000 bars, *J. of Phys. Chem.,* 72, 684-703, 1968.

Riddihough, R.P. and R.D. Hyndman, Canada's active western margin: the case for subduction, *Geosci. Can., 3,* 269-278, 1976.

Riddihough, R.P., Recent movements of the an%D de Fuca plate system, *J. Geophys. Res., 89,* 6980-6994, 1984.

Rogers, G.C., An assessment of the megathrust earthquake potential of the Cascadia subduction zone, *Can. J. Earth. Sci., 25,* 844-852, 1988.

Rohr, K.N.M., Increase of seismic velocities in upper oceanic crust hydrothermal circulation in the Juan de Fuca plate, *Geophys. Res. Lett., 21,* 2163-2166, 1994.

Savage, J.C., Geodetic strain measurements in Washington, *J. Geophys. Res., 86,* 4929-4940, 1981.

Savage, J.C., M. Lisowski, W.H. Prescott, and M. Lisowski, Strain measurements and the potential for a great subduc- tion earthquake off the coast of Washington, *Science, 252,* 101-103, 1991.

Scholtz, C.H., *The mechanics of earthquakes and faulting,* p. 439, Cambridge University Press, New York, 1990.

Schultz, A., J. Booker, and J. Larsen, Lake Bottom Magnetotellurics, *J. Geophys. Res., 92,* 10639-10649,, 1987.

Schultz, A.P. and R.S. Crosson, Seismic velocity structure across the Central Washington Cascade Range from refraction interpretation with earthquakes sources, *J. Geophys. Res.,* (in preparation). 1996.

Schuster, J.E., *Geologic Map of Washington,* Washington State Department of Natural Resources, Division of Geology and Earth Resources, Olympia, WA, 1992.

Smith, J.T. and J.R. Booker, Rapid inversion of two-dimensional magnetotelluric data, *J. Geophys. Res., 96,* 3905-3922, 1991.

Stanley, W.D., W.D. Mooney, and G.S. Fuis, Deep crustal structure of the Cascade Range and surrounding regions from seismic refraction and magnetotelluric data, *J. Geophys.Res., 95,* 19419-19438, 1990.

Taber, J. and B.T. Lewis, Crustal structure of the Washington continental margin from refraction data, *Bull. Seismol. Soc. Am., 76*, 1011-1024, 1986.

Tabor, R.W, J.E. Muller, and P.D. Snavely, Late Mesozoic and possible early Tertiary accretion in western Washington State, *Geol. Soc. Am. Bull., 106*, 217-232, 1994.

Tabor, R.W., A Tertiary accreted terrane: Oceanic basalt and sedimentary rocks in the Olympic Mountain Washington, *Geol. Soc. Am. Centennial Field Guide - Cordilleran Section*, 1987.

Tabor, R.W., V.A. Frizzell, D.B. Jr. Booth, R.B. Waitt, J.T. Whetten, Jr., and R.E. Zartman, Geologic map of the Skykomish River 30 by 60-minute quadrangle, *U.S. Geol. Surv, Map I-1963*, 1993.

Tabor, R.W., Late Mesozoic and possible early Tertiary accretion in western Washington State: The Helena-Haystack melange and the Darrington-Devils Mountain fault zone, *Geol. Soc. Am. Bull., 106*, 217-232, 1994.

Tabor, R.W., Late Mesozoic and possible early Tertiary accretion in western Washington State: The Helena-Haystack melange and the Darrington-Devils Mountain f%Alt zone, *Geol. Soc. Am. Bull., 106*, 217-232, 1994.

Thomson, D.J. and A.D. Chave, Jackknifed error estimates for spectra, coherences, and transfer functions, in *Advances in Spectrum and Array Processing*, pp. 58-113, Englewood Cliffs, N,J,, 1991.

Tichelaar, B.W. and L.J. Ruff, Depth of seismic coupling along subduction zones, *J. Geophys. Res.*, in press, 1992.

Tikhonov, A.N., Determination of the electrical characteristics of the deep state of the earth's crust, *Dok. Akad. Nauk USSR, 73*, 295-297, 1950.

Trehu, A.M., J. Asudeh, T.M. Brocher, J.H. Luetgert, W.D. Mooney, J.L. Nabelek, and J. Makamura, Crustal architecture of the Cascadia Forearc, *Science, 266*, 1994.

Tse, S.T. and J.R. Rice, Crustal earthquake instability in relation to the depth variation of frictional slip properties, *J. Geophys. Res., 91*, 9452-9472, 1986.

VanDecar, J.C. and R.S. Crosson, Determination of teleseismic relative phase arrival times using multi-channel cross- correlation and least squares, *Bull. Seismol. Soc. Am., 80*, 150-169, 1990.

Wang, K., Kinematic models of dewatering accretionary prisms, *J. Geophys. Res., 99*, 4429-4438, 1994.

Wannamaker, P.E., W. Hohmann and S. Ward, Magnetotelluric responses of the three-dimensional bodies in layered earths, *Geophysics, 49*, 1517-1533, 1984.

Wannamaker, P.E., J.R. Booker, A.G. Jones, A.D. Chave, J.H. Filloux, H.S. Waff, and L.K. Law, Resistivity cross section through the Juan de Fuca Subduction System and its tectonic implications, *J. Geophys. Res., 94*, 14127-14144, 1989.

Wong, I.G., Deep intraplate earthquakes in the western United States and their relationship to lithospheric temperatures, *Bull. Seismol. Soc. Am., 80*, 589-599, 1990.

Zhdanov, M.S. and G.V. Keller, *The Geolectrical Methods in Geophysical Exploration*, Amsterdam, 1994.

APPENDIX A

INVERSION: 2D

1. INTRODUCTION

In a 2D case the solution of Maxwell equations separates into two independent modes, TE and TM in the principal axis system, reduces to two the non-zero elements of the impedance tensor $\mathbf{Z}$ (Z_{xy} and Z_{yx}). The impedance tensor would be a function of y and z with $\hat{x}$ parallel to the strike direction. The "data" would be either $Z_{xy}(y_s,z)$ or $Z_{yx}(y_s,z)$ where y_s marks the position of a station. Given $\sigma(y,z)$ (conductivity structure), $\mathbf{Z}(y,z,w)$ is perfectly determined at any point. The question is: Would be possible to invert this path ? If $\mathbf{Z}$ is known at every point in the space, would be σ perfecttly determined? The answer of this questions is yes, the solution would be unique. Now, suppose only a set of discrete values for $\mathbf{Z}$ is known, would be possible to obtain the true σ? The answer would no, as the solution is not unique. Nevertheless, from all the possible solutions one may want to work with those with the minimum structure.:

The first step is to determine in what way these functions (Z_{xy} or Z_{yx}) are sensible to small variations in σ. Let us define V and U, functions related to Z_{xy} (TE) and Z_{yx} (TM) respectively:

$$\text{TE:} \quad V = i\,\omega\,\mu_0\,\frac{H_y}{E_x} \tag{A.1}$$

$$\text{TM:} \quad U = \frac{E_y}{H_x} \tag{A.2}$$

The variations $\delta\sigma$ are small enough to cause small variations in δU or δV. Beginning from an unperturbed state, the resulting fields of the new structure $\sigma + \delta\sigma$ would be expressed as perturbations of the original fields. Writing down the Maxwell's equations corresponding to the two independent modes δV and δU can be expressed as functions of $\delta\sigma$ if some second order derivative terms are neglected.

$$\delta V(y_0, z_0) = \frac{i \, \omega \, \mu_0}{E_x^2(y_0, z_0)} \int_{z_0}^{z_*} E_x^2(y_0, z) \, \delta\sigma \, (y_0, z) dz \tag{A.3}$$

$$\delta U(y_0, z_0) = \frac{1}{E_y^2(y_0, z_0)} \int_{z_0}^{z_*} E_y^2(y_0, z) \, \delta\sigma \, (y_0, z) dz \tag{A.4}$$

where z_* is a depth sufficiently large that the electric field has effectively decay to zero, and (y_0, z_0) is the site position.

Both $V(y)$ and $U(y)$ depends on the local change of $\sigma(y,z)$, as a as a function of depth only. In this quasi-1D problem the 2-dimensionality is involved in the fields themselves. The resulting 2D structure is built by interpolation of the values at each of the sites or stations considered as data. The fields involved in equations (A.3) and (A.4) come from the solution of Maxwell's equations for a 2D structure $\sigma(y,z)$.

This perturbation analysis is close to the one used for 1D MT problem *(Oldenburg, 1978)*. These site inversions are called "pseudo-Frechet" derivatives, because the difference with the 1D Frechet derivatives is that the fields involved respond to a 2D model.

1.1. Pseudo-One dimensional inversions: RRI

In this nonlinear inverse problem models which are extreme in some global sense are wanted. In particular, in the RRI used here *(Smith and Booker, 1991)* the following functional is used to impose penalties in the model (rapid horizontal variations):

$$Q(y_i) = \int (z + z_0^3) \left[\frac{\partial^2 m}{\partial z^2} + \frac{\partial^2 m}{\partial y^2} * g(z) \right] dz$$

where $g(z)$ allows for trading-off between penalizing horizontal and vertical structures. This can be translated in finite differences as:

$$Q_i = (\mathbf{R} \, \mathbf{m}_i - \mathbf{c}_i)^T \, (\mathbf{R} \, \mathbf{m}_i - \mathbf{c}_i)$$

where $\mathbf{m}_i$ is the discrete sampled model and $\mathbf{R}$ is a roughening operator, $\mathbf{c}_i$ is a vector that arises from penalizing the horizontal second derivatives. The functional to be minimized is:

$$W_i = Q_i + \beta_i \, e_i^2 \tag{A.5}$$

where e_i are the variances of the measurement errors and β_i a trade-off parameter between model structure and misfit.

Equations (A.3) and (A.4) can be translated into:

$$(\mathbf{d} - \mathbf{e}) - \mathbf{d}_0 = \mathbf{F}\,\mathbf{m} - \mathbf{F}\,\mathbf{m}_0 \qquad (A.6)$$

where $\mathbf{m}$ nd $\mathbf{m}_0$ are the sampled models at discrete points, the difference between them is δm, these are vectors of nz elements. The data are represented by a nfreq vector $\mathbf{d}$ and the calculated responses as $\mathbf{d}_0$. The misfit would be within some tolerance $\mathbf{e}^T\mathbf{e}$ as the data has errors. Finally, $\mathbf{F}$ is and nz x n_f pseudo-Frechet derivative matrix. The basic idea is to find a model that satisfy (A.6) minimizing (A.5).

2. INVERSION NEW FEATURES

Equations (1) and (2) say that if part of the model remains unchanged, then this part does not contribute at all in the corresponding changes on the data. Suppose the following situation, you want to invert data to get a conductivity image of the study area, but you also known some part of the structure. There is not an unique solution, but you would like to move in the space of solutions characterized by models having that part of the structure you know. We can do that by simple asking that part of the model to remain unchanged through the whole inversion procedure. We have two different situations, one situation where stations are involved, and a second situation, only grid-sites are involved.

In the first case, when part of the "known" structure is beneath a station (see Figure A.1a), we simply have to change the integration limits of equations (A.3) and (A.4), instead of ζ_0, let say z_1 where z_1 would be the depth of the "known" part of the model at that particular station:

$$\delta V(y_0,z_0) = \frac{i\,\omega\,\mu_0}{E_x^{2_0}} \int_{z_1}^{z_*} E_x^2(y_0,z)\,\delta\,\sigma\,(y_0,z)dz \qquad (A.3.1)$$

$$\delta U(y_0,z_0) = \frac{1}{E_y^2(y_0,z_0)} \int_{z_1}^{z_*} E_y^2(y_0,z)\,\delta\sigma\,(y_0,z)dz \qquad (A.4.1)$$

In the second situation, when part of the "known" does not involve stations (see Figure A.1b), then a wise interpolation is the only thing required for solving the problem: the interpolation performed at each iteration step in order to construct a 2D model should not touch the "known" part. In this interpolation we can also make choices on the conductivity gradients at these boundaries (between the fixed part of the model and the part that comes from inversion).

Now, suppose a different situation, you have stations located not at the air-interface surface as usual, but rather on to another surface (see Figure A.1c) (i.e. bottom of the ocean). That is not a problem as equations (A.3) and (A.4) simply will be evaluated at the new position instead of from z_0. But no information about the above structure will be given, so σ for $z > z_1$ (instead of z_0) should be known:

$$\delta V(y_0, z_0) = \frac{i \, \omega \, \mu_0}{E_x^{2_0}} \int_{z_1}^{z_*} E_x^2(y_0, z) \, \delta\sigma \, (y_0, z) dz \qquad (A.3.2)$$

$$\delta U(y_0, z_0) = \frac{1}{E_y^2(y_0, z_0)} \int_{z_1}^{z_*} E_y^2(y_0, z) \, \delta\sigma \, (y_0, z) dz \qquad (A.4.2)$$

Finally, another situation can also be addressed: the presence of topography relieve (see Figure A.1d). Its implementation does not involved changes in δV or δU, but rather a different approach on how the matrices involved in a 2D problem are treated and/or stored. With no topography, the model is represented by a nz*ny-dimension matrix, where ny is the number of horizontal nodes, and nz vertical nodes, the same for all sites. When topography is present we should increase the nz-dimension of the matrix by [nair(max)+nz], where nair(max) is the maximum of the set {nair(1), nair(2),...,nair(ny)} which represents the air-nodes at each site (topography). This is basically a Forward Modeling problem. Nevertheless, when calculating either δU or δV, care must be taken in working with the correct values of all the terms involved in the integrals (z_0 will be a $z(i)$ with "i" different for each station; the same when evaluating the fields and the function themselves).

I modified the inversion code, so the following options are available (see Figure A.2):

(1) data at any other surface rather than the air-earth interface

(2) constraining parts of the model

(3) topography

3. APPLICATIONS: SOME EXAMPLES

3.1. Ocean

It is well known that ocean has a strong influence on MT collected data near the coast. Particularly, TM phases resent its presence in the long periods, making it difficult to extract information on the real structure without being jeopardize by the ocean if the later is not included in the modeling. This situation is present in POM data. The Pacific Ocean should form part of the modeling if we want to extract useful information from the coastal sites.

As an example I will show the results of two inversions from artificial data. The original model is a 100 ohm-m half space close to the coast, where the ocean (up to 2 kilometers deep) has a resistivity of 0.3 ohm-m. first, the "data" was inverted from a 50 ohm-m half space which includes the ocean, with no constraints. Secondly, the data was inverted from the same starting model but with the condition the modeled ocean should stay throughout the whole inversion procedure. The resulting models produced by inversion of the TM data are shown in Figure A.3. Where the ocean was not constrained, the inverse code (unable to create structure outside the geographical range of the data) created some artificial conductivity structure in order to reproduce the ocean effect in the computed data. When the ocean was actually considered as part of the model, then the original half space conductivity is recovered faithfully.

3.2. Topography

An application of the third option was the inclusion of a topography representing the mountainous core of the Olympic Peninsula. Usually topography is considered to affect solely the apparent resistivities by a constant shift along the frequency range. The validity of this assertion will depend on the skin-depth associated with the structure. Most of the Olympic Mountains are formed by Tertiary sediments (water filled sedimentary rocks are very conductive), then it is possible the topographic effects may be sensed in the lowest periods. In order to test whether this was valid or not for the Olympic Mountains forward model calculations were performed.

Figure A.4 shows the calculated responses for the starting model used in Chapter V (model1) with and without topography. These were the results:

(1) small changes in phase at small period only in a few sites close to or at the mountains

(2) apparent resistivities curves affected by a multiplicative constant. The second result is what we call a "static shift". Thus what we see in the data is mostly subsurface structure. This encourages me to invert the data without topography as the benefits of including topography would not surpass the problems that comes with the inclusion of topography. Theoretically I could invert the data with topography, but the gap in the transect encloses most of the Olympic Mountains, which is a problem, as the information about this structure is not present. As the most important effect would be static shifts in a few stations, then I decided to invert the data without topography. Also 3D static-shifts effects due to topography would not be different from 2D static-shifts effects.

Summary

The new features added to RRI were not only useful to POM project, but indeed one of them was actually required. The ocean effect can not be avoided and thus the implementation of the the features that allows constraints on the model outside the station range is basic to invert POM data. Although topography was discarded in the inversion of the data, we can proved that doing so was valid, specially when it could not be discarded by a simple skin depth calculations.
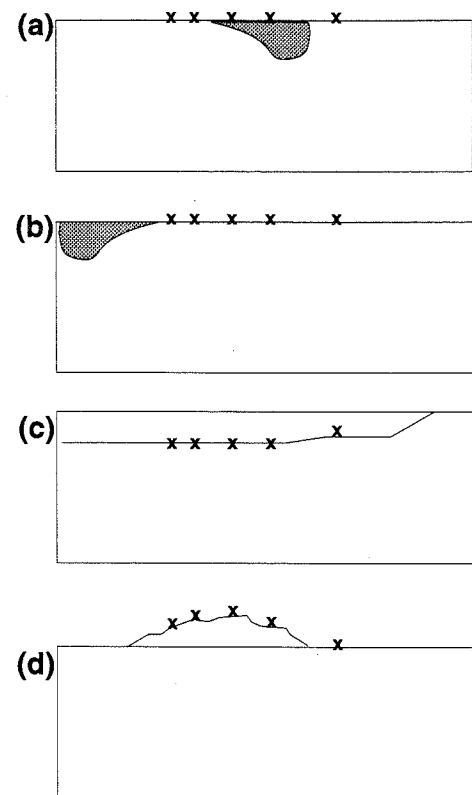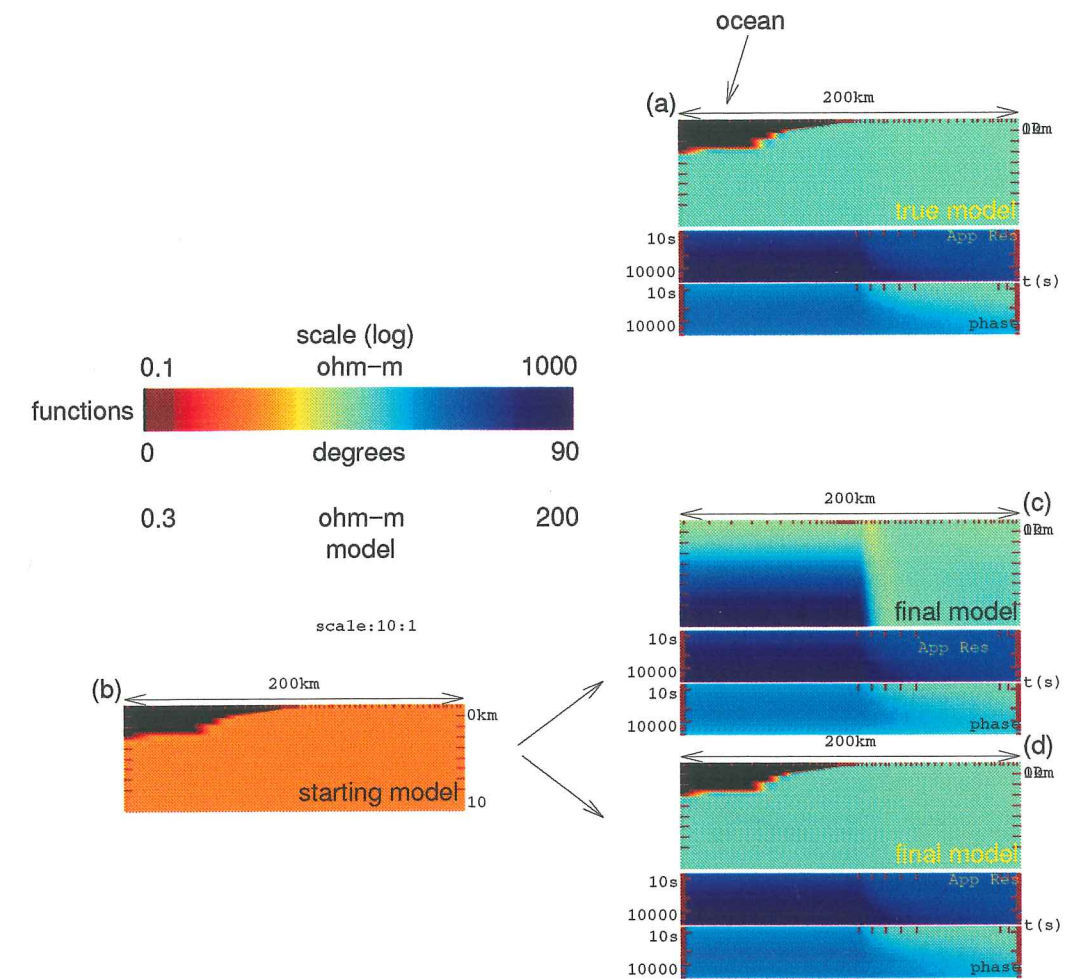
FIGURE A.1
Different situations that can be adressed in the inversion:
(a) part of the true model is known and involves stations
(b) part of the model is known but it is out of the range of stations
(c) stations are located at any other interface (i.e bottom of ocean)
(d) topography is present
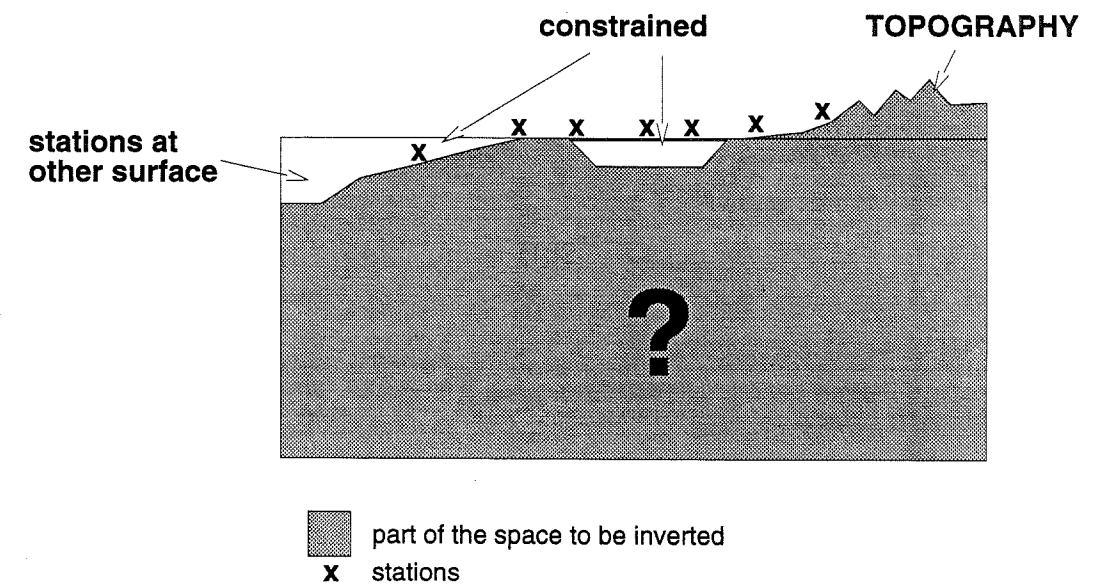
FIGURE A.2
The modified RRI can handle these situations: (1) stations at any interface
(2) constraints in the model (3) topography

133

FIGURE A.3

Ocean effect: (a) true model with data (b) starting model for inversions (c) result of inversion of the data with the no constraints (d) result of the inversion from the same starting model but with the condiction of the ocean being constrained throughout the inversion procedure. Note the recovery of the true model happens only in case (d), also the responses in case (c) do not fit the data as case (d).

APPENDIX B

CONDUCTIVITY OF ROCKS AND MINERALS: AN OVERVIEW

1. INTRODUCTION

Materials can be classified as conductors, semiconductors and insulators. Electrical currents come from the motion of charged carriers. Real materials are not pure compounds but a mixture of several. Offen several mechanisms of conduction are involved: metallic conduction, electronic semiconduction, solid and aqueous electrolytic conduction. *Zhdanov and Keller (1991)* give a comprehensive review of this topic. Unless explicitly stated, all references are taken from this review.

2. MECHANISM OF CONDUCTIONS

2.1. Metallic conduction

Drude theory explains the electrical conductivity of metals. When an external electric field is applied to a metal, the electrons of the electron gas surrounding the nuclei will accelerate in the direction of the field creating an electrical current along a particular direction. Collisions of the electrons with the nuclei limits the conductivity to a finite value, given by the following Drude's formulae:

$$\sigma = n \, e^2 \, \tau \, / \, m \qquad\qquad (B.1)$$

where σ is the conductivity, n is the number of free electrons per unit volume of the metal, *e* the charge of the electron, τ scattering time (time between collisions) and m the electron mass. The increase of temperature will decrease the mobility of the electrons and the effect is to reduce the conductivity. Imperfections in crystal structure will also reduce the conductivity as defects may inhibit mobility.

Some native metals, such as gold or copper are extremely rare, nevertheless high conductivity is expected when ore minerals happen. Graphite can be considered as a metallic conductor along one of its crystal planes it is not uncommon on the earth surface, so its presence, depending on the abundance, certainly will justify low values in resistivity.

2.2. Electronic semiconduction

The same basic theory can be applied to the case of electronic semiconduction. But the main difference is that a significant amount of energy must be added to electrons before they can move freely and carry charge (activation energy E). Increasing temperature will increase the number of free electrons (following the Stefan-Boltzmann law this number $n \propto e^{\frac{-E}{kT}}$) where T is temperature and k Boltzmann constant, but also will reduce their mobility, so the net effect is that semiconductors will show an increase in conductivity with temperature at some temperature ranges and the opposite in others.

Materials are composed by several atomic species. In this combination there are several activation energies (E) and the correspondent electrons will contribute to the conductivity depending on the amount of given energy and temperature.

Magnetite is a common mineral and its high conductivity (around 1000 S/m or 0.001 ohm-m resistivity) can be explained by this theory. Sulfide ore minerals are very conductive, meanwhile silicate minerals have a high electronic semiconduction resistivity but they can have a high ion conduction conductivity.

2.3. Solid electrolytic conduction

Electrolytic conduction can take place in ionic bonded crystals. Ions are responsible for the transport of charges and so they create with their motion along a particular direction, a macroscopic electrical current. The Coulomb type binding forces are so important that the simply applying of an external electric field could not cause ions to move, but imperfections in the crystal lattice allow this to happen. Atoms in the wrong lattice position or missing atoms give ions a way to move. Ions jump to interstitial or vacant lattice positions, but in a random way. When an external electric field is applied, there is a preferred direction and so a macroscopic electric current along that direction.

The number of ionic charge carriers available follows a Stefan-Boltzmann's type of law, there is a potential wall the ion must to cross to move out off the lattice. As temperature increases, the number of ionic charge carriers is expected to grow. The conductivity should be proportional to that number, to the mobility of the ion but it will also depend on the type of interstices in the crystal lattice. Small ions are expected to move more easily (in rocks these mobile ions can be the small single-nuclei atoms including sodium, magnesium and iron). Arrhenius plots characterize the conductivity curves for solid electrolytes (see Figure B.1). These are conductivity versus the inverse of temperature in logarithm scale.

For the most common type of rocks in their solid state, the conductivity resulting from this mechanism is very small. At elevated temperatures conductivity for dry rocks are generally a function of temperature rather on the composition. But for above the melting point, conductivity is greatly increased. For molten rocks it was found to be between 0.1 S/m and 1 S/m. Pressure is very important in the molten state (see examples in Figure B.2).

2.4. Aqueous electrolytic conduction

When salt is dissolved in water, ions separate and are free to move. When an external electric field is applied, then a net movement along is direction generates a current. The mobility of the ions will depend on the viscosity of water. Increasing temperature will help the ions to move as the viscosity decreases. Increasing concentration of ions will increase conductivity. But at very high concentration of ions may inhibited the mobility and so conductivity decreases.

Aqueous solutions fill pore spaces in rocks, this is the *most* important factor controlling the electrical conductivity of most rocks at the earth's surface. The conductivity of the water bearing rock will depend on the amount of water present, the brine conductivity and the way the pores are connected as well as on their geometry. Other mechanism of conduction still operates but dominated by aqueous ionic fluid. If at some temperature the water converts into steam, then the conductivity will decrease abruptly. But the pressure of the overburden normally take care of maintaining pore water in a liquid state when it is present in a rock.

2.4.1. Archie's Law

Archie's law is a empirical formula commonly used to relate the porosity and resistivity of the rock:

$$\sigma = a\, \sigma_w\, W^m \qquad \text{(B.2)}$$

where σ is the bulk conductivity of the rock, σ_w the fluid conductivity, W is the fluid content (porosity if all pores are filled with fluid), and a and m are fitting parameters for a particular type of rock. These parameters depend on the geometry of the pore structure. There are basically three cases:

(1) intergranular space in clastic detrital rocks

(2) fracture, joint and microcrack pores, usually crystalline rocks

(3) vugs or other large poorly interconnected pore spaces, as in extrusive volcanic rocks.

For the same porosity a brine conductivity (2) will give the highest conductivity and (3) the lowest. Fluid conductivity will depend on several factors, as temperature, density, pressure and concentration (see examples in Figure B.3). The *formation factor* is defined as:

$$F = \frac{\sigma_w}{\sigma} \qquad \text{(B.3)}$$

Table (B.1) shows some values for a and m that may be used if the lithology of a rock is known (generally m=2 for spherical pores, and m=1 for cracks):
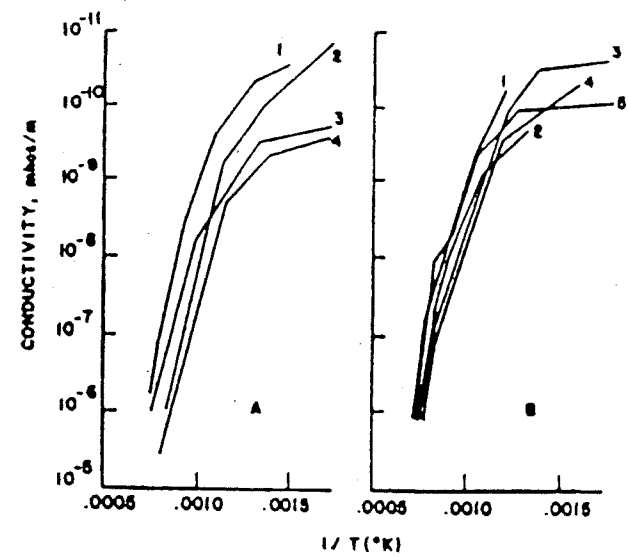
Near surface water-saturated rocks:

For near-surface water-saturated rocks, a better way to describe the conductivity is given by the following expression (Schopper,1982(43r.1)):

$$\sigma = \frac{1}{F} \sigma_{w+} \sigma_s \qquad (B.4)$$

where F is the *formation factor*, σ_w the brine conductivity and σ_s the surfaceconductivity. The second term depends largely on the size of the hydrophilic inner surface area of the rocks accessible to the electrolyte. Clays, mudstones, marls and weakly consolidated shales may reach an important inner surface area, as they contain clay minerals and colloidal material to a great extent. The conductivity σ_s may easily reach or even exceed 1 S/m. Its importance decreases with depth since clay minerals transform to illite and mica accompanied by coarsening of the grains. When the later term is not important, Archie's law can well represent the conductivity.
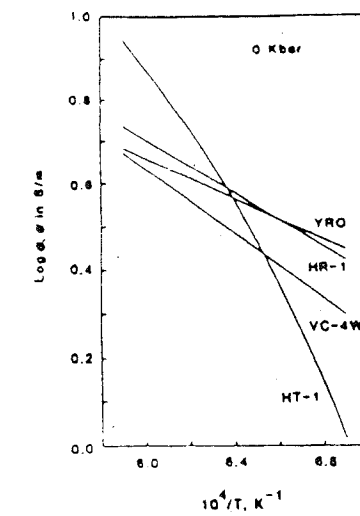
lithology	a	m
TABLE 3.1: Archie's Law		
weakly detrital rocks, such as sand and some limestone with a porosity range 25-45%, usually Tertiary in age	0.88	1.37
Moderately well cemented sedimentary rocks, including sandstones and limestone, with a porosity range 18-35%, usually Mesozoic in age	0.62	1.72
Well-cemented sedimentary rocks with a porosity range of 5-25%, usually Paleozoic in age	0.62	1.95
Highly porous volcanic rocks such as tuff with porosity in the range of 20-80%	3.5	1.44
rocks with less than 4% porosity, including dense igneous rocks and metamorphosed sedimentary rocks	1.4	1.58

Arrhenius plots for molten andesite (VC–W4), rhyodacite (HR–1), rhyollite (YRO) and Hawaiian thoeleiite (HT–1) (from Zhdanov & Keller, 1991).
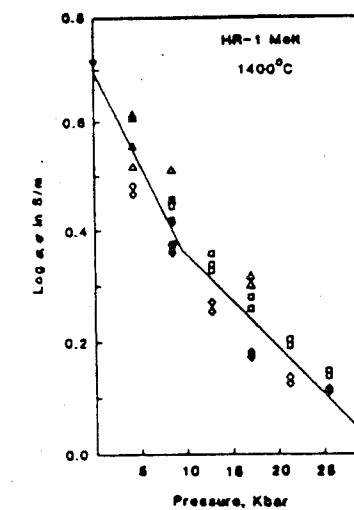

FIGURE B.1

Arrhenious plots: relationship between conductivity and temperature fin acidic and intermediate rocks. Slope is related to the activation, energy different energies are activated with temperature.
(A: 1–2 andesite, 3 quartz diorite, 4 andesite basalt; B: 1 quartzite 2–3–4 granite 5 perthite; from Zhdanov & Keller, 1991).
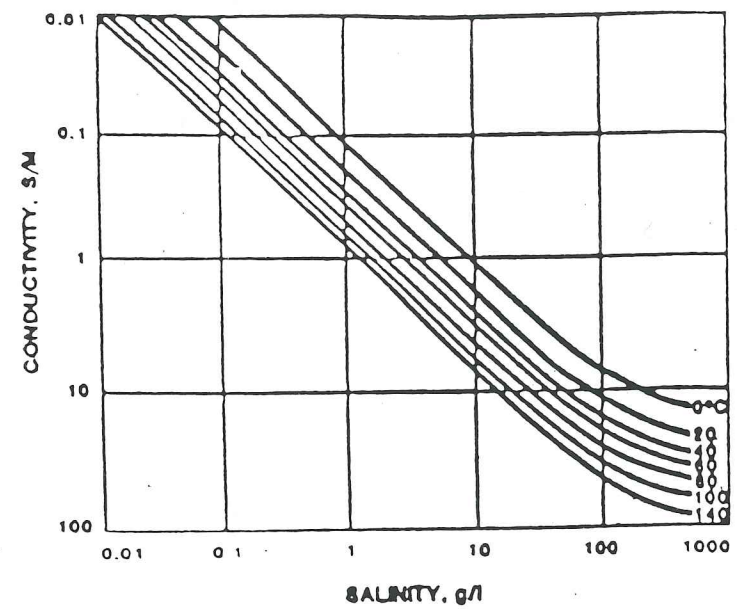
Conductivity of molten rhyodacite at 1400C as a function of preassure (from Zhdanov & Keller, 1991).

FIGURE B.2

144

FIGURE B.3

Brine conductivity: ffect of concentration an temperature on the
conductivity of a solution of sodium chloride (from Zhdanov &
 Keller, 1991).